UNIVERSITY OF CALIFORNIA

Los Angeles

Hybrid Fabrication and Characterization of Two-Dimensional Vanadium Disedelined Related Materials

A dissertation submitted in partial satisfaction of the requirements for the degree Doctor of Philosophy in Materials Science and Engineering

by

Abdullah Ali S Alrasheed

2025

© Copyright by

Abdullah Ali S Alrasheed

2025

ABSTRACT OF THE DISSERTATION

Hybrid Fabrication and Characterization of Two-Dimensional

Vanadium Disedelined Related Materials

by

Abdullah Ali S Alrasheed

Doctor of Philosophy in Materials Science and Engineering

University of California, Los Angeles, 2025

Professor Kang L. Wang, Chair

Two-dimensional (2D) van der Waals (vdW) materials have attracted significant interest for next- generation spintronic, electronic, and energy-storage applications due to their unique layer-dependent properties, including magnetism, charge transport, and mechanical flexibility. Nevertheless, the development of robust and scalable devices remains challenging. Key issues include the air sensitivity of many 2D crystals, difficulties in integrating conventional lithographic methods without contamination, and obstacles in forming uniform, high-quality oxide barriers for tunneling applications. In this work, a “hybrid” fabrication method is introduced that combines **confocal laserinduced oxidation** with **inductively coupled plasma (ICP) etching**, providing a mask-free, controllable strategy for surface

modification and patterning. Vanadium diselenide (VSe_2) is used as a

demonstration platform, wherein localized laser irradiation in an oxygen-rich environment generates a vanadium pentoxide (V_2O_5) layer with adjustable thickness and lateral dimensions. By exploiting differential ICP etch rates for VSe_2 and V_2 O_5, selective removal enables precise device geometries to be defined without the need for polymeric masks or chemical developers. The resulting oxide barrier can serve as an ultrathin insulating layer suitable for tunneling magnetoresistance (TMR) applications, while preserving a cleaner oxide–metal interface to mitigate spin-scattering defects and pinholes. In addition, localized oxidation or doping introduced at the oxide interface can potentially modify magnetic anisotropy, suggesting a route toward perpendicular magnetic anisotropy (PMA) in 2D magnets that typically exhibit in-plane magnetization. Beyond VSe_2, this approach is compatible with other 2D magnets and transition metal dichalcogenides (e.g., MoS_2, WSe_2, $MnBi_2Te_4$), facilitating the design of multi-barrier tunnel junctions, lateral heterostructures, and integrated energy-storage architectures without conventional mask alignments. The method's scalability is supported by the widespread availability of industrial laser scanning platforms and standard ICP tools. Overall, the hybrid laser–plasma fabrication presented here addresses critical barriers to integrating 2D materials in spintronic devices and lays the groundwork for the creation of novel magnetic and electronic architectures.

The dissertation of Abdullah Ali S Alrasheed is approved.

Gregory P Carman

Alexander Alexee Balandin

Qibing Pei

Kang L. Wang, Committee Chair

University of California, Los Angeles

2025

Dedicated to my Father

Table of Contents

ABSTRACT OF THE DISSERTATION....ii

Table of Contents....vi

List of Figures....x

1. Introduction....1

1.1 Motivation....5

1.2 Material Background....7

1.2.1 Background on Two-Dimensional VSe2....7

1.2.2 Crystal Structure and Synthesis....9

1.2.3 Phases and Structural Transitions....9

1.2.4 Applications....10

1.2.5 Outlook and Challenges....10

1.3 Literature Review of Thin V_20_5: Fabrication, Challenges, Crystal Structure, and Applications in Lithium-Ion Batteries....11

1.4 Crystal Structure of V_20_5....11

1.4.1 Fabrication of Thin V_20_5/f….....11

1.4.2 Challenges in Thin Film Fabrication....13

1.4.3 New Approaches for Nanoscale Engineering....13

1.4.4 Applications in Lithium-Ion Batteries....13

1.5 Ferromagnetic Behavior of VSe2....14

1.5.1 Introduction....14

1.5.2 Theoretical Foundations of Ferromagnetism in VSe2....15

1.5.3 Role of Defects and Se Vacancies....16

1.6 Experimental Investigations and Conflicting Reports....17

1.7 Recent Developments....18

1.8 Strain, Annealing, and Defects Effects 19

1.8.1 Strain Effects 19

1.8.2 Annealing and Defects Effects 20

1.9 Chronological magnetic study in correlation with the number of layers of VSe_2 21

1.91 Ferromagnetism in Ultrathin VSe_2 Nanosheets 21

1.9.2 No Ferromagnetism in Exfoliated VSe_2 21

1.9.3 Transport Studies Indicating No FM in Chemical Vapor Deposition (CVD) Few-Layers 22

1.9.4 Room-Temperature Ferromagnetic Domains in Few-Layer VSe_2 22

1.10 Prospects for Applications and Future Research 24

1.10.1 Challenges and Research Gaps Procedures and Results 25

1.11 Conclusions 26

2. Procedures and Results 27

2.1 Experimental Setup 27

2.2 Summary of Results 31

2.2.1 Laser-Induced Oxidation and Evaporation of VSe_2 32

2.2.2 Heat Transfer Effects and Edge Oxidation 33

2.3 Laser-Induced Oxidation and Evaporation of VSe_2 32

2.2.3 Plasma Etching of VSe_2 and V_2O_5 34

2.2.4 Post-Etch Magnetic Behavior and Theoretical Insights 35

2.3. Theoretical Correlation Between Vacancies, Strain, and Magnetism 36

2.4 Results Section 37

2.4.1 FM at RT for thick VSe2 37
2.4.2 Hybrid fabrication method 38
2.5 The results of the Hybrid fabrication method in Magnetic moment study for the thinned flake 51
2.6 Theoretical Correlation Between Selenium Vacancies and the Increase in Magnetic Moment 54
2.7 Figures 60
3. Results analysis and discussion 82
3.1 Overview 82
3.2 Laser Treatment System 82
3.3 Plasma Etching Equipment 83
3.4 Characterization Methods 84
3.5 Heat Transfer Effects 84
3.6 Magnetic Characterization 85
3.7 Plasma Etching Selectivity 86
3.8 Summary 88
3.9 Discussion 88
4 Conclusion 93
4.1 Key Findings and Contributions 93
4.2 Broader Implications and Future Directions 95
5 Methodology 96
5.1 Sample Preparation 97
5.2 Characterization Techniques 98
5.3 Plasma Etching 99
6. References 106

7. Appendices.....111

List of Figures:

Figure 1: Number of publications on 2D, 1D and 0D from 2000 to 2032, illustrating the significant difference between 2D publications and the rest.....5

Figure 2: Chronological line for experimental investigation on the magnetic behavior of 2D VSe_2. The red circle indicates no FM detected, green FM. And Yellow circle indicates a switch form non-FM to FM due to defect engineering… 23

Figure 3: Thickness vs chorological magnetic study results. Maxum thickness with FM reported is 8nm until this work. Insite show the SQUID result of this work 24

Figure 4: The Laser Treatment apparatuses. Using the laser in situ with the Raman spectroscopy set 62

Figure 5: Effects of high power laser treatments on the VSe2 flake. (A) shows the before and after images. (B) shows the effects after 100mW power, 785nm laser for 1min. Red arrow show light green coloring from the SeOx due to laser treatment. (C) SEM image detailing the effect of the laser treatment.....62

Figure 6: A & B show the effect of 100mW laser treatment for 5 min: A after the treatment and B 24 hours later. C shows the Raman

spectra. Black is the pristine measurement and red is 24 hours later. On a spot 8um away from the treatment location. It shows the disappearance of VO2 peak 63

Figure 7: Flake single laser treatment of 100mW, 785nm, five minutes. Raman spectra show three locations: black spectra (center of laser treatment), red 3um away from laser treatment spot, blue 6um from laser treatment spot. The blue curve is small to show any feature only the strong oxide at 230-1. Both black and red show a combination of vanadium oxide peaks. Peaks of 305 and 405 cm-1. Check the Raman shift table in the appendix 63

Figure 8: A) showing the pristine flake. B) flake after laser treatment of 100mW using 785nm laser. C) leaving one week in ambient condition. D) after three days in the glovebox..... 64

Figure 9: Shows a flake that was left after treatment (100mW for 5 min.). The Insite show Raman spectra, the development of the V_2O_5 peak. The Raman spectra were taken 10 um away in the red zoon shown in the optical image. Three Raman measurements were taken, black before laser treatment, red after treatment, blue after one week in glove box, green three days in Ambient conditions. These measurements were taken one after the

other respectfully 64

Figure 10: A) before laser mapping treatment. B) after laser mapping treatment 65

Figure 11: A) optical image showing treatment and Raman map. B) Raman spectra of oxide area. C) Raman spectra showing no treatment 65

Figure 12: A) optical image showing treated location. B) Raman spectra of treated Area, showing spectra V_2O_5 peak at 995cm-1 65

Figure 13: A) optical image showing treated location. B) Raman spectra of treated area, showing spectra V_2O_5 peak at 995cm-1 66

Figure 14: A) optical image showing treated location. B) Raman spectra of treated area, showing spectra V_2O_5 peak at 995cm 66

Figure 15: Simulation results for laser treatment on the surface of VSe_2 of varying thickness. Assuming no heat exchange with the surrounding except the SiO_2 substrate. SiO_2 substrate was kept at 300nm 66

Figure 16: Simulation results for laser treatment on the surface of VSe_2 of varying thickness. Assuming no heat exchange with the surrounding except the SiO_2 substrate. SiO_2 substrate was kept at 30 67

Figure 17: Shows the growth of the oxide starting from the edge. Going from A to C, the growth evolves from the edge. The treatment location is pushed down as seen in C by the red box. Mapping parameters 50mW for 0.1s 67

Figure 18: A treated sample heat effect on the thin edge, with Raman spectra showing oxide peak of 250cm-1. A) optical image of the treated area. B Raman spectra of edge showing oxide peak. C&D SEM images of the effect of laser 68

Figure 19: A) Optical image of laser mapping treatment on the edge. B) SEM image of the laser mapped edge. C) EDS results for the % compound on the points in B 68

Figure 20: A) showing RF plasma effect before and after. Top images show the before, bottom images show the after. B) Show the Raman spectra. All spectra show no change 69

Figure 21: Shows a set of ICP plasma treatments, indicating no change. Left, before treatment; right, after treatment 69

Figure 22: A) shows the Raman spectra of after RF plasma treatment. B) shows the Raman spectra after ICP plasma treatment..... 70

Figure 23: All figures showing the effects of etching when using CF4 for high powers and longer time 70

Figure 24: A) optical image after laser treatment and before ICP plasma treatment. B) after plasma treatment. C) Raman spectra (black spectra before ICP treatment, red after plasma treatment)..... 71

Figure 25: A) and B) are optical images of before and after CL ICP etching. C) Raman spectra of before (black) after (red). D) 3D AFM.....71

Figure 26: the AFM results thickness before the ICP CL etching.....72

Figure 27: AFM after ICP CI-etching, showing a decrease in thickness of 300nm. The red circles are where the measurements are.....72

Figure 28: Showing the V2O5 grown via annealing before and after ICP CI plasma etching. Etching for 1 minute up to 3 minutes.....73

Figure 29: A) and B) show the optical image of flakes before and after the CL plasma treatment (not the same flake). C) and D) show the Raman spectra for both, with a clear peak at 960 and 990 that is of V_2O_5 but the A1g peak can be seen indicating the presence of the VSe_2 underneath. 73

Figure 30: Selective etching for VSe_2 and preserving V_2O_5. A) and B) before and after etching; red circle shows V_2O_5 after ICP CL etching. C) Raman spectroscopy for V2O5. E) SEM image. D) EDS results..... 74

Figure 31: Selective etching of V_2O_5. A) and B) illustrate an optical image before and after etching (red circle treated V_2O_5).C) and D) illustrate Raman Spectra: C) V_2O_5 Raman spectra. D) Raman spectra after ICP CF4 etching..... 74

Figure 32: EDS results before and after ICP CF4 plasma treatment. EDS data were taken on the red circle area..... 75

Figure 33: ICP etching results. Raman spectra only showing A1g. No oxide peak detected. And no shift for the A1g.....75

Figure 34: 3D AFM results after ICP CH_4.....76

Figure 35: AFM images. C) 3D AFRM image (circle image) 76

Figure 36: ARM image. B) values are adjusted to the nearest three digit, which is not real value (software adjusted values).....77

Figure 37: 3D AFM. B) MFM phase image that shows magnetic moment..... 77

Figure 38: CF4 ICP plasma etched flake 78

Figure 39: AFM image after ICP CF_4 etching 78

Figure 40: A) optical image. B) 3D AFM image. C) MFM image 79

Figure 41: DFT simulation. Removing Se single atom and observing the increase of magnetic moment as well as an increase in local strain.....79

Figure 42: A) using DFT simulation correlate Se vacancy with strain. B) DFT simulation correlating Se vacancy Jhan-Teller distortion. C) DFT simulation and correlation of Se vacancy with the magnetic moment 80

Figure 43: Dos of VSe2 each figure represents a % Se vacancy. Starting from 0% Se vacancy..... 80

Figure 44: A) SQUID results VSe2 CVD grown and exfoliated on SiO2 (300nm) for inplan external magnetic. B) optical image of the

VSe2 flake. C) and D) optical and AFM results of a flake. E) statistic of an example of flakes with various thickness 81

Figure 45: DFT simulation for the correlating strain with magnetic moment. E) the outer plan strain vs. magnetic moment..... 82

Figure 46: A) and B) are published results from Ci, et al. 2022, showing SQUID results and thickness of flakes. Comparing This works SQUID result, of in plan at room temperature 82

Figure 47: Density of states (DOS) of VSe_2 under different strain conditions. the total DOS for three different strain values (-0.1, 0.0, and 0.1). The spin-up and spin-down contributions are depicted with solid and dashed lines, respectively. **(b)** presents the projected density of states (PDOS) for the d-orbital (orbital 3 of Vanadium (V)..... 82

Figure 48: Schematic of the confocal Raman laser treatment system..... 84

Figure 49: Simulated heat distribution for VSe2 flake 86

Figure 50: MFM results showing the correlation between thickness and magnetic moment.....87

Figure 51: DFT calculations showing the effect of Se vacancies on the magnetic moment..... 88

Bio

Abdullah is a materials scientist and engineering Ph.D. candidate at UCLA, specializing in the fabrication and property modulation of two- dimensional (2D) van der Waals materials. Under the supervision of Professor Kang L. Wang, his research focuses on controlling the magnetic properties of VSe_2 through advanced techniques such as laser thinning, plasma etching, and H_2 annealing, aiming to enhance magnetism via defect engineering. His work has also demonstrated the potential of oxidized VSe_2 as a lithium-ion battery anode and explored selective etching strategies for vanadium-based materials. In addition to his research, Abdullah is a researcher at the King Abdulaziz City for Science and Technology (KACST), where he contributes to the advancement of nanotechnology, energy storage, and quantum materials.

1. Introduction

Two-dimensional (2D) van der Waals (vdW) materials have emerged as one of the most transformative classes of materials in the field of nanotechnology and materials science. These materials, including graphene, hexagonal boron nitride (h-BN), and transition metal dichalcogenides (TMDs) (such as MoS_2 and WSe_2) exhibit a range of extraordinary physical, electrical, and optical properties [1], [2]. Unlike bulk materials, their atomic-scale thickness and the vdW interactions between layers result in unique features such as quantum confinement effects, tunable bandgaps, high carrier mobilities, and large surface-to-volume ratios [3], [4]. These properties make 2D materials highly desirable for next-generation applications in electronics, photonics, sensing, and energy storage [5].

Graphene, the first 2D material to be isolated, catalyzed a wave of interest in these materials due to its remarkable electrical conductivity and mechanical strength [6].

Following the discovery of graphene, researchers identified numerous other 2D materials, each with distinct properties. For example, TMDs such as MoS_2 and WS_2 are semiconductors with direct bandgaps in their monolayer form, making them ideal for optoelectronic devices [7].

Similarly, h-BN is an excellent insulator with a wide bandgap, commonly used as a dielectric layer in heterostructures [8].

Despite their promise, the integration of 2D materials into large-scale production remains a significant challenge. Conventional fabrication methods such as mechanical exfoliation, chemical vapor deposition (CVD), and physical vapor deposition (PVD) have critical limitations. Mechanical exfoliation, for example, yields high-

quality flakes but is inherently low throughput and is unsuitable for scalable manufacturing [9]. CVD offers scalability and uniformity but often suffers from substrate restrictions, interfacial contamination, and difficulties in controlling nucleation and growth [10]. These obstacles hinder the widespread adoption of 2D materials in practical applications and necessitate innovative approaches to fabrication.

Hybrid fabrication methods have emerged as a powerful solution to the challenges associated with large-scale production of 2D materials. These methods combine two or more fabrication techniques to leverage the strengths of each while mitigating their individual limitations. For instance, the development of hybrid processes such as CVD combined with transfer printing addresses the contamination and mechanical stress introduced during film transfer. In this approach, a 2D film grown on a sacrificial substrate, such as copper foil, is transferred to a target substrate using a polymer support like polydimethylsiloxane (PDMS) or polymethyl methacrylate (PMMA). This process reduces defects and ensures cleaner interfaces [11]. Another example is polymer-assisted exfoliation, which combines the scalability of CVD with the high quality of exfoliated flakes. In this method, CVD grown films are coated with a polymer layer, peeled off from the substrate, and transferred to another substrate for further processing. This technique not only minimizes substrate damage but also

allows substrate reuse, which is particularly beneficial when using expensive substrates like sapphire [12]. This technique not only minimizes substrate damage but also allows substrate reuse, which is particularly beneficial when using expensive substrates like sapphire [12]. Hybrid processes also address challenges in nucleation control and domain size.

For example, solution-phase exfoliation followed by CVD seeding involves using exfoliated nanosheets as seed crystals on a substrate. Subsequent CVD growth expands these seeds into larger, more uniform domains, significantly reducing grain boundaries and improving film quality [13], [14]. This method has been successfully applied to various TMDs, enabling better control over domain orientation and film properties. Epitaxial growth combined with electrochemical exfoliation is another hybrid strategy that has gained traction. Electrochemical exfoliation produces few layer graphene or TMD flakes, which are then subjected to epitaxial regrowth to repair defects and enhance crystallinity. This combination enables fine control over doping and layer thickness, making it a promising approach for electronic and optoelectronic applications [15]. This combination enables fine control over doping and layer thickness, making it a promising approach for electronic and optoelectronic applications [15]. A particularly innovative hybrid method involves atomic layer deposition (ALD) followed by post-annealing in a chalcogen-rich environment. ALD provides angstrom-level thickness control, while the annealing step

crystallizes the amorphous films into high-quality 2D layers. This approach combines the

precision of ALD with the improved crystallinity of annealing, making it highly suitable for applications requiring exact thickness and uniformity [16].

These hybrid fabrication methods are not merely incremental improvements; they represent a paradigm shift in the way 2D materials are synthesized and integrated. By combining top-down and bottom-up approaches, hybrid methods overcome the limitations of individual techniques, enabling the production of large area, high-quality films with precise control over structural, electronic, and optical properties [17]. The significance of hybrid methods extends beyond their technical advantages. They address critical bottlenecks in scaling up 2D materials for industrial applications.

In conclusion, hybrid fabrication methods are indispensable for advancing 2D materials from laboratory research to industrial-scale production. By leveraging the strengths of multiple techniques, these methods address fundamental challenges in scalability, quality, and integration. As the field continues to evolve, hybrid approaches are expected to play a pivotal role in enabling the widespread adoption of 2D materials in applications ranging from flexible electronics to quantum computing, laying the groundwork for the next generation of technological innovations.

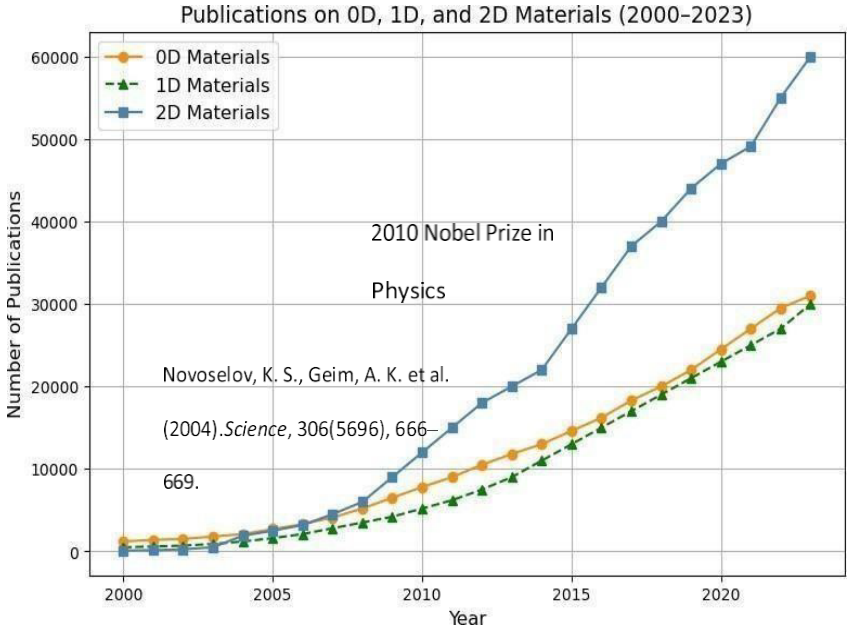


Figure 1: Number of publications on 2D, 1D and 0D from 2000 to 2032, illustrating the significant difference between 2D publications and the rest.

1. Motivation

Our Proposal for a New Hybrid Fabrication Method Motivated by these advancements, my work focuses on a novel hybrid approach utilizing confocal laser treatment under controlled environmental conditions. This technique allows precise surface modifications of 2D vdW materials, enabling three potential outcomes: (1) sublimation or evaporation of top surfaces, (2) controlled oxidation of top surfaces, or (3) induction of structural defects that trigger phase changes. This method addresses challenges in treating materials highly resilient to low laser powers, such as VSe2, which can be damaged or oxidized with high-power lasers.

In my research, I focus on controlled oxidation of VSe_2 surfaces to form V_2O_5, followed by selective inductively coupled plasma (ICP) etching. This process enables precise thinning of the VSe2 layer without affecting the V_2O_5 regions. Subsequently, a second ICP plasma recipe removes the V_2O_5 layer, offering unparalleled control over the thickness of specific regions.

Alternatively, direct etching of V_2O_5 can also thin the flake while preserving the underlying VSe_2. These strategies provide scalable solutions for producing patterned and thinned vdW materials. The process leverages the scalability and cost-effectiveness of laser and plasma treatments compared to techniques like ALD, electron-beam lithography, or molecular beam epitaxy (MBE). By replacing confocal lasers with millimeter-scale lasers, the approach can be extended to large-scale production and automated processes, enhancing its industrial applicability. VSe_2 serves as a representative example of a vdW material for this study, with a focus on thinning flakes to achieve ferromagnetism (FM) (citation to be added).

Post-thinning characterization is performed using atomic force microscopy (AFM), Raman spectroscopy, and magnetic force microscopy (MFM) to validate the increase in magnetic moment. Additionally, this research explores using laser treatment to fabricate V_2O_5 directly on the VSe_2 surface, offering a new route for producing V_2O_5. Finally, an investigative study using density functional theory

(DFT) simulations examines the role of selenium defects in enhancing FM in VSe_2. Preliminary findings suggest that lattice distortions associated with these defects influence the density of states (DOS), indirectly increasing the magnetic moment. This comprehensive approach represents a significant contribution to the design, fabrication, and understanding of 2D vdW materials, paving the way for future advancements in materials science and engineering.

1.2 Material Background

We focus on two materials as representative examples for our hybrid method:

1) (1T) VSe_2 (a metallic TMD) and
2) V_2O_5 (a layered oxide with promising electrochemical properties)

Section 1.2.1 provides a general background on VSe_2, including its crystal structure, electronic and magnetic properties, phase transitions, and potential applications. Section 1.3.2 offers a review of thin V_2O_5 films in the context of lithium-ion battery applications.

Finally, Section 1.2.2 provides a deeper discussion of the ferromagnetic behavior of VSe_2, surveying both theoretical predictions and experimental evidence in the literature.

1.2.1 Background on Two-Dimensional VSe2

Vanadium diselenide (VSe_2) is a layered transition metal dichalcogenide (TMD) that has attracted intense interest for its unique physical properties, multiple accessible phases, and potential applications in

electronics, spintronics, and energy storage [18]. As with other TMDs, VSe_2 can be exfoliated down to the monolayer limit, exhibiting novel two-dimensional (2D) phenomena such as enhanced magnetic ordering and charge density wave (CDW) transitions [19]. In this background, we discuss the crystal

structure of 2D VSe_2, its electronic and magnetic properties, phase transitions, and prospective applications.

1.2.1 Crystal Structure and Synthesis

Layered Structure. In the bulk form, VSe_2 crystallizes in a 1T (octahedral) structure, where each vanadium atom is octahedrally coordinated by six selenium atoms. These layers stack along the c- axis and are held together by vdW interactions [20]. Because of the relatively weak interlayer coupling, mechanical or chemical exfoliation methods can be used to obtain ultrathin flakes or monolayers of

VSe_2.

Phase Variations. While the bulk stable form of VSe_2 is typically the 1T phase, studies have indicated that monolayer or few-layer VSe_2 can exhibit subtle structural distortions, sometimes linked to the formation of a charge density wave or to the stabilization of other phases under specific conditions (such as doping or strain) [21]. Phase stability can also be tuned by changing external parameters like temperature, pressure, or by substrate induced strain when grown via molecular beam epitaxy (MBE).

Synthesis Methods. The main routes for synthesizing 2D VSe_2 include: *Mechanical Exfoliation* from bulk crystals grown by chemical vapor transport or flux methods (limited in large-area coverage) [22]. *Chemical Vapor Deposition (CVD)*, which can yield wafer-scale films with thickness control but demands careful optimization of precursors and temperature [23].

Molecular Beam Epitaxy (MBE), enabling high-purity monolayers with controlled thickness and crystallinity [24].

1.2.2 Electronic and Magnetic Properties

VSe_2 distinguishes itself from more common semiconducting TMDs (like MoS_2 and WS_2) by being metallic and by exhibiting interesting magnetic behavior when reduced to the 2D limit [25].

Metallic Conductivity. VSe_2 maintains metallic conductivity due to partially filled d-orbitals from vanadium atoms. In the monolayer limit, the electronic band structure can shift, leading to enhanced electron correlations [21].

Magnetism. Monolayer VSe_2 may exhibit ferromagnetic behavior at or near room temperature, making it attractive for spintronic applications [26]. However, the presence and robustness of this magnetism depend on sample quality, substrate effects, and defect concentrations.

Charge Density Waves (CDWs). VSe_2 hosts a CDW phase at low temperatures (105 K in bulk) [24]. In the monolayer limit, the CDW transition temperature and periodicity can shift, serving as a platform for

studying electron correlations and lattice instability.

1.2.3 Phases and Structural Transitions

The 1T phase is the most common structure for VSe_2, characterized by octahedral coordination. In monolayer form, this structure is generally preserved but can be distorted by CDW formation, strain, or layer dependent effects [23]. Although phase engineering is well-known in other

TMDs, VSe_2 remains predominantly 1T. Nonetheless, doping or intercalation can tune structural and electronic properties [27].

1.2.4 Applications

Spintronics: The possible ferromagnetism in monolayer VSe_2 opens avenues for magnetic storage, spin filtering, and other spin-dependent phenomena.

Electronics and Contact Layers: Owing to its metallic nature, VSe_2 can serve as a low resistance contact for 2D semiconductors or as an ultra-thin interconnect in layered device architectures [25].

Energy Storage and Conversion:

Battery Electrodes: Metallic conductivity and layered structure make VSe_2 appealing for ion storage (e.g., Li^+, Na^+) [27].

Electrocatalysis and Supercapacitors: The large active surface area and favorable electronic structure of metallic TMDs can benefit catalytic reactions or fast charge/discharge cycles.

Fundamental Research: VSe_2 is a fertile ground for studying charge

density waves, magnetism in low dimensions, and heterostructure physics when stacked with other 2D materials.

1.2.5 Outlook and Challenges

Reproducible Synthesis: Large-area, defect-free monolayers require refined CVD/MBE protocols [23].

Stability: Metallic TMDs can be more reactive, necessitating inert processing or encapsulation [25].

Magnetic Characterization: More rigorous spin-sensitive probes are needed to fully understand the origin and stability of magnetism [26].

Device Integration: Achieving stable interfaces, doping control, and patterning at scale remains a challenge for commercial VSe2-based devices [24].

1.3 Literature Review of Thin V_2O_5: Fabrication, Challenges, Crystal Structure, and Applications in Lithium-Ion Batteries

Vanadium pentoxide (V_2O_5) is a layered transition metal oxide with promising electrochemical properties. Its layered crystal structure, high theoretical capacity, and relatively low cost make it attractive for applications in energy storage devices, particularly lithium-ion batteries (LIBs) [18]. Thin films of V_2O_5 have garnered special interest due to their advantageous kinetics and potentially enhanced electrochemical performance, including faster lithium intercalation and superior rate capability [19]. This subsection summarizes the crystal structure of V_2O_5, provides an overview of established and emerging thin-film fabrication methods, addresses key challenges in the fabrication process,

and highlights recent approaches toward nanoscale engineering of V_2O_5 for LIB applications.

1.4 Crystal Structure of V_2O_5

*V*2*O*5 typically crystallizes in an orthorhombic layered structure, where layers of distorted VO5 square pyramids share edges and corners, forming two-dimensional sheets [28]. These sheets are loosely bonded by weak van

der Waals forces, facilitating the intercalation of guest species such as Li^+ ions. The layered structure of V_2O_5 contributes to its high theoretical capacity for LIBs, often cited around 294 mAh g^{-1} based on the reversible insertion/extraction of lithium ions [29]. However, the electronic conductivity of bulk V_2O_5 is relatively low. One strategy to address this issue involves producing thin films or nanostructured V_2O_5, which shortens Li^+ diffusion paths and can improve both ion transport and overall electrochemical performance.

1.4.1 Fabrication of Thin V_2O_5/f

Physical Vapor Deposition (PVD) Methods

Thermal Evaporation and Electron-Beam Evaporation: V_2O_5 powder is heated under high vacuum until sublimation. The evaporated species condense on a substrate to form a thin film [30]. Controlling film stoichiometry and uniformity is a key challenge.

Sputtering: Reactive magnetron sputtering employs a vanadium target in an oxygen-containing atmosphere. By tuning oxygen partial pressure and substrate temperature, high-purity V_2O_5 thin films can be

achieved with controllable thickness and stoichiometry [18].

Chemical Methods

Sol-Gel Processing: Involves hydrolysis and condensation of vanadium alkoxides or vanadyl precursors in solution. Spin-coating or dip-coating onto substrates is followed by controlled heat treatment [31].

Chemical Vapor Deposition (CVD): Vanadium-containing precursors decompose at elevated temperature in oxygen, allowing conformal coating

and precise thickness control of V_2O_5 [32].

1.4.2 Challenges in Thin Film Fabrication

Stoichiometry Control: Deviations in the O:V ratio can produce different vanadium oxide phases (V_2O_3, VO_2, etc.), impacting battery performance [30]. **Uniformity and Thickness Control:** Achieving uniform thin films at scale remains non-trivial. **Adhesion and Stability:** Films must strongly adhere to substrates and maintain stability under repeated battery cycling. **Conductivity:** Low electronic conductivity necessitates doping or composite approaches (e.g., carbon additions).

1.4.3 New Approaches for Nanoscale Engineering

Nanostructured Composites: Embedding V_2O_5 nanostructures into conductive matrices (graphene, CNTs, etc.) enhances electron transport and shortens Li^+ pathways [33].

Atomic Layer Deposition (ALD): Enables atomic-scale thickness control for ultra-thin, uniformV_2O_5 films [19].

Electrochemical Deposition: Grows V_2O_5 directly on current collectors,

reducing contact resistance [18].

3D Nanoarchitectures: Employing 3D scaffolds (e.g., metal foams) increases surface area and mitigates mechanical stress [25].

1.4.4 Applications in Lithium-Ion Batteries

High Theoretical Capacity: 294 mAh g^{-1} [21].

Improved Rate Capability: Thin films + conductive additives compensate for low conductivity [19].

Enhanced Cycle Life: Optimizing morphology/stochiometry lessens capacity fading [24]. **Lower Material Consumption:** Thin coatings reduce material costs and support miniaturized devices.

While V_2O_5 excels in capacity, its limited conductivity, potential dissolution at higher voltages, and structural changes upon cycling require continued research. Techniques like doping (W, Na), surface coatings, and hybrid nanocomposites help address these issues [23].

1.5. Ferromagnetic Behavior of VSe_2

1.5.1 Introduction

Two-dimensional (2D) materials have attracted considerable attention due to their unprecedented potential in nanoscale devices, especially in fields such as spintronics and optoelectronics [34–36]. Their reduced dimensionality leads to unique physical properties not observed in their bulk counterparts, including tunable electronic structures, enhanced quantum confinement effects, and the possibility of manipulating magnetic order through external stimuli [37–40]. The discovery of

intrinsic ferromagnetism in atomically thin crystals such as CrI3 and Fe_3GeTe_2 has revolutionized the research landscape of 2D magnetic materials [41], [42]. These findings underscore the possibility of integrating 2D magnets into advanced spintronic architectures, where magnetism can be controlled by electric fields, gating, or strain [40], [43]. However, achieving stable and controllable room temperature ferromagnetism (RT FM) in 2D systems remains an ongoing challenge [34], [35].

In this context, VSe_2 has attracted special interest. A member of the transition metal dichalcogenide (TMD) family, VSe_2 displays interesting electronic and structural phase transitions, including charge density wave (CDW) states and possible magnetic ordering [26]. Despite theoretical predictions supporting ferromagnetic (FM) behavior in monolayer VSe2, the experimental picture remains far from clear, with conflicting reports in the literature [25], [47-52], [26]. Initial experimental observations suggested a magnetic moment in monolayer VSe_2 nearly an order of magnitude larger than typical ferromagnetic metals such as Fe and Co—an extraordinary claim, particularly when theory predicts a more modest magnetic moment of about 0.6 μB per ion [51]. This discrepancy has sparked intense research into the origins and tunability of FM behavior in ultrathin VSe_2, focusing on defects, molecular adsorption, and strain effects [53].

In this article, we provide an expanded overview of the debate

surrounding room-temperature ferromagnetism in VSe_2. We delve into the theoretical underpinnings, discuss the experimental evidence that both supports and challenges the notion of FM ordering, and explore the roles of strain, annealing, and defects. By piecing together these findings, we aim to clarify the nature of FM behavior in VSe_2 monolayers and identify directions for future research.

1.5.2 Theoretical Foundations of Ferromagnetism in VSe_2

Early Predictions and Mechanistic Insights

The prospect of ferromagnetism in VSe_2 monolayers was first seriously considered through theoretical work employing density functional theory (DFT) and other first principle approaches. Ma and Dai et al. [54] explored how the magnetic moment of VSe_2 depends on lattice strain and the presence of vacancies. They found that VSe_2 exhibits FM behavior when subjected to isotropic strain ranging from –5% to +5%. In these calculations, the magnetic moment is strongly influenced by modifications in ionic-covalent bonding, as strain alters the distance between V and Se atoms and effectively tunes the hybridization of electronic orbitals.

Such predictions, if confirmed experimentally, imply that monolayer VSe_2 could become an ideal candidate for strain engineering in spintronics applications, functioning as a tunable 2D magnet that complements the electronic properties of graphene [41], [55]. Moreover, theoretical models suggest that both through-bond and through-space interactions can contribute to stabilizing ferromagnetic order in VSe_2

[54]. The interplay between these interactions is particularly sensitive to lattice distortions, emphasizing the significance of fine structural control.

1.5.3 Role of Defects and Se Vacancies

Recent DFT studies have shed light on the importance of defects (especially selenium vacancies) in stabilizing the ferromagnetic phase in VSe_2 [53], [56]. Defects can introduce localized states that enhance magnetic coupling, effectively amplifying magnetic moments. The introduction of molecular species on the surface—through environmental exposure or controlled

chemical processes— can similarly modify the electronic structure and either enhance or diminish FM properties. These theoretical findings correlate well with experimental variations, highlighting why some samples exhibit strong FM signals while others remain nonmagnetic under seemingly similar conditions [61].

In addition to point defects, line defects and grain boundaries have been proposed as sites where local magnetic order may form [53]. Such structural imperfections can serve as nucleation points for magnetism by altering the local density of states and stabilizing spin polarization. Overall, the existing theoretical framework consistently underscores the interplay of strain, defects, and adsorbates as central to understanding the FM properties in 2D VSe_2.

1.6 Experimental Investigations and Conflicting Reports

The first experimental evidence of ferromagnetism in ultrathin VSe2

was reported by Xu et al. [57], who employed a wet-chemistry approach to grow few-layer VSe_2 (4–8 layers thick) on Si/SiO_2 substrates. They observed room-temperature ferromagnetic behavior, confirming the feasibility of Dai's theoretical predictions [54]. This initial breakthrough prompted further investigations worldwide, aiming to replicate, validate, or refute these findings in monolayer VSe_2.

However, the experimental scenario quickly became complicated. Cao et al. [59] reported the absence of FM order in laminated VSe_2 at room temperature, directly contradicting earlier observations. Their results suggested that variations in sample preparation or external conditions (e.g.,

vacuum environment, temperature, and substrate interactions) could drastically influence the magnetic behavior of VSe_2.

Subsequent studies reached similarly conflicting conclusions, reinforcing the notion that the magnetism in VSe_2 is highly sensitive to multiple factors— defect concentration, surface adsorbates, substrate choice, and measurement techniques. The lack of uniformity in sample synthesis and characterization underscores the challenges inherent in isolating the intrinsic magnetic properties of 2D VSe_2.

In 2018, Bonilla et al. [26] used molecular beam epitaxy (MBE) on highly oriented pyrolytic graphite (HOPG) and MoS_2 substrates to fabricate monolayer VSe_2. They conducted super- conducting quantum interference device (SQUID) and magneto-optical Kerr effect (MOKE) measurements, revealing definitive FM hysteresis at room temperature.

Further explorations by Feng et al. [50] and Chen et al. [51] employed X-ray magnetic circular dichroism (XMCD) to probe magnetic order with element-specific sensitivity. While Feng's results corroborated Bonilla's identification of RT FM, Chen's data indicated no detectable magnetic moment, exposing the extent of variability tied to sample conditions and substrate interactions. Such discrepancies underscore the critical need for standardized growth and characterization protocols.

1.7 Recent Developments

The debate over the presence of FM in VSe_2 continued with new techniques and refined experimental approaches. In 2019, Yu et al. used

chemical

exfoliation in conjunction with SQUID, XMCD, and magnetic force microscopy (MFM) to demonstrate RT FM in monolayer VSe2 [60]. Around the same time, Chua et al. [61] confirmed FM ordering via MBE growth, adding further credence to the notion of intrinsic magnetism in properly prepared samples.

Despite these confirmatory studies, research from 2021 to 2022 [36–38] continued to yield divergent outcomes. Some pointed to robust FM signals, while others found little to no magnetism. A recurring conclusion across many of these reports is that magnetic behavior is not dictated merely by the choice of substrate or growth technique but rather by a subtle interplay of intrinsic defects, molecular adsorption, strain, and potentially other less explored factors. Consequently, the consensus emerging is that VSe_2 is an intrinsically flexible magnet the properties of which can be modulated by multiple extrinsic and intrinsic parameters.

1.8. Strain, Annealing, and Defects Effects

1.8.1 Strain Effects

Strain engineering has emerged as one of the most powerful tools for modulating magnetism in 2D materials [55]. In the case of monolayer VSe_2, both experimental and theoretical evidence points toward a pronounced strain dependence of FM order [54]. By applying compressive or tensile strain in the range of ±5%, researchers observe notable changes in magnetic moment and coupling strength. Ma et al.

[54] attributed these shifts to modifications in ionic-covalent bonds, which directly impact the exchange interactions.

Experimentally, Ci et al. [56] introduced strain by bending flexible mica substrates coated with VSe2. They detected an increase in the magnetic moment under tensile strain and a corresponding decrease under compressive strain, aligning well with theoretical predictions. These findings illustrate that careful application of strain can tune the magnetic properties of VSe_2, presenting exciting possibilities for spintronic devices where mechanical manipulation or integration into flexible electronics is envisioned.

1.8.2 Annealing and Defects Effects

Defect engineering represents another critical pathway for controlling magnetism in VSe_2. Selenium vacancies in particular have been frequently implicated in stabilizing ferromagnetism [34], [53]. Xu et al. showed that controlled annealing could enhance the concentration of Se vacancies, thereby boosting the FM signal [53], [57]. DFT calculations lend support to these observations, demonstrating that localized states arising from vacancies can strengthen the ferromagnetic exchange interaction.

Chua et al. [61] introduced selenium-deficient defect lines through targeted annealing protocols. Using XMCD and MFM, they showed that these defect lines activated ferromagnetism in samples previously lacking any magnetic signal. This phenomenon opens the door to

purposeful "defect engineering"—tailoring the magnetic domain structure and over- all magnetization by controlling both the density and spatial distribution of vacancy-related defects.

Beyond selenium vacancies, other forms of local disorder, such as line defects, domain boundaries, and doping with foreign atoms, also have the potential to affect magnetism [61],[54] and [98]. Each of these variables— strain, defects, adsorbates— may work in concert or opposition, thereby creating a complex "phase diagram" for magnetism in VSe_2 that depends sensitively on external and internal conditions. Mastering this complexity is likely essential for designing devices based on VSe_2 or related TMD magnets.

1.9 Chronological magnetic study in correlation with the number of layers of VSe_2

1.9.1 Ferromagnetism in Ultrathin VSe_2 Nanosheets

In 2013, [57] exfoliated VSe_2 to create ultrathin nanosheets of about 4–8 layers and investigated their transport and magnetic properties. They observed a room temperature ferromagnetic response, which they attributed to an intrinsic mechanism coupled with a charge-density-wave transition.

This study provided early evidence that few-layer VSe_2 might exhibit ferromagnetism distinct from the well-known paramagnetic behavior of bulk crystals. • Layers:4–8 layers • Magnetism: Ferromagnetic (FM) • **Key Note**: First report suggesting that reducing VSe_2 thickness to the

few-layer regime could stabilize a ferromagnetic state.

1.9.2 No Ferromagnetism in Exfoliated VSe_2

In 2017, Cao et al., examined few-layer VSe_2 “laminates” obtained through mechanical exfoliation [59]. Their magnetic characterization showed no evidence of intrinsic ferromagnetism in the samples from room temperature down to low temperatures. Instead, a weak paramagnetic response associated with structural defects was observed. This contrasted sharply with the 2013 results, suggesting that sample quality and preparation methods might critically influence the magnetic outcome. • Layers: Few layer (³ 3) laminates • Magnetism: Non- Ferromagnetic (non-FM) • **Key Note**: Identified paramagnetism originating from defects; concluded there is no intrinsic FM in exfoliated few-layer VSe2.

1.9.3 Transport Studies Indicating No FM in Chemical Vapor Deposition (CVD) Few-Layers

In 2019, Liu et al. focused on high-quality few-layer VSe_2 nanosheets grown by chemical vapor deposition, covering thicknesses from approximately four layers up to tens of layers [63]. Magneto transport measurements revealed a weak antilocalization effect, suggestive of strong spin– orbit coupling, but no hysteresis or anomalous Hall effect. The absence of these signatures implied there was no ferromagnetic ordering in these samples. This work supported the viewpoint that pristine few-layer VSe_2 generally remains non-ferromagnetic under standard growth conditions. • Layers: 4 layers to tens of layers •

Magnetism:

Non-Ferromagnetic (non-FM) • **Key Note**: Reinforced the notion that ideal few layer VSe2 (CVDgrown) does not exhibit spontaneous ferromagnetism.

1.9.4 Room-Temperature Ferromagnetic Domains in Few-Layer VSe_2 In 2022, Ci et al. reported on few-layer VSe_2 flakes (^{3} 3 layers)

synthesized by CVD [56]. Using magnetic force microscopy, they observed clear ferromagnetic domains at room temperature in flakes thinner than about 6 nm (roughly up to 10 layers). Thicker samples exhibited a diminished magnetic response, indicating a thickness dependent crossover from a ferro- magnetic state to a more bulk-like, non-magnetic or weakly paramagnetic phase. They also demonstrated that strain engineering can tune the magnetic properties, suggesting an externally controllable mechanism for ferromagnetism in these 2D layers. • **Layers:** 3+ layers (up to 10). * **Magnetism:** Ferromagnetic (FM) in thinner flakes; vanishes in thicker ones. * **Key Note:** Revived the evidence for few-layer ferromagnetism at room temperature, highlighting strong thickness dependence and the role of strain.

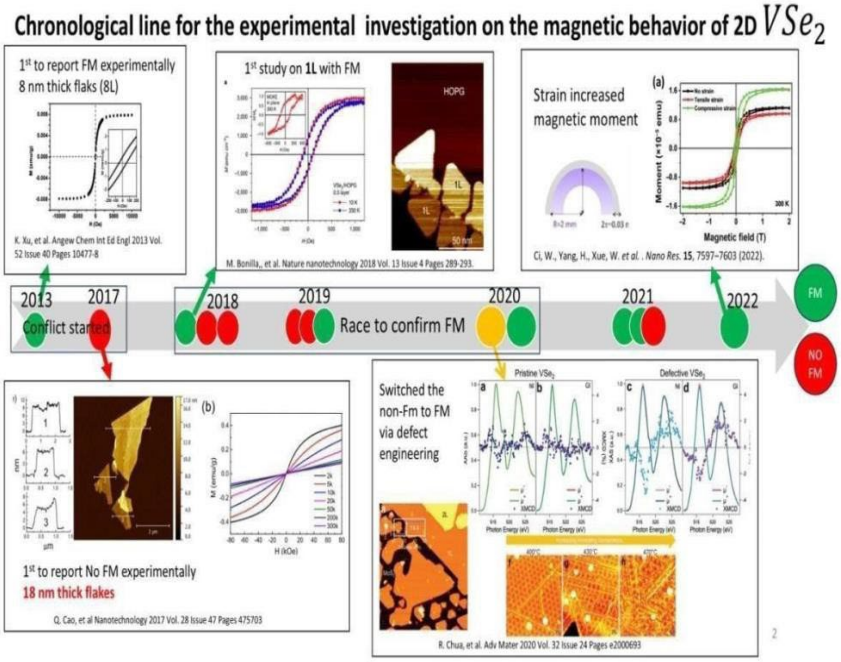


Figure 2: Chronological line for experimental investigation on the magnetic behavior of 2D VSe_2. The red circle indicates no FM detected, green FM. And

Yellow circle indicates a switch form non-FM to FM due to defect engineering.

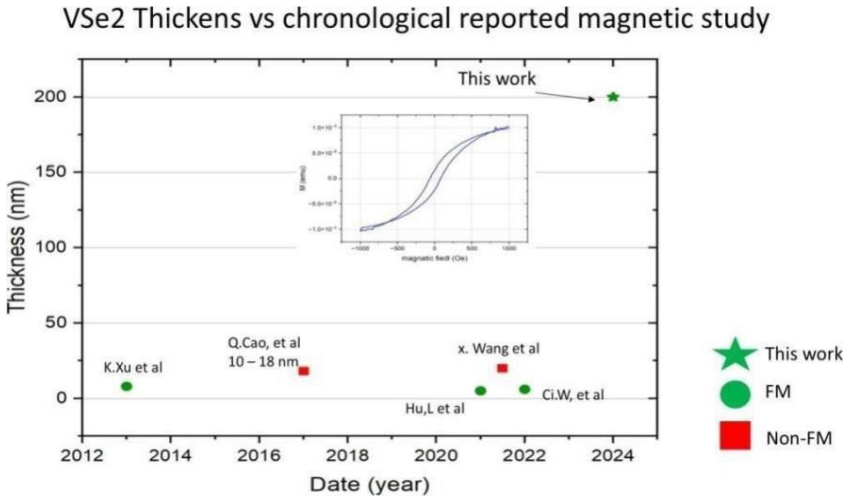


Figure 3: Thickness vs chorological magnetic study results. Maxum thickness with FM reported is 8nm until this work. Insite show the SQUID result of this work.

1.10 Prospects for Applications and Future Directions

The promise of 2D ferromagnets lies in their potential for low-power spin based devices [58]. If monolayer VSe_2 indeed supports robust FM order at or above room temperature, it could be integrated into next-generation data storage and logic devices where spin replaces or complements charge as the primary information carrier [35]. Moreover, the ability to modulate magnetism via strain or defect control paves the way for adaptive devices with reconfigurable magnetic states.

One compelling approach is the fabrication of heterostructures—layers of different 2D materials stacked together to form devices with customized properties [34]. Combining VSe_2 with other van der Waals materials (e.g., graphene, hBN) could enable proximity effects, where the magnetic

properties of VSe_2 induce spin polarization in an adjacent non-magnetic layer [13], [43]. Such coupling phenomena are already being explored in graphene- based spintronics, but the high Curie temperature needed for practical applications has made ideal 2D ferromagnets elusive. VSe_2 may fill this niche, provided the fundamental issues around reproducibility and sample variability are resolved.

1.10.1 Challenges and Research Gaps

Despite the excitement, the field faces numerous challenges. The variability in reported magnetic properties from one study to another

underscores the imperative for standardized protocols. Growth conditions, annealing temperatures, vacuum levels, and substrate choices must be carefully delineated to reproduce results consistently. Enhanced characterization techniques, such as correlative microscopy (combining MFM with XMCD or ARPES), could yield a more comprehensive picture of magnetic domains and electronic structure simultaneously [28-30].

Additionally, more systematic theoretical work is needed to map out the parameter space in detail. For instance, the interplay between large- scale strain (tensile or compressive) and local defects, remains insufficiently understood. Similarly, the role of chemical doping, such as substituting vanadium with another transition metal, could unlock or suppress ferromagnetism in ways not yet fully explored [53]. Achieving precise control over doping or defect density at the atomic scale will be crucial for device applications, and advanced nanofabrication methods may

be required to realize these goals. Moving forward, collaborative efforts that integrate predictive theory, high-quality materials synthesis, and cutting edge characterization will be key to unraveling the full potential of monolayer VSe_2. A more thorough understanding of its ferromagnetic properties may position this TMD at the forefront of 2D spintronics research. Whether or not VSe_2 ultimately becomes a standard-bearer for 2D magnets, the knowledge gained from studying its strain- and defect-tunable magnetism will undoubtedly inform the design and discovery of

new 2D ferromagnetic materials.

1.11 Conclusions

VSe2 exemplifies both the promise and the challenges of 2D magnetism research. Theoretical predictions indicate it should exhibit a moderate magnetic moment under certain strain conditions, while experimental data have suggested moments far exceeding those of many known ferromagnets. This striking contradiction has driven extensive investigations into how defects, strain, and adsorbates modulate magnetic ordering. Although significant discrepancies persist in the literature, a broad consensus is emerging that extrinsic factors—rather than purely intrinsic properties— dominate the observed FM signals.

The next phase of VSe_2 research requires systematic studies that carefully control growth parameters, defects, and external stimuli. These efforts, coupled with state-of-the-art computational models, are essential to confirming the existence (and mechanism) of robust RT FM in monolayer VSe_2. If such ferromagnetism can be reliably established and engineered,

VSe_2 may find wide applications in spin-based devices, catalyzing innovations in 2D spintronics and beyond.

2. Procedures and Results

This chapter will explain the experimental setup, after which we will detail our results, specifically our detection of a record-breaking thickness for VSe_2 with ferromagnetism at room temperature. In the second section we show the significance of this discovery

for designing magnetic materials by developing our own hybrid fabrication method for selective etching on VSe_2. In addition, in this section we show the results of fabricating an oxide layer of V_2O_5 on top of the VSe_2 flake with a micropression and explain the selective process for etching using ICP plasma for two different gases (CL and CF4). This discussion is followed by a demonstration of the effectiveness of this hybrid method by showcasing MFM data for the selective area that was etched, which demonstrates a higher magnetic movement. Finally, we present a DFT simulation correlating the Se vacancies with local lattice strain and argue that this strain could be the underlaying reason for having an FM behavior for VSe_2.

2.1 Experimental Setup

In this chapter, the experimental procedures for laser treatment and plasma etching of vanadium diselenide (VSe_2) flakes are described. The goal is to achieve localized oxidation, evaporation, or thinning of the material by combining a **confocal Ramanbased laser setup** with **selective plasma etching**. Subsequently, a variety of **characterization methods** are introduced to evaluate structural, magnetic, and compositional properties of the treated samples. Specific process parameters, such as laser power ranges, plasma gas flow rates, and instrument calibration details, are deferred to the comprehensive methodology section
(Chapter 5) to maintain clarity.

Laser Treatment System

The laser processing stage is centered on a confocal Raman spectroscopy instrument equipped with a 785 nm laser source and a 50× objective lens, which produces a spot size of approximately 1 μm on the sample surface. By mounting exfoliated VSe_2 flakes on a 300 nm SiO_2/Si wafer, it becomes

possible to perform localized oxidation or evaporation of VSe_2 simply by varying the laser power, dwell time, and scanning step size. One significant advantage of this setup is **in situ** measurement capability: the Raman spectrometer collects backscattered light immediately from the same region undergoing laser treatment, allowing real-time monitoring of potential phase changes, surface oxidation, or thickness alterations.

A schematic of the confocal arrangement (referenced in Figure 1) illustrates how the laser beam is focused onto the VSe_2 surface through the objective lens, while a beam splitter and optical route the scattered signal into the spectrometer. To achieve precise control over pattern dimensions and ensure uniform laser exposure, the system utilizes motorized stages with submicron resolution. By systematically adjusting parameters such as power output, scanning speed, and repetition, the experiment can induce partial or complete oxidation, targeted evaporation, or patterning of the VSe_2 layer.

Plasma Etching Equipment

After the laser modifications, the samples undergo one or more plasma etching processes to remove either the newly oxidized material or sections of pristine VSe_2. Three different plasma systems are employed, each chosen for its unique

gas chemistry and ion density profile. First, a **radio frequency (RF) plasma etcher** utilizing a mixture of Ar, N_2, and O_2 offers lower ion energies, allowing gentler surface modification or oxidation. Second, an **ICP plasma etcher** based on fluorinecontaining gases (e.g., SF_6 or CF_4)

supports more aggressive, anisotropic etching, which is especially useful for removing specific compounds or achieving deeper trenches. Third, a **chlorine-based ICP etcher** provides alternative selectivity and etch profiles by introducing Cl_2 or similar chlorine gases into the plasma.

In each case, parameters such as gas flow rate, RF or ICP power, chamber pressure, and etch duration determine the final etch rate and selectivity. By iteratively combining laser processing and plasma etching, it becomes possible to produce finely tuned thickness variations, patterned regions, or complete removal of upper layers in a controlled manner. Detailed operational recipes (e.g., flow rates, pressures, and power levels) are cataloged in the methodology section, enabling reproducibility and optimization for future work.

Characterization Methods

A suite of **characterization tools** is used to assess the success of the laser treatment and plasma processes, focusing on morphological changes, thickness profiles, magnetic behavior, and elemental composition. **Scanning Electron Microscopy (SEM)** is first employed to provide an overview of surface morphology and to reveal contrast differences between etched and unetched regions. With magnifications reaching sub-100 nm resolution, SEM easily identifies microscale defects and verifies whether the laser-induced patterns have uniform boundaries or exhibit partial over-etching.

To obtain quantitative thickness and roughness data, **Atomic Force Microscopy (AFM)** is used. Depending on sample stability, either tapping or contact mode can be selected, yielding high- resolution height profiles

across the laser-treated or plasma-etched zones. Coupled with AFM is **Magnetic Force Microscopy (MFM)**, which employs a magnetized probe to sense local magnetic fields. By scanning the same surface areas assessed by AFM, MFM reveals the distribution of magnetic domains or variations in magnetic moment correlated with flake thickness or processed regions.

Complementing these local imaging methods, **Superconducting Quantum Interference Device (SQUID)** magnetometry allows for highly sensitive, bulk-level magnetic measurements. This technique quantifies magnetization as a function of temperature or external magnetic field, establishing clear evidence of ferromagnetism in the samples if present. Meanwhile, **Magneto-Optical Kerr Effect (MOKE)** measurements offer a surface-sensitive view of the magnetic hysteresis loop, providing an additional handle to distinguish surface magnetism from bulk effects. In many cases, SQUID and MOKE data are combined to yield a fuller picture of both intrinsic (bulk) and surface-driven magnetic phenomena.

Finally, **confocal Raman spectroscopy**—initially integral to the laser treatment—also serves as a post-processing analytical method, detecting shifts in vibrational modes associated with oxidation, selenide deficiencies, or material removal. By comparing spectra before and after plasma etching, one can confirm the removal of specific phases or verify the persistence of VSe_2 peaks in the patterned zones. For additional compositional insight, **Energy Dispersive X-ray Spectroscopy (EDS)** is performed (often in conjunction with SEM) to confirm elemental changes, such as reduced selenium content

or increased oxygen in treated regions. Although EDS is semi-quantitative, it provides reliable secondary confirmation of the chemical states suggested by Raman.

In conclusion, the experimental workflow integrates a **confocal Raman based laser system** for precise modification of VSe_2 and multiple **plasma etching** platforms for further layer control. Characterization through

SEM, AFM, MFM, SQUID, MOKE, Raman, and EDS ensures a comprehensive analysis of the morphological, magnetic, and compositional transformations resulting from each process. Detailed process parameters, including laser power, etch recipes, measurement settings, and data processing protocols, are presented in Chapter 3. This multifaceted approach provides a robust framework for fabricating and examining customized 2D structures of VSe_2 for advanced device applications.

2.2 Summary of the results

This study has discovered ferromagnetism (FM) at room temperature in VSe_2 flakes with an unprecedented thickness of ~300 nm. Previously, FM had only been reported in VSe_2 samples down to ~8 nm, making our observation at essentially bulk-like thickness both novel and significant.

Sample Fabrication and Characterization. VSe_2 crystals, grown via chemical vapor deposition (CVD) by collaborators, were mechanically exfoliated onto Si/SiO_2 substrates (300 nm oxide). The high quality of these flakes is confirmed by optical microscopy and Raman spectroscopy prior to magnetic measurements. **SQUID Magnetometry Results.** SQUID

measurements (with in-plane applied field) reveal a clear ferromagnetic hysteresis loop (see Figure 44a), unambiguously confirming room-temperature FM in 300 nm-thick VSe_2.

Implications.

1. The ability to sustain FM in much thicker crystals simplifies device fabrication by obviating the need for extremely thin, fragile flakes.
2. The total magnetic moment in device or heterostructure designs can be tuned by adjusting thickness—creating new opportunities in spintronics and magnetic materials.
3. The observation of FM in 300 nm-thick samples implies a defect-mediated or strain- assisted mechanism that is robust across a wide range of thickness scales, shedding new light on the origin of magnetism in VSe_2. Figure 46 compares literature data (showing ferromagnetism in thinner flakes) to our results on 300 nm-thick samples, highlighting a similar hysteresis behavior with an order of magnitude greater thickness.

A key outcome of this dissertation is the development of a **hybrid method** that couples **laser- driven oxidation** with **selective plasma etching** to sculpt and functionalize van der Waals materials. We illustrate this using VSe_2, demonstrating how vanadium oxides (primarily V_2O_5) can serve as a plasma resistant mask—or be selectively removed—depending on the chosen plasma chemistry.

2.2.1 Laser-Induced Oxidation and Evaporation of VSe_2

Immediate Evaporation at High Power. Exposing VSe_2 flakes to a 100 mW laser for even 1 s triggers local evaporation, creating visible damage (Figure 5). Two treatment spots ~10 μm apart reveal total vaporization at

the center

and a ring-like oxide layer surrounding the beam center

Extended Laser Exposure. Increasing the treatment time to 5 minutes (Figures 6 and 7) leads to more pronounced oxidation around the laser spot. Raman spectra confirm growing intensities of oxide- related peaks, highlighting the formation and evolution of multi-phase vanadium oxides.

Formation of Vanadium Oxides. A distinct oxide ring (~8 μm from the center) contains VO_2, V_2O_3, and V_2O_5, gradually transitioning toward a more stable V_2O_5 phase over 24 hours. The ~140 cm^{-1} peak (VO_2/V_2O_5) and the diminishing 255 cm^{-1} VO_2 feature suggest progressive oxidation to V_2O_5 [1&2]. **Air Exposure vs. Inert Environment.** Storing samples in a glovebox slows but does not halt the conversion to oxides—selenium vacancies created by the laser continue to be filled by oxygen over time. Upon re-exposure to air, new broad peaks (240 cm^{-1}, 235 cm^{-1}) appear, indicating additional oxide formation (Figures 8, 9) [64], [65]. **Laser Mapping and Controlled Oxide Growth.**

Intermediate laser powers (e.g., 25 mW for 1 minute) reproducibly yield V_2O_5 on top of VSe_2 without destroying the underlying layers (Figures 9, 10). The distinct A_1g VSe_2 peak at 207 cm^{-1} remains visible, confirming the integrity of the buried VSe_2.

H_2 Annealing. Similar oxide layers can be produced by furnace annealing. Unlike local laser annealing, however, furnace oxidation affects the entire flake. Raman peaks (e.g., at 994 cm^{-1}) confirm V_2O_5 formation, with sharpness varying by oxide thickness. Critically, the VSe_2 A_1g mode at 207 cm^{-1} indicates the surviving underlying layer.

2.2.2 Heat Transfer Effects and Edge Oxidation

Edge Effects. Despite focusing the laser at the flake center, oxidation often appears more aggressively at flake edges (Figures 5–9, 17–18). This phenomenon stems from **in-plane heat conduction**: thinner edges dissipate heat less effectively, driving higher local temperatures and promoting oxidation/evaporation.

Simulation Insights. Thermal modeling (Figures 15, 16) demonstrates that going from 100 nm to 50 nm thickness can double the local temperature. Accordingly, edges and corners—where the flake tapers—heat up more and oxidize or evaporate first. EDS analysis also detects SeO_x byproducts at edges, confirming localized decomposition.

2.2.3 Plasma Etching of VSe_2 and V_2O_5

Radio frequency (RF) plasma cleaning initially showed no significant impact on VSe_2, apart from removing tape residue coupled plasma (ICP) etching, with increased ion density and higher RF power, was then explored to achieve effective removal of VSe_2 layers or oxide layers.

ICP Advantages.

1. **High Plasma Density** (10^{11}–10^{12} cm^{-3}), supporting faster etch rates and uniform processes.
2. **Decoupled Ion Energy** (source vs. bias power), reducing damage to delicate 2D materials.
3. **Chemical Versatility** (Cl_2, BCl_3, CF_4, SF_6, etc.) for selective etching of different compounds.

Chlorine-Based Etching of Bulk VSe_2. Chlorine plasma effectively etches VSe_2 (Figure 25). A 10 s recipe with BCl_3, Ar, and Cl_2 at suitable

power can remove up to ~300 nm, as confirmed by AFM thickness measurements and decreased Raman peak intensity (Figures 26, 27).

Comparing VSe_2 vs. V_2O_5 in Chlorine Plasma. By contrast, V_2O_5 etches more slowly under the same Cl_2-based conditions (Figures 28, 29). Extended etch times still show strong V_2O_5 signatures, revealing that vanadium oxide can act as a **hard mask** against Cl_2 plasma. Figure 30 highlights a flake first laser treated to form an oxide region, then subjected to Cl-based ICP for 10 s. The untreated VSe_2 is fully etched, while the oxide region remains. EDS confirms minimal Se content and abundant V–O in the masked area, and Raman identifies V_2O_5. This result proves **Chlorine Plasma Selectivity**: laser created V_2O_5 protects underlying VSe_2 in designated areas.

Conversely, CF_4-based ICP can **rapidly remove V_2O_5**, while leaving VSe_2 relatively intact (Figures 31–32). The oxide is eliminated, as shown by the disappearance of V_2O_5 peaks in Raman post- etch, whereas the original VSe_2 A_1g mode remains visible. EDS confirms the removal of oxide in most regions. Thus, V_2O_5 and VSe_2 exhibit inverted selectivities in Cl- vs. F-based plasmas: **Cl-Plasma:** Rapid VSe_2 etch, slower V_2O_5 removal → oxide can protect underlying VSe_2. **CF_4-Plasma:** Rapid V_2O_5 etch, comparatively slower VSe_2 removal → oxide can be selectively stripped.

By **first forming V_2O_5** locally (e.g., via laser or furnace annealing) and **then applying Cl_2 or CF_4 plasmas**, one can selectively etch either VSe_2 or its oxide cap. This modular, top-down process enables complex patterning

or protective masking in **2D van der Waals** materials, demonstrated here with VSe_2/V_2O_5 as a proof.

2.2.4 Post-Etch Magnetic Behavior and Theoretical Insights

Plasma thinning of VSe_2 can accentuate magnetic properties, especially near edges where the etching is most pronounced (Figures 33, 36–38). Atomic force microscopy (AFM) maps show local reductions in thickness to ~14–20 nm, while **magnetic force microscopy (MFM)** reveals bright, high-moment areas in these ultra-thin regions (Figures 37, 38, 40).

Thickness Dependence. MFM contrast is strongest at edges or thinner locations, indicating an increase in the local magnetic moment.

Possible Mechanisms. Selenium vacancy formation, strain relaxation, and local distortion may boost FM order in thinner domains of VSe_2.

2.3. Theoretical Correlation Between Vacancies, Strain, and Magnetism

Density functional theory (DFT) calculations and model simulations support a link between Se vacancies, tensile strain, and enhanced magnetic moments (Figures 39– 45, 47):

1. Se Vacancies

   Introducing 1–10% vacancies in a 2×2 lattice increases the magnetic moment nearly twofold, with partial Jahn–Teller (JT) distortions stabilizing the spin polarization.

2. Strain Engineering

   Both compressive and tensile strain can shift the V 3d states near the Fermi level, altering spin splitting and leading to variations in the net magnetization. A Jahn–Teller mechanism can lift orbital degeneracies, even

with a nominal single d1d^1d1 electron configuration for vanadium, thereby stabilizing higher spin states. Overall, **plasma-thinned VSe_2** likely harbors a dense population of Se vacancies and local strain fields that collectively enhance FM response.

This synergy between top down fabrication and intrinsic quantum phenomena paves the way for **strain- and vacancy-engineered spintronic devices**.

2.4 Results Section

2.4.1 FM at RT for thick VSe_2

This study has discovered ferromagnetism (FM) at room temperature in VSe_2 flakes with an unprecedented thickness of ~300 nm. Previously, FM had only been reported in VSe_2 samples down to ~8 nm, making our observation at essentially bulk-like thickness both novel and significant. In this work, we demonstrate a breakthrough discovery of robust ferromagnetism in VSe_2 at an unprecedented thickness of ~300 nm. The VSe_2 crystals were grown via chemical vapor deposition (CVD) by collaborators and mechanically exfoliated onto Si/SiO_2 substrates with a 300 nm oxide layer, yielding large high quality flakes [64]. SQUID magnetometry measurements (with the field applied in plane) revealed a clear ferromagnetic hysteresis loop (Figure 44a), unequivocally confirming in-plane ferromagnetic order at room temperature. This result dramatically extends the known thickness range for VSe_2's ferromagnetic behavior: previously, ferromagnetism had only been reported in much thinner samples (~8 nm) [3], making the observation at 300 nm (essentially bulk-

like) unprecedented. Notably, this finding has several important implications. First, the ability to observe FM in a much thicker VSe_2 crystal greatly simplifies the fabrication of FM-based devices by eliminating the need for extremely thin and delicate layers. Second, it enables new opportunities in the design of magnetic materials and heterostructures, where one can modulate the total magnetic moment by controlling the number of VSe_2 layers. Third, sustaining FM at such a large thickness provides insight into the origin of magnetism in VSe_2, suggesting that defect-induced

mechanisms may be responsible for the emergence of ferromagnetism at different thickness scales. Figure 46 shows a comparison between current litterateur data and our results. We show similar magnetic moment with a hysteresis however our samples are 100X thicker.

2.4.3 Hybrid fabrication method

Effect of High-Power Laser Treatment on VSe_2

When subjected to high-power laser treatment at 100 mW for even 1 second, the VSe_2 flake undergoes immediate evaporation, as shown in Figure 5. It this figure it can be see a clear sign of damage. To investigate the effects of laser induced modification, the sample was treated at two locations approximately 10 μm apart. The results indicate that at the center of the laser treatment zone, complete evaporation of VSe_2 occurred, while a surrounding ring exhibited the presence of an oxide layer.

To further confirm the formation of oxides around the laser-treated region, a second experiment was conducted with an extended laser

exposure time. By increasing the treatment duration, we aimed to observe changes in the flake's surface and oxidation behavior. In Figures 6 and 7, where the laser treatment duration was increased to 5 minutes, the results provide further insights into the oxidation dynamics and material transformation induced by prolonged laser exposure.

Oxidation Dynamics and Stability of Vanadium Oxide

A visible ring surrounding the laser treatment zone can be observed, extending approximately 8 μm from the center. A Raman measurement taken at this distance confirms the presence of vanadium oxide. However, in this

experiment, the sample was exposed to air for 24 hours, and the results indicate increased surface degradation and a higher intensity of VO_x peaks [64], [65]. This suggests that laser treatment induces selenium vacancies, which, upon air exposure, become filled with oxygen, leading to further oxidation. Another significant observation is the emergence of a peak around 140 cm^{-1}, associated with both VO_2 and V_2O_5, along with the disappearance of the 255 cm^{-1} peak, which is primarily linked to VO_2 111. This transformation suggests that the oxide layer is undergoing a phase transition, shifting from a mixture of oxides toward a more thermodynamically stable V_2O_5 form [64], [65]. To further analyze these spectral changes, a high-resolution Raman spectrum was recorded after 24 hours of air exposure, as presented in Figure 6. This detailed examination provides deeper insights into the oxidation state evolution and stability of the oxide layer over time. It can be observed that the region at the center and a few 3 to 6 um away shows the signature peaks of V_2O_5, which lead us

to conclude that at first the oxide regions is a combination of vanadium oxides (VO_2, V_2O_3 and V_2O_5) but after time they will switch to a more stable form of V_2O_5 [64], [65].

An additional experiment was conducted to examine the degradation behavior of VSe_2 following laser treatment. Using the same parameters as in Figure 8 (100 mW for 5 minutes), the treated flake was immediately placed inside a glovebox to minimize exposure to ambient conditions. The results are presented in Figure 8.

From Figure 8, it is evident that after storing the sample in the glovebox for three days, the presence of oxide is significantly lower than that observed when the sample was left in ambient conditions for one week.

However, the Raman spectra indicate a continuous increase in oxide peak intensity even within the glovebox environment. This suggests that selenium vacancies created during the laser treatment were gradually filled with oxygen, leading to further oxidation over time.

A particularly noteworthy observation was made after removing the sample from the glovebox and exposing it to air. The Raman spectra, shown in Figure 9, revealed the appearance of a broad double peak at approximately 240 cm^{-1} and 235 cm^{-1}. Although the resolution of these spectra is limited, they still indicate a distinct change in the oxidation state of the material.

Mapping Laser Treatment and Oxide Formation

Next, we present the results of a laser mapping treatment to fabricate an oxide layer on the surface of 2D VSe_2. This analysis also provides deeper insights into the specific types of oxides formed on the surface. Figures 8

and 9 illustrate the spatial mapping of laser-induced oxidation on VSe_2, highlighting the distribution and characteristics of the oxide layer.

The appearance of a layer of oxide on top of the flake can be seen. Figure (9) shows the Raman peaks of the treated area vs the non-treated area. The Raman spectra of the treated area, shown in Figure 9, were acquired immediately after laser treatment and exhibit a combination of VO_2 and V_2O_5 spectral features [64], [65]. This indicates that the oxidation process initially produces a mixture of vanadium oxides. However, when using an intermediate laser power with a longer treatment duration, the results become more stable. As shown in Figure 10, a sample treated with 25 mW laser power for 1 minute exhibits Raman peaks characteristic of V_2O_5, confirming the successful and consistent formation of the oxide layer under these conditions. This

observation clearly indicates that our controlled laser treatment is capable of producing a V_2O_5 layer on top of VSe_2. This conclusion is supported by the presence of the A_1g peak at 207 cm^{-1} in the treated area, which confirms that the underlying VSe_2 layer remains intact beneath the oxide layer. We can also produce similar results using controlled annealing for the whole substrate.

However, unlike the laser treatment the entire flak and sample would be oxidized.

Figure 10 shows the signature peak of V_2O_5 at 994cm^{-1} [64], [65]. A second annealing experiment has taken place under the same conditions as the H_2 annealing only without the H_2 gas.

The Raman spectra reveal a characteristic peak at 994 cm^{-1},

confirming the presence of V_2O_5. Additionally, by comparing the sharpness of the two spectra, it is evident that the black spectrum, corresponding to a thicker V_2O_5 layer, exhibits sharper and more well-defined peaks than the red spectrum. This observation indicates a variation in oxide thickness across the sample. Most importantly, the A_1g peak at 207 cm^{-1}, characteristic of VSe_2, remains strong, providing clear evidence that a VSe_2 layer persists beneath the V_2O_5 layer.

We have demonstrated a novel approach for fabricating V_2O_5 layers on VSe_2 using two distinct methods: controlled laser-induced local annealing and large-scale furnace annealing. These techniques offer precise control over oxidation processes, enabling the formation of V_2O_5 while preserving the underlying VSe_2 structure.

Heat Transfer Effects

During our laser-induced local annealing treatment, an intriguing phenomenon was observed. As illustrated in Figures 5, 6, 7,8, and 9, significant effects can

be seen at the edges of the flake, despite the treatment being applied several microns away. This effect can be attributed to heat transfer mechanisms.

As heat propagates in all directions, it encounters variations in layer thickness. When reaching the edges, where the number of layers is lower, the thermal effects—such as oxidation or evaporation—become more pronounced due to the reduced capacity for heat dissipation. To further validate this explanation, we present simulation results based on heat transfer analysis, demonstrating the correlation between localized heating

and its impact on the thinner edge regions.

Figure 15 demonstrates that as the number of layers is decreased the temperature would raise quadratically. Going from 100 nm thickness to 50nm the temperature would raise by double.

Figure 16 presents a simulation of a VSe_2 flake with a thickness of 100 nm at the center and 10 nm at the bottom edge. When laser treatment is applied at the center, the heat transfer extends toward the bottom, as indicated by the temperature profile. The simulation results reveal that the temperature is significantly higher at the bottom edge, where the flake is thinner, due to the reduced capacity for in- plane heat dissipation. Further details regarding the simulation methodology and parameters can be found in the Appendix.

In Figure 17, experimental results demonstrate that oxidation and evaporation initiate at the edges of the flake. This observation aligns with the simulation, confirming that thinner regions experience higher localized temperatures, making them more susceptible to oxidation and material loss. We keep moving the treatment area (in red) lower everything and oxide would

grow from the edge first.

In Figure 18, it is evident that the treatment effect extends to the edge and right corner of the flake in the optical image. This can be attributed to the reduced thickness of the flake in these regions. With fewer layers, heat accumulation becomes more pronounced due to the limited capacity for in- plane heat dissipation. The heat transfer between the bottom flake and the SiO_2 substrate remains constant, while the in-plane thermal

conductivity of VSe_2 is higher than that of SiO_2.

Consequently, in thicker regions of VSe_2, heat is more effectively dispersed laterally. However, in thinner regions, the reduced in-plane heat transfer leads to localized temperature buildup, resulting in greater oxidation and/or evaporation at specific edges of the flake. Further details regarding the thermal calculations and modeling can be found in the Appendix. Another notable phenomenon observed was the formation of SeO_x particles at the edge of the VSe_2 flake following laser treatment. Due to the heat propagation towards the edges, where temperatures are higher, VSe_2 undergoes localized melting and evaporation, leading to the deposition of SeO_x particles. This dispersion, visible as a light green spread in Figure 16, indicates the redistribution of selenium and oxygen species. Energy dispersive spectroscopy (EDS) analysis confirms that these particles consist of selenium and oxygen in compound form, further supporting the occurrence of thermal decomposition and oxidation at the flake's periphery.

Plasma etching:

Plasma-based etching techniques play a **critical role** in defining the geometry and functionality of micro- and nano-scale device components across a broad range of applications, including microelectronics, optoelectronics, energy
storage, and spintronics. **Transition metal compounds**— particularly those exhibiting **van der Waals bonding**—have attracted widespread attention due to their **unique layered structures** and the tunability of their electronic, optical, and magnetic properties [66]. Specifically, the

compounds **vanadium selenide (VSe_2)** and **vanadium pentoxide (V_2O_5)** are promising for next- generation devices and energy-related applications, owing to their diverse range of **electronic band structures**, **oxidation states**, and **cation-intercalation capabilities** [68-70].

In parallel, **Inductively Coupled Plasma (ICP)** etching has emerged as an advanced top-down microfabrication technology. ICP systems leverage **high density plasma** to produce a robust supply of reactive species and ions, enabling precise material removal through a combination of **chemical reactions** and **ion assisted bombardment**. The **key advantage** of ICP over more traditional reactive ion etching (RIE) lies in its ability to **decouple** plasma density from ion energy, thereby minimizing sample damage while maintaining high etch rates [71-73].

The endurance of VSe_2 under plasma:

Initially, a simple radio frequency (RF) plasma cleaning approach was employed to investigate potential surface modifications in VSe_2. As shown in Figure 20, RF plasma treatment did not produce any observable effects on the VSe_2 surface.

The only noticeable change was the removal of tape residue from the substrate. Subsequently, inductively coupled plasma (ICP) etching was utilized to enhance ion generation and apply higher RF power, enabling a more effective plasma interaction with the material.

Significance of ICP Etching

High Plasma Density: ICP can achieve electron densities in the range of 10^{11} – 10^{12} cm^{-3} enabling faster etch rates and more uniform processes [74].

Reduced Ion Energy: By separating the source power (for plasma generation) from the bias power (for ion energy control), damage to the substrate and underlying layers is minimized, crucial for delicate 2D materials.

Chemical Versatility: ICP etching can be conducted with a range of halogen gases (Cl_2, BCl_3, CF_4, SF_6, etc.), offering **selectivity** between materials by exploiting differences in byproduct volatility and reaction kinetics [75].

The Raman results show no change on the surface that can be detected. The main effect can be observed when using long etching time or higher powers. In Figure 20 and 22 we repeated the experiment only this time we have increased the time up to 5min and 10 min and the effects can be seen.

Although the substrate exhibits clear signs of etching, the bulk of the VSe_2 sample remains largely unaffected, even after prolonged etching durations.

This observation, combined with the Raman spectroscopy results, suggests that VSe_2 possesses exceptional resilience to plasma etching. Such stability highlights its potential for applications in high-temperature environments and extreme conditions, where structural integrity and durability are critical.

Selectivity of etching: A major challenge in utilizing TMDs and related vanadium-based layered materials for large-scale device

production is the lack of reliable top-down processes that allow patterning, doping, and functionalization.

A crucial objective of this work is to present a hybrid approach:

1. **Confocal Laser Process**: Transform part of VSe_2 into V_2O_5 **in situ**, creating a robust oxide layer that can serve as an **etch mask**.
2. **Selective Plasma Etching**: Utilize the differences in reactivity between VSe_2 and V_2O_5 under different halogen chemistries (Cl_2 vs. CF_4) to **sculpt** the underlying layered structures.
3. **Easy Mask Removal or Thinning**: Leverage the different plasma chemistries to **remove or retain** the oxide layer as needed, enabling flexible design pathways. Such an approach can be extended beyond just VSe_2/V_2O_5 to other **hybrid layered systems**, thus paving the way for novel applications in **energy storage**, **spintronics**, and **sensing** platforms.

For our purposes we aim to selectively etch specific areas of the flakes, those that have been laser treated. After observing the effect of plasma treatment on the sample, an ion reaction must take place to assist with the etching. We will be using two main ions: F^- and Cl^-.

Etching VSe_2:

Before we start, we would like to discuss the idea of volatility and how we can achieve selectivity with this material.

1. VSe_2 **in Cl_2 Plasma**

High Volatility of Selenium Chlorides: When VSe_2 is exposed to a chlorine rich plasma, selenium in the lattice readily forms **selenium**

chlorides such as $SeCl_2$ or $SeCl_4$, which can **sublimate or vaporize** at modest temperatures under plasma conditions. The removal of selenium, in tandem with the formation of volatile vanadium chlorides (e.g., VCl_2, VCl_3), drives an overall **strong etch reaction** [76]. **Thermodynamic Favorability**: The Gibbs free

energy (ΔG°) for generating these halide byproducts is significantly **negative** at typical plasma temperatures, indicating that once the reaction is initiated— often assisted by ion bombardment—etching proceeds readily, *go to appendix B for more details*.

2. **V_2O_5 in Cl_2 Plasma**

Oxychloride Formation: V_2O_5 can also be etched by chlorine, primarily through the formation of **vanadium oxychlorides** (e.g., $VOCl_3$). These may exhibit decent volatility; however, the **oxygen** in V_2O_5 can lead to **stable suboxides** or partially chlorinated residues that require more energetic bombardment or longer etch times to remove [78].

Masking Effect: Under certain process windows, the net removal rate of V_2O_5 in Cl_2 can be slower compared to that of VSe_2. Consequently, V_2O_5 can serve as an **etch mask** in chlorine plasma to protect underlying VSe_2.

3. **V_2O_5 in CF_4 Plasma**

Volatile Fluoride Routes: In fluorine-rich plasmas, V_2O_5 tends to form **VF_x** or **VOF_y** species, many of which can be driven off at modest process temperatures. These pathways facilitate a **faster net removal** of the oxide compared to some chlorine-based reactions, depending on plasma conditions [79].

Oxyfluoride Passivation vs. Removal: While initial oxyfluorides might momentarily **passivate** the surface, sufficient ion energy (bias power) and radical density in ICP can break these layers down, leading to continuous etching [80].

4. VSe_2 **in** CF_4 **Plasma**

Formation of SeF_x **and** VF_y: Fluorination of VSe_2 can produce volatile selenium fluorides (SeF_4, SeF_6) and vanadium fluorides (VF_5), [76]. Ultimately, selenides like VSe_2 often yield **highly volatile** selenium halides ($SeCl_4$, SeF_6), making them generally easier to **etch quickly**. Meanwhile, **oxides** such as V_2O_5 may demand more precise tuning of **plasma chemistry** and **ion energy** to break down or remove stable oxyhalides. This difference underpins the two-step **hybrid fabrication** strategy where VSe_2 is selectively etched in chlorine plasma (with V_2O_5 acting as a robust mask), followed by CF_4 etching to remove or thin the V_2O_5 layer, facilitating **complex device architectures** in vanadium based 2D materials. For more detailed and calculations see the appendix.

Etching VSe_2

Using gasses BCL_3 (20sccm), Ar (10sccm) and CL_2 (60 sccm). And RF power of 100W and ICP power of 800W for 10s. we were able to etch up to 300 nm of VSe_2 as can be shown in Figure 25.

Although the optical images suggest a non-uniform etching process, this is likely attributed to the initial variations in flake thickness rather than inconsistencies in the etching itself. This conclusion is supported by atomic

force microscopy (AFM) measurements taken before and after etching, which reveal only minor nonuniformity in the analyzed region. Additionally, the 3D AFM images indicate that the surface remains smooth and clear following the etching process.

Another significant observation confirming the thinning effect is the Raman spectra recorded before and after etching. Notably, the A_1g peak of VSe_2 at 207 cm^{-1} exhibits no shift, and no additional defect-related peaks are detected, demonstrating the nondestructive nature of the plasma etching process.

Furthermore, the intensity of the A_1g peak decreases by a factor of three, correlating wit reduction in layer thickness from approximately 400 nm to 100 nm. Figures 26 and 27 provide a more detailed analysis of these results.

Chlorine Plasma Etching of V_2O_5

The same chlorine (Cl) plasma etching recipe was applied to an annealed VSe_2 sample (V_2O_5), with the treatment duration extended to 1 minute. Figures (28 & 29) presents an annealed VSe_2 sample where V_2O_5 has formed on its surface. Additionally, Figure 25 provides optical images of H_2-annealed VSe_2 samples before and after Cl plasma etching, illustrating the impact of the etching process on the material.

Although the analyzed flakes are not identical, the surface texture and oxide layer remain unchanged. Figure 29 presents the Raman spectra recorded before and after 1 minute of chlorine (Cl) plasma etching. The post-etching Raman spectrum exhibits a distinct signature of V_2O_5, with its major peaks closely matching those of the thick flake prior to etching. This observation confirms that the plasma etching process proceeds at a significantly slower rate for vanadium oxide.

Furthermore, by examining Figures 25 and 29, we can better understand the selective nature of Cl plasma etching. These results demonstrate that, when combined with laser treatment, this selectivity can be effectively leveraged to achieve controlled modifications in material composition and structure.

Demonstrating the Selectivity of Chlorine Plasma Etching

To evaluate the selectivity of chlorine (Cl) plasma etching, a VSe_2 flake, shown in Figure 30(a), was subjected to laser treatment to induce the formation of vanadium oxide on its surface. Following this modification, the sample underwent inductively coupled plasma (ICP) Cl etching for 10 seconds. The results indicate that VSe_2 was completely etched, while the vanadium oxide remained intact, demonstrating the selective nature of the process.

Energy dispersive spectroscopy (EDS) analysis at points 2 and 3 confirmed the presence of vanadium and oxygen, with an almost negligible amount of selenium, indicating the formation of a vanadium oxide compound. Additionally, the EDS phase image revealed a high concentration of vanadium in the laser-treated region, further supporting the formation of vanadium oxide. Finally, Raman spectroscopy performed on the same area displayed characteristic peaks of V_2O_5, reinforcing the conclusion that the chlorine plasma etching selectively removes VSe_2 while preserving the oxide.

Selective CF_4 etching

Now we are going to laser treat a sample and selectively plasma etch the

V_2O_5 while keeping the VSe_2 intact. Figure 24 shows a flake that has been treated to with laser and grew an oxide layer as can be seen in the optical image and Raman results that confirms the presence of V_2O_5. And after CF4 ICP etching which shows no V_2O_5 as confirmed by the Raman spectra. Figure 31 (a) presents an optical image of a VSe_2 flake prior to laser treatment, while Figure 31(b) depicts the treated region, with Figure 31 (C and D) displaying the Raman spectrum characteristic of V_2O_5. Additionally, the scanning electron

microscopy (SEM) image confirms the formation of the oxide layer. Figure 32 shows the SEM images of the flake following inductively coupled plasma (ICP) CF_4 etching, where it is evident that the oxide layer has been completely removed while the VSe_2 remains intact. Figure 31 (C & D) presents the Raman spectra recorded before and after plasma etching, where a small A_1g peak at 207 cm^{-1} is observed post-etching. Furthermore, as an additional indicator, SEM images reveal the presence of three small VSe_2 flakes atop the original flake, highlighted by green circles. These features remain visible after etching, confirming that the process selectively removed vanadium oxide (V_2O_5) while largely preserving the underlying VSe_2.

Figure 32 presents the energy dispersive spectroscopy (EDS) data obtained before and after CF_4 plasma etching of V_2O_5. In Table (c), data from points 4 to 8 confirm the presence of a vanadium oxide compound. However, following plasma etching, Table (d) shows that points 1 and 2 exhibit no detectable vanadium, with a significantly high percentage of silicon, indicating that the plasma etching process completely removed the

oxide layer. Point 3, located at the edge, still displays a minimal presence of vanadium oxide, suggesting that some residual material remains at the boundary. The majority of the flake, however, is identified as VS_2. Furthermore, based on Figures 24, 31 and 32, it can be concluded that CF_4 plasma etches both VSe_2 and V_2O_5, with the etching rate being significantly higher for the oxide.

2.5. The results of the Hybrid fabrication method in Magnetic moment study for the thinned flakes

As discussed previously in the literature, VSe_2has a strong magnetic moment at a few layers and it was shown to have an FM behavior at the monolayer. Due

to the flake not being uniform, the etching has produced thin flake. Using a Magnetic tip the sample shows a high magnetic moment for thin flak compared to thick flak. In the Figure (33) the etching effect is shown to be prominent on the edge rather than the center. The Raman spectra show in all three locations there is VSe_2.

The atomic force microscopy (AFM) analysis presented in Figure 36 illustrates the effects of plasma etching on the sample's edge, where distinct layer thicknesses have been measured and annotated with numerical labels and circular markers. This region, spanning a surface distance of 30 nm, exhibits an average thickness of 20 nm, with notable variations in layer height observed at specific locations. These variations, highlighted in the image, suggest a nonuniform thinning process influenced by the specific parameters of the plasma etching procedure. The data further indicate that

the etched profile of the edge is highly dependent on localized effects, which play a critical role in tailoring the material's properties.

In the subsequent figures (37) and (40), magnetic force microscopy (MFM) results will be presented to establish a correlation between these structural modifications and the material’s magnetic moment. This analysis aims to provide deeper insights into how plasma etching influences the magnetic properties at the nanoscale, offering a more comprehensive understanding of the relationship between structural alterations and magnetic behavior.

The magnetic force microscopy (MFM) images presented in Figures 37 and 40 illustrate the spatial distribution of the magnetic moment across the etched edge, where bright regions correspond to areas of high magnetic moment,
while dark regions indicate lower magnetic moments. By correlating the MFM phase image with the three-dimensional (3D)-colored atomic force microscopy (AFM) image, it is observed that regions with a thickness of approximately 14 nm exhibit the highest brightness, signifying a peak in the magnetic moment. The 3D-colored AFM image proves particularly valuable in visualizing height and thickness variations within the flake, providing critical insight into the structural features that influence its magnetic properties. This strong correlation between thickness and magnetic moment underscores the pivotal role of controlled etching in modulating the material's magnetic behavior, as
evidenced by the precise alignment between the MFM and AFM data at specific locations.

In the subsequent figures (38 to 40), a second sample is analyzed, further corroborating the observation that plasma etching generates regions with reduced layer thickness, thereby enhancing the magnetic moment. The AFM image of this sample reveals variations in thickness along one of its edges, while the corresponding MFM phase image displays bright regions where the magnetic moment is maximized. These findings reinforce the conclusion that a reduction in layer thickness, facilitated by plasma etching, directly enhances the material's magnetic properties, as demonstrated by the consistent correlation between the AFM and MFM data.

To gain a deeper understanding of the relationship between thickness and magnetic moment, we will develop a quantitative model that describes this correlation. By integrating experimental data from atomic force microscopy (AFM) and magnetic force microscopy (MFM) measurements, the model will

capture the observed trend across different samples, wherein thinner regions consistently exhibit enhanced magnetic moments. This model will account for key factors such as the effect of layer thickness on magnetic interactions and potential modifications induced by plasma etching. Establishing this relationship will provide valuable insights into the underlying mechanisms governing the observed magnetic behavior, facilitating predictive control over the material's properties for future applications.

2.6. Theoretical Correlation Between Selenium Vacancies and the Increase in Magnetic Moment

To investigate the relationship between selenium (Se) vacancies and the enhancement of the magnetic moment, we conducted a density functional

theory (DFT) simulation on VSe_2, examining the correlation between Se vacancies and strain. In our calculations, a Se vacancy was introduced into a 2×2 lattice, resulting in both an increase in the magnetic moment and an associated rise in strain. Subsequently, we applied tensile strain to the system and observed a further enhancement of the magnetic moment. These findings suggest that the presence of Se vacancies induces strain, which in turn contributes to the increase in the magnetic moment. Figure 39 presents the results of this study.

Formal Electron Count vs. Actual Degeneracy

In many textbooks or simplistic ionic models, vanadium in VSe_2 is treated as V^{4+} with a nominal $3d^1$ configuration, suggesting there is just a single d-electron. However, even a single electron in a degenerate or nearly degenerate orbital manifold can drive a Jahn–Teller (JT) distortion. According to the JT theorem, any nonlinear molecule or crystal site with a degenerate electronic

ground state can lower its total energy by distorting and thereby splitting the degeneracy. In the case of a doubly or triply degenerate set of orbitals, shifting one orbital downward in energy and another upward lets that single electron occupy the lower-energy orbital, producing a net energy saving. Thus, simply having “one d-electron” does not preclude a JT distortion; if there is an orbital degeneracy, even one electron can take advantage of it.

How a JT Distortion Affects VSe_2

In monolayer VSe_2, the V 3d states near the Fermi level can be partially

occupied and near-degenerate due to the trigonal prismatic or octahedral-like crystal field environment. A Jahn–Teller distortion lifts this degeneracy: before the distortion, two or more d-orbitals may lie close in energy; after the distortion, these orbitals split, allowing the partially filled d-band (or the single d-electron) to preferentially occupy the newly lowered orbital. This arrangement lowers the electronic energy by an amount ΔE that can outweigh the elastic cost of the distortion, especially if the electron–phonon coupling is strong. In addition, altering the orbital occupancy and splitting often enhances local magnetic moments. In VSe_2, experiments and calculations show that doping, vacancies, or strain can reinforce this effect, leading to an increase in the magnetic moment.

Why One Electron Is Sufficient for a JT Distortion

A common misconception is that multiple electrons must occupy degenerate orbitals to realize a significant JT effect. In reality, even a single electron in an orbital doublet (denoted e) or triplet (t_2) can benefit once that level is split.

Placing the electron in the lower sub-level reduces the total electronic energy. Mathematically, in a simple two-level degenerate system with energy E_0, a small distortion that lowers one level by δ while raising the other by δ gains δ in electronic energy for the electron occupying the lower level. If the lattice cost scales roughly like $(½)KQ^2 \sim \delta^2$, then for a sufficiently strong electron– phonon coupling, the overall energy will still decrease, driving the distortion**. Connecting to VSe_2 in Practice**

From a computational perspective, first-principles calculations (e.g., using

DFT) often reveal that certain d-orbitals in monolayer VSe_2 lie near the Fermi energy, partially filled and close to degeneracy. Small structural deformations—or effects such as Coulomb interactions, strain, or Se vacancies—can lift this degeneracy, effectively channeling the electron(s) into the newly stabilized orbital(s).

Experimentally, some observe a charge density wave or structural distortion that can be explained by Fermi surface nesting but may also be understood through a Jahn– Teller lens: the system lowers its symmetry to gain electronic energy. When Se vacancies are introduced, local crystal fields, doping levels, and electron–phonon interactions all shift in ways that can strengthen the JTtype distortion. This reorganization of electronic states and possible orbital polarizations ties directly to changes in the magnetic moment, as a more localized or favorably occupied dorbital can support a larger spin polarization. Despite the nominal single-electron (d1) configuration of V in VSe_2, the
V 3d bands can retain partial degeneracy and therefore remain susceptible to a Jahn– Teller distortion. The fundamental mechanism is straightforward: a slight distortion lifts degeneracies, placing the electron in the lower- energy orbital and reducing electronic energy. Whether or not this distortion materializes depends on the balance of electron–phonon coupling strength and the elastic energy cost. Once it does occur, it often enhances magnetism by favoring a more robust spin polarization. Thus, monolayer VSe_2 provides a compelling example where even “one delectron” can drive Jahn–Teller physics, consistent with the observed increases in magnetic

moment under conditions that reinforce or stabilize the underlying distortion, such as additional Se vacancies or applied strain.

Figures 41, 42, 43 and 45 present the simulation results of a simplified toy model designed to correlate selenium (Se) vacancies with the magnetic moment through Jahn-Teller (JT) distortion. Figure 42 illustrates the gradual increase in the magnetic moment as the vacancy concentration rises, reaching an approximately constant value at around 10% vacancy. This increase in the magnetic moment is nearly twofold. Figure 43 depicts the variation in the density of states (DOS) as a function of Se vacancy concentration. As the number of Se vacancies increases, the density of spin-up states near the Fermi level also increases, which accounts for the observed enhancement in the magnetic moment.

DFT Calculation on VSe_2 Investigating Magnetization vs Strain This study examines how an isotropic lateral contraction affects the magnetization properties of VSe_2 using DFT calculations. The DFT computations were performed with the Quantum ESPRESSO package [82]. We employed the Perdew– Burke–Ernzerhof (PBE) exchange-correlation functional within the GGA framework [83] and used norm-conserving pseudopotentials to model the electronic interactions [84]. The electronic self- consistent field loop was converged to an energy tolerance of 1×10^(-8) Ry, and atomic positions were relaxed until forces dropped below 1×10^(-3) Ry/bohr. To ensure converged magnetization results, a 12×12×1 k-point grid was used, and the plane- wave cutoff energies were set to 700 Ry for the wavefunctions and 60 Ry for the charge density.

Figure 45 present the atomic structure of a vanadium selenide (VSe_2) material under varying strain conditions. Panel (a) illustrates the crystal structure of VSe_2, where vanadium (V) atoms are shown in purple and selenium (Se) atoms in gold, with the lattice constant a_0 indicated. Panel (b) depicts the VSe_2 structure under zero strain, with the separation between the atoms represented by the lattice constant $a_0 = 0.334$ nm. Panel (c) shows the structure under a -4% strain, where the lattice is compressed, causing the interatomic distances along the lattice to decrease. Finally, panel (d) illustrates the structure under a +4% strain, where the lattice is stretched, resulting in increased interatomic distances. The arrows indicate the direction of strain applied to the structure in panels (c) and (d). These images highlight how the atomic arrangement of VSe_2 is altered with the application of tensile and compressive strain.

The density of states (DOS) and projected density of states (PDOS) results presented in Figure 47 illustrate the effect of strain on the electronic and magnetic properties of the system. The total DOS (Figure 47(a)) shows a systematic decrease in the magnetic moment as strain increases from -0.1 to

0.1. This behavior indicates that strain directly influences the spin polarization of the system, leading to a reduction in the net magnetization. The linear dependence of magnetization on strain can be attributed to the strain-induced modification of the electronic structure, which alters the exchange interactions governing the spin splitting of electronic states.

To understand the microscopic origin of this trend, we examine the

PDOS for the d-orbitals of vanadium (Figure 47(b)), which represent the largest contribution to the total DOS. The results reveal that the spin polarization of the vanadium d-orbitals follows the same trend as the total moment, decreasing as strain increases. This suggests that the observed magnetization change is primarily driven by the redistribution of states near the Fermi level, where the d-orbitals play a dominant role. Under in plan tinsel strain (-0.1), the spin-up and spin-down states exhibit a larger splitting, leading to a higher magnetic moment. As the strain decreases, this splitting diminishes, reducing the exchange interaction strength and consequently decreasing the total magnetization.

The results obtained from the DFT calculations were analyzed to determine the relationship between isotropic lateral strain and the magnetization of VSe_2. A detailed analysis of the magnetic moments, and density of states was conducted to understand the underlying mechanisms. This methodology provides a comprehensive framework for investigating the magnetization properties of VSe_2 under isotropic lateral strain using DFT calculations. The results contribute to a deeper understanding of the strain dependent magnetic behavior of VSe_2 and potentially guide future experimental and theoretical studies in this field. These findings highlight the crucial role of strain engineering in tuning the magnetic properties of the material. By controlling the strain state, it is possible to modulate the electronic structure and, consequently, the magnetic response, which is essential for potential applications in strain-controlled spintronic devices.

2.7 Figures

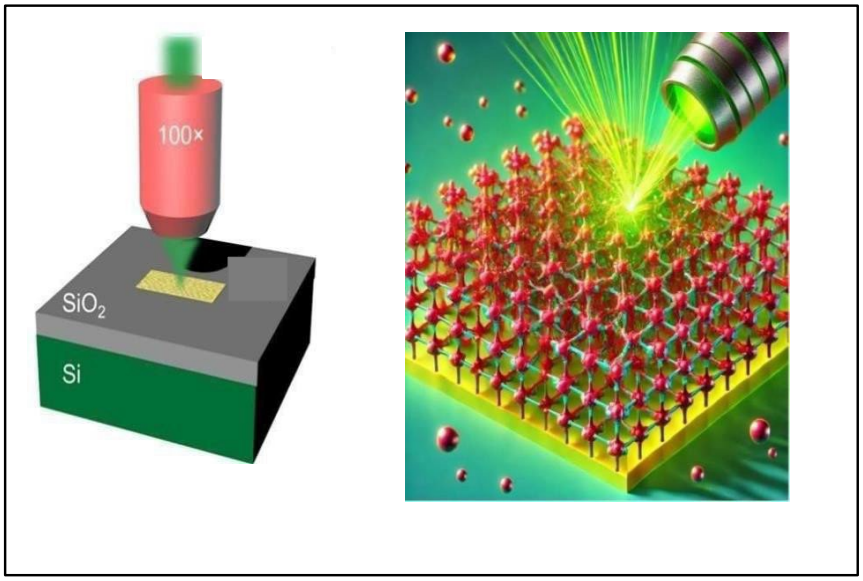


Figure 4: The Laser Treatment apparatuses. Using the laser in situ with the Raman spectroscopy setup.

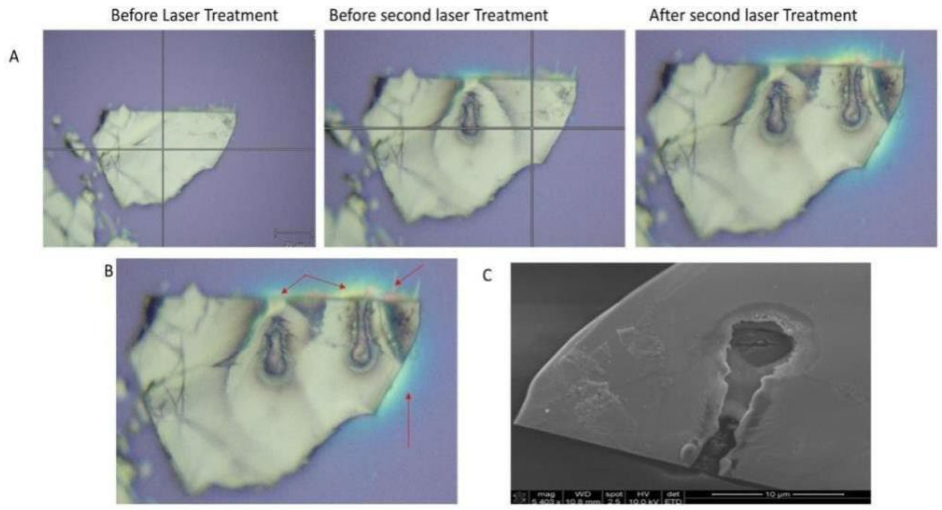


Figure 5: Effects of high power laser treatments on the VSe_2 flake. (A) shows the before and after images. (B) shows the effects after 100mW power, 785nm laser for 1min. Red arrow show light green coloring from the SeOx due to laser treatment. (C) SEM image detailing the effect of the laser treatment.

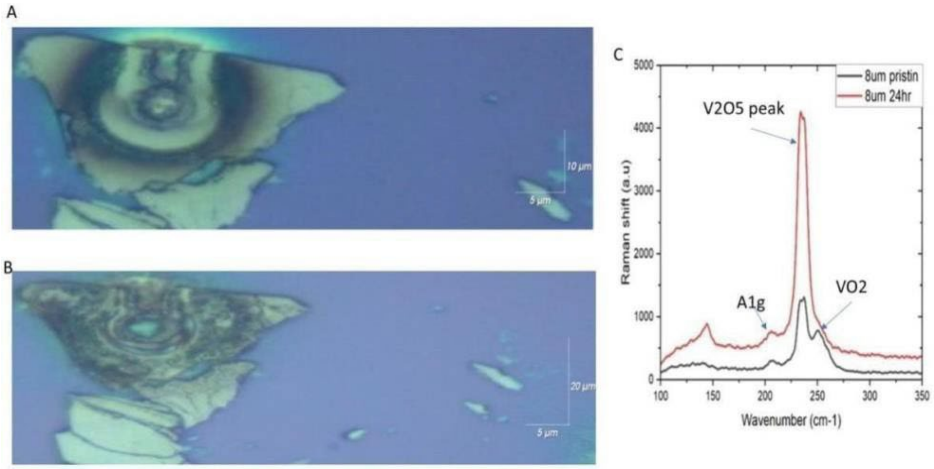


Figure 6: A & B show the effect of 100mW laser treatment for 5 min: A after the treatment and B 24 hours later. C shows the Raman spectra. Black is the pristine measurement and red is 24 hours later. On a spot 8um away from the treatment location. It shows the disappearance of VO_2 peak.

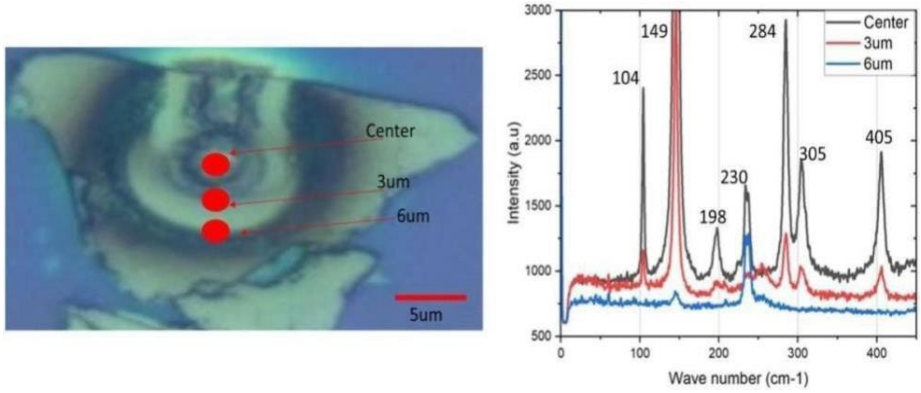


Figure 7: Flake single laser treatment of 100mW, 785nm, five minutes. Raman spectra show three locations: black spectra (center of laser treatment), red 3um away from laser treatment spot, blue 6um from laser treatment spot. The blue curve is small to show any feature only the strong oxide at 230-1. Both black and red show a combination of vanadium oxide peaks. Peaks of 305 and 405 cm-1. Check the Raman shift table in the appendix.

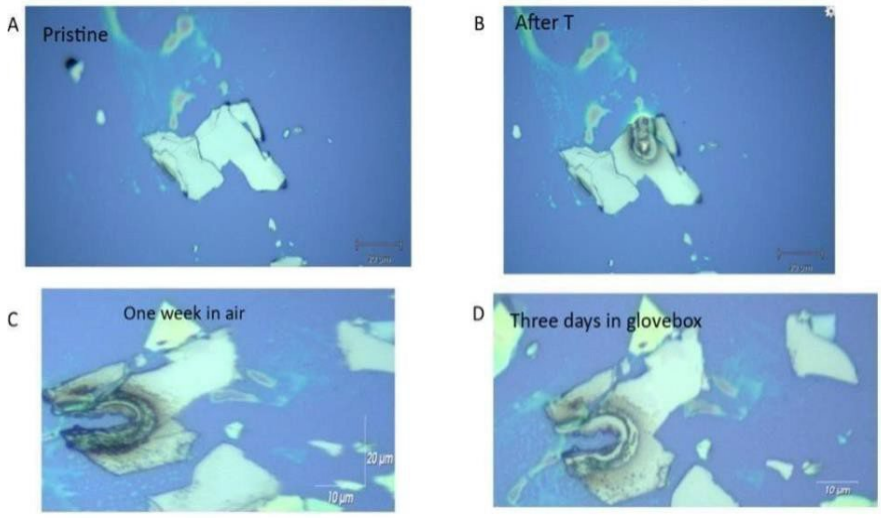


Figure 8 A) showing the pristine flake. B) flake after laser treatment of 100mW using 785nm laser. C) leaving one week in ambient condition. D) after three days in the glovebox.

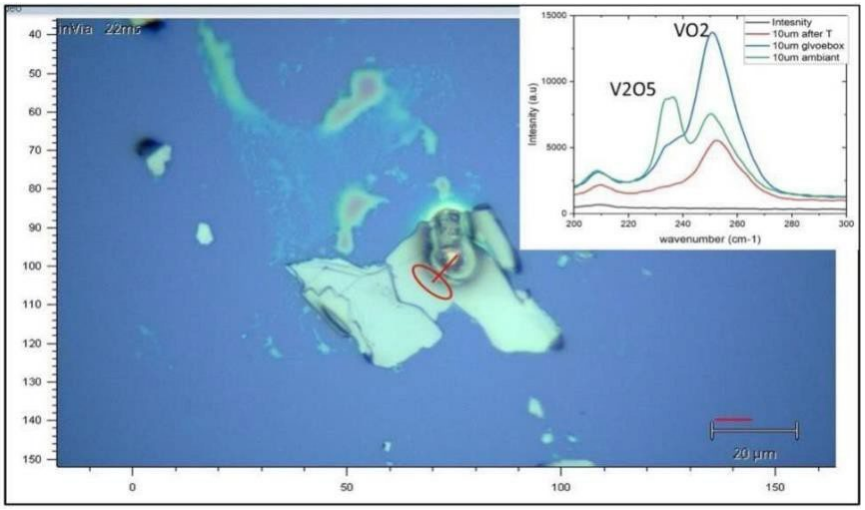


Figure 9 Shows a flake that was left after treatment (100mW for 5 min.). The Insite show Raman spectra, the development of the V2O5 peak. The Raman spectra was taken 10 um away in the red zoon shown in the optical image. Three Raman measurements were taken, black before laser treatment, red after treatment, blue after one week in glove box, green three days in Ambient conditions. These measurements were taken one after the other, respectfully.

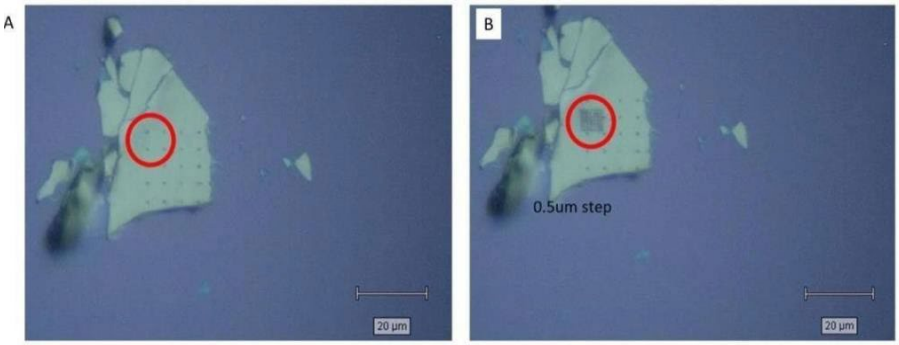


Figure 10: A) before laser mapping treatment. B) after laser mapping treatment.

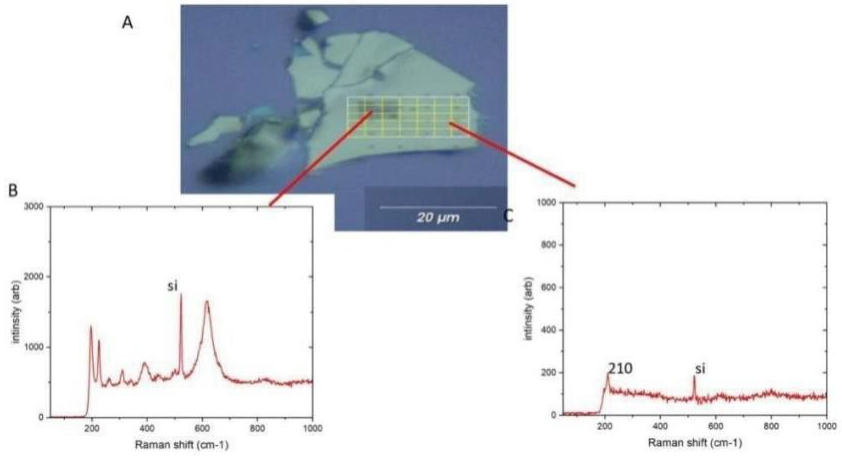


Figure 11 A) optical image showing treatment and Raman map. B) Raman spectra of oxide area. C) Raman spectra showing no treatment.

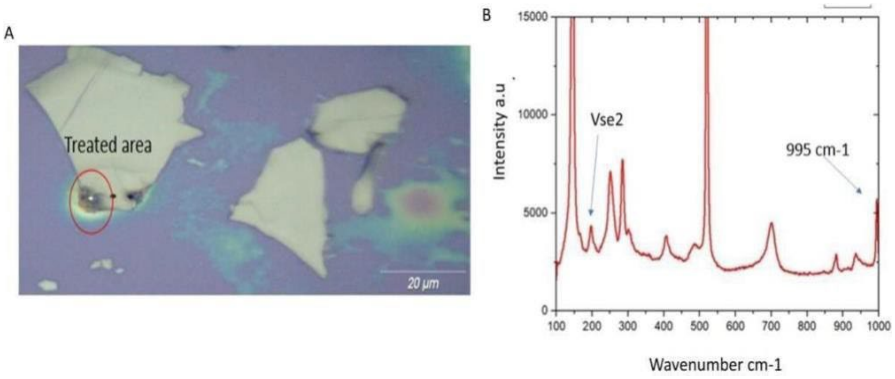
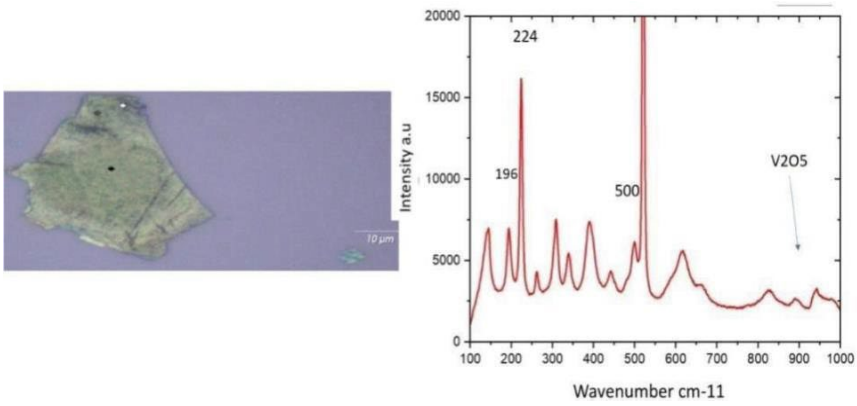


Figure 12: A) optical image showing treated location. B) Raman spectra of treated area, showing spectra V2O5 peak at 995cm-1



.

Figure 13: A) optical image showing annealed sample. B) Raman spectra of annealed area, showing spectra V2O5 peak at 995cm-1.

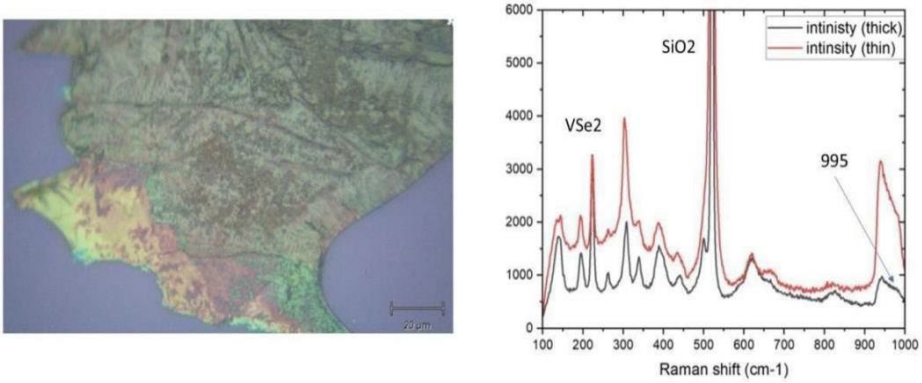


Figure 14: A) optical image showing annealed sample. B) Raman spectra of annealed area, showing spectra peak at 995cm-1.

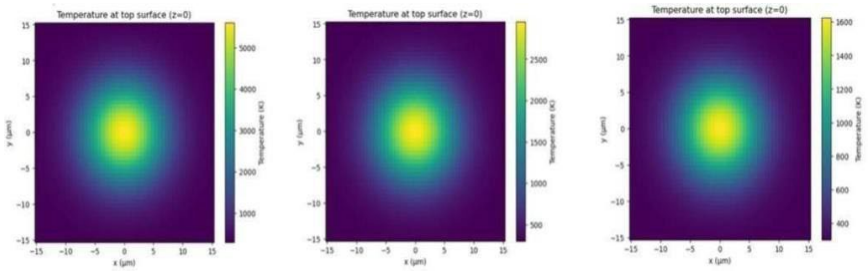


Figure 15: Simulation results for laser treatment on the surface of VSe_2 of varying thickness. Assuming no heat exchange with the surrounding except the SiO2 substrate. SiO2 substrate was kept at 300nm.

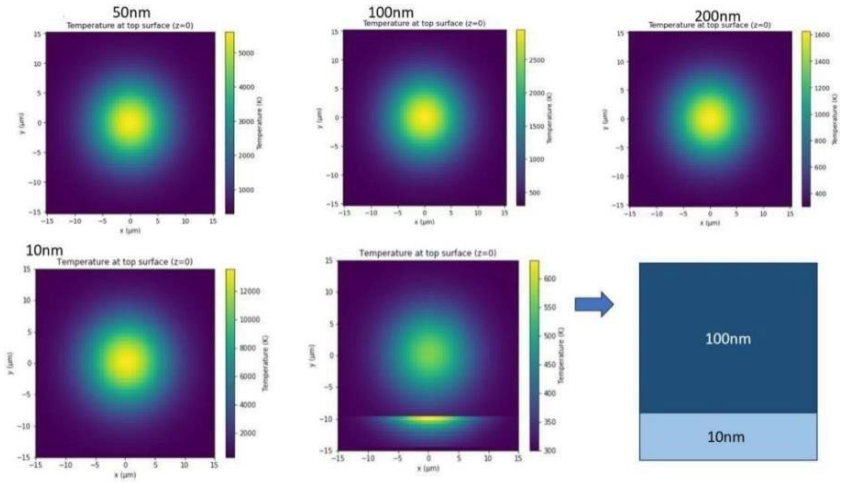


Figure 16: Simulation results for laser treatment on the surface of VSe_2 of varying thickness. Assuming no heat exchange with the surrounding except the SiO2 substrate. SiO2 substrate was kept at 300nm.



Figure 17: Shows the growth of the oxide starting from the edge. Going from A to C, the growth evolves from the edge. The treatment location is pushed down as seen in C by the red box. Mapping parameters 50mW for 0.1s.

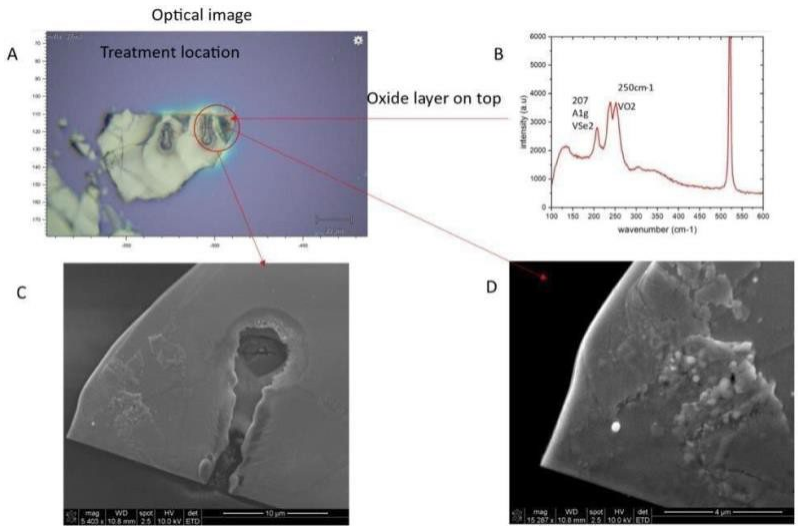
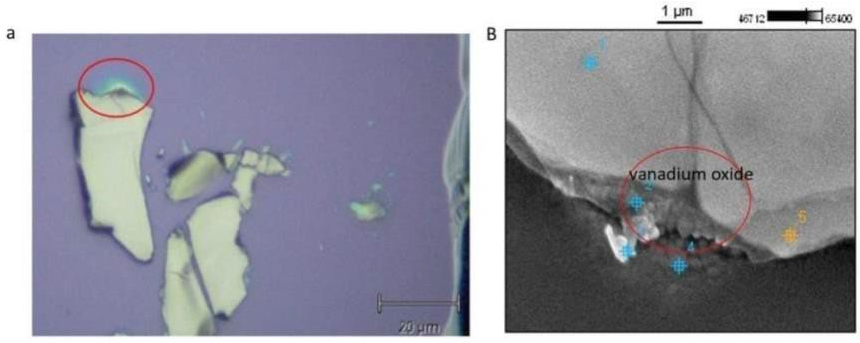


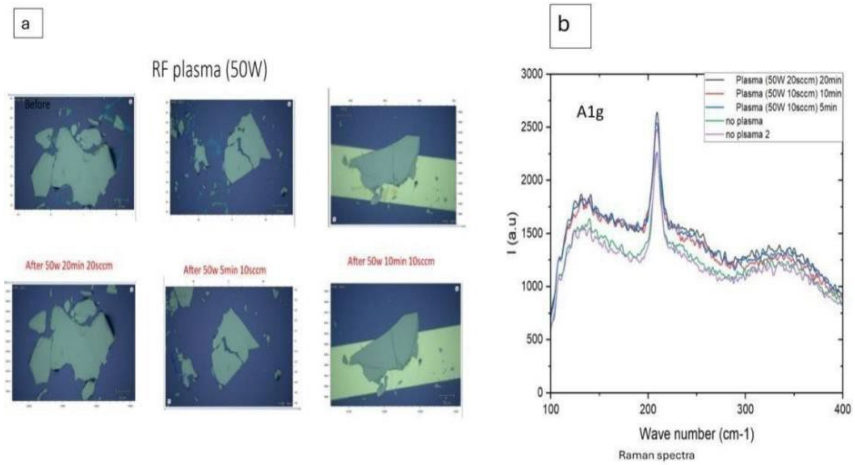
Figure 18: A treated sample heat effect on the thin edge, with Raman spectra showing oxide peak of 250cm-1. A) optical image of the treated area. B Raman spectra of edge showing oxide peak. C&D SEM images of the effect of laser.



C **EDS results: % compound**

	C	O	Si	V	Ge	Se
Mnr det shift test(3)_pt1	9.54	3.24	45.23	13.68	0.00	28.32
Mnr det shift test(3)_pt2	18.53	14.66	50.25	13.30		3.27
Mnr det shift test(3)_pt3	19.50	16.03	52.15	6.45		5.88
Mnr det shift test(3)_pt4	11.14	16.72	65.05	0.53		6.56
Mnr det shift test(3)_pt5	8.73	8.96	54.74	9.40		18.17

Figure 19: A) optical image of laser mapping treatment on the edge. B) SEM image of the laser mapped edge. C) EDS results for the % compound on the points in B.



20: A) showing RF plasma effect before and after. Top images show the before, bottom images show the after. B) Show the Raman spectra. All spectra show no change.

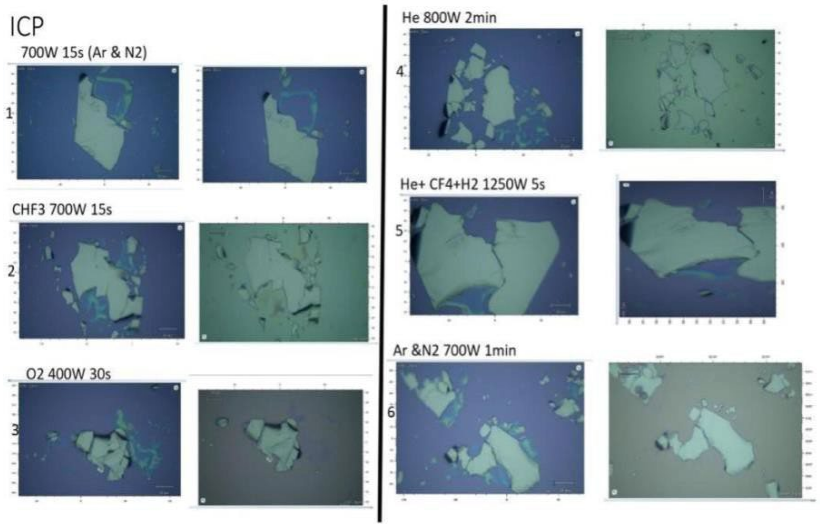


Figure 21: Shows a set of ICP plasma treatments, indicating no change. Left, before treatment; right, after treatment.

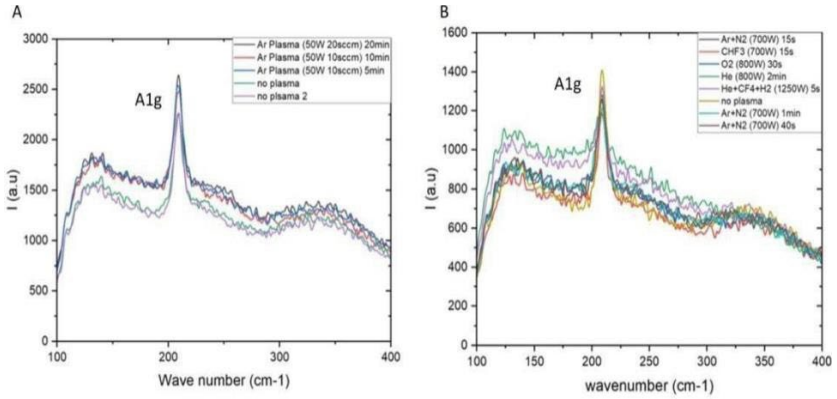


Figure 22: A) shows the Raman spectra of after RF plasma treatment. B) shows the Raman spectra after

I

CP plasma treatment.

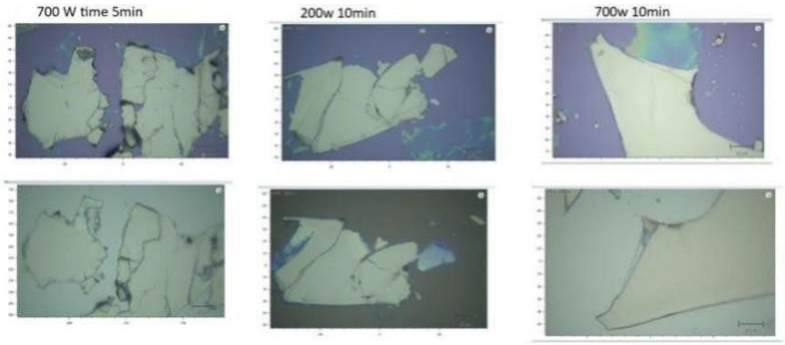


Figure 23: All figures showing the effects of etching when using CF4 for high powers and longer time.

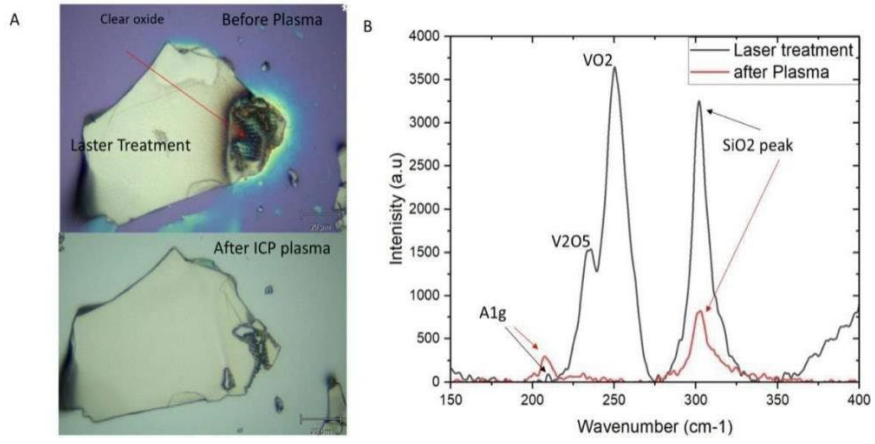


Figure 24: A) optical image after laser treatment and before ICP plasma treatment. B) after plasma treatment. C) Raman spectra (black spectra before ICP treatment, red after plasma treatment). Spectra (black before ICP plasma, red after plasma).

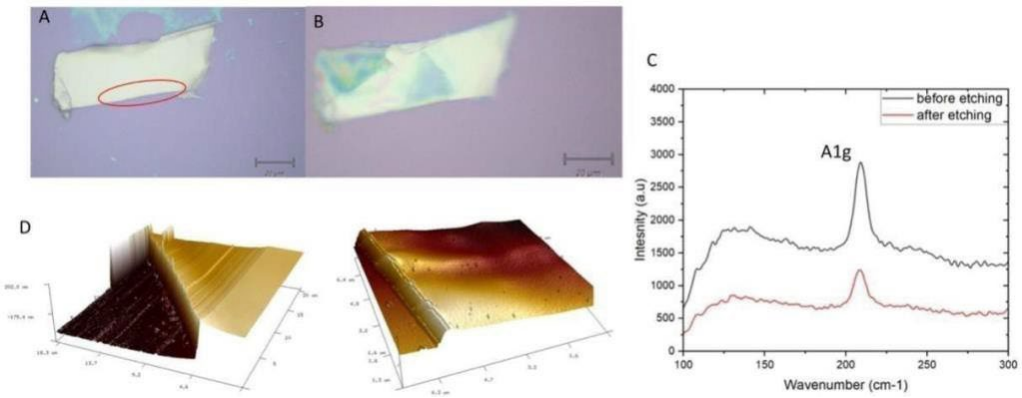


Figure 25: A) and B) are optical images of before and after CL ICP etching. C) Raman spectra of before (black) after (red). D) 3D AFM.

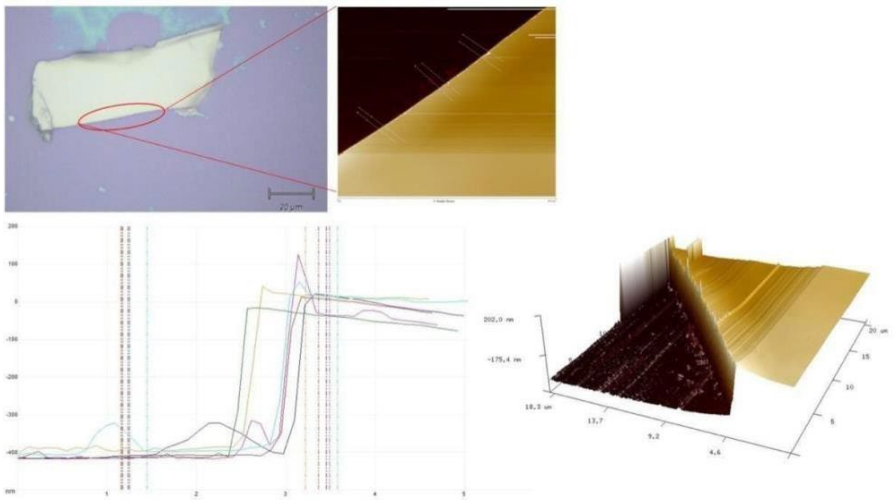


Figure 26: Showing the AFM results thickness before the ICP CL etching.

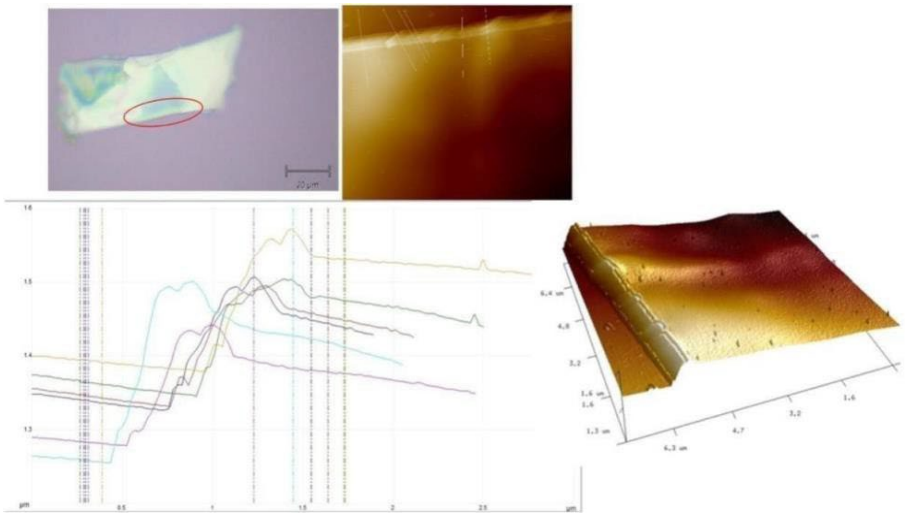


Figure 27: AFM after ICP CI-etching, showing a decrease in thickness of 300nm. The red circles are where the measurements are.

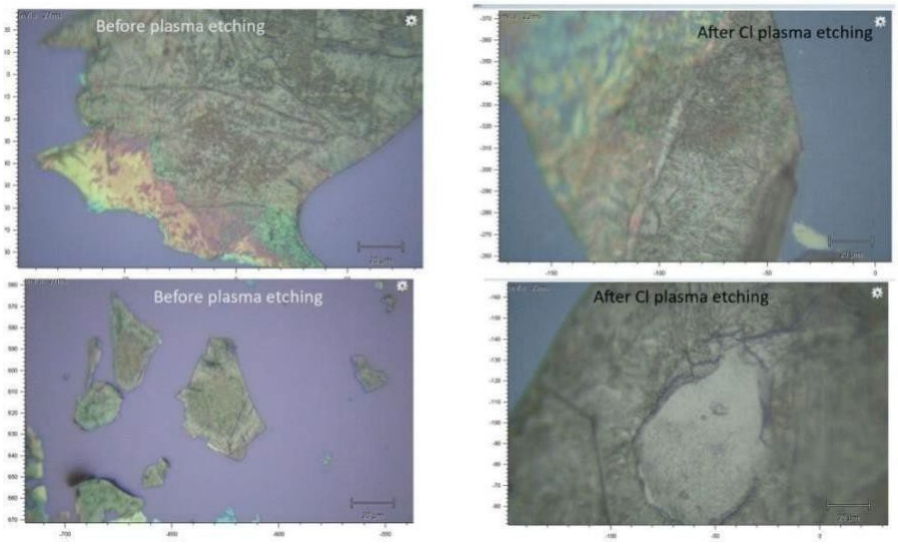


Figure 28: Showing the V2O5 grown via annealing before and after ICP CI plasma etching. Etching for 1 minute up to 3 minutes.

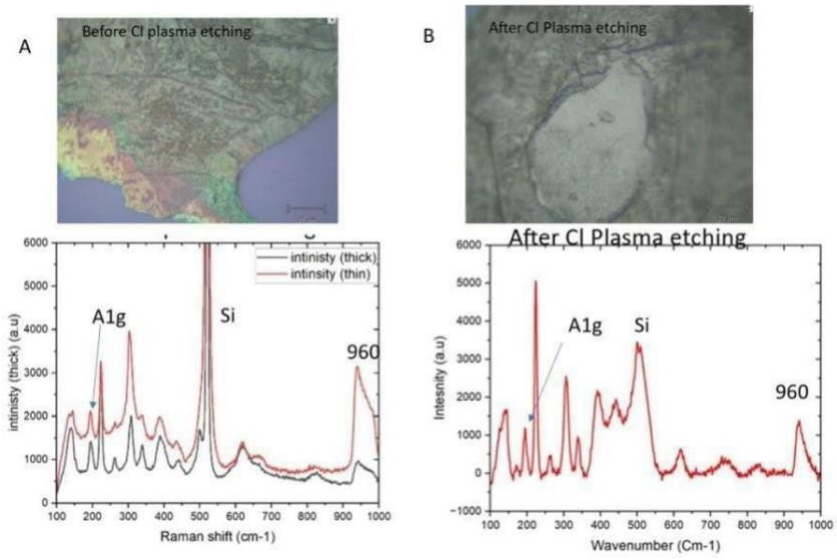


Figure 29: A) and B) show the optical image of flakes before and after the CL plasma treatment (not the same flake). C) and D) show the Raman spectra for both, with a clear peak at 960 and 990 that is of V2O5 but the A1g peak can be seen indicating the presence of the VSe_2 underneath.

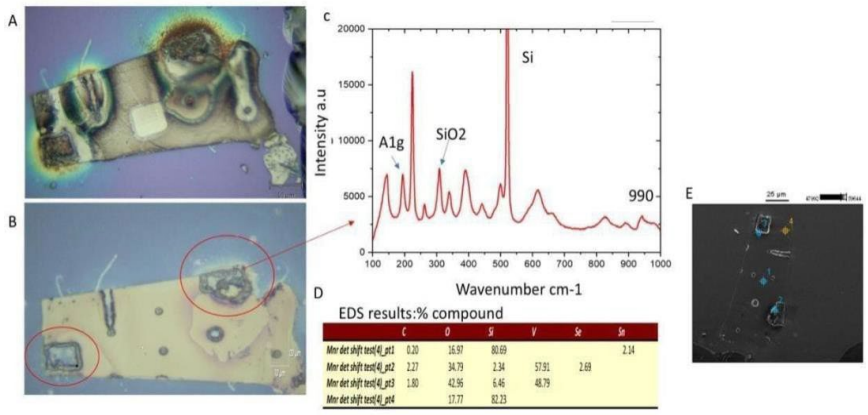


Figure 30: Selective etching for VSe_2 and preserving V2O5. A) and B) before and after etching; red circle shows V2O5 after ICP CL etching. C) Raman spectroscopy for V2O5.
E) SEM image. D) EDS results.

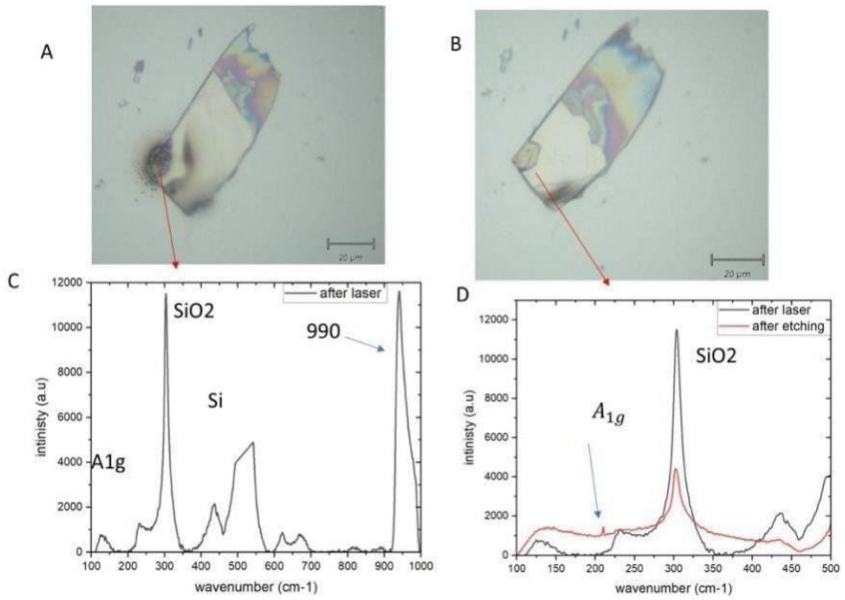


Figure 31: Selective etching of V2O5. A) and B) illustrate an optical image before and after etching (red circle treated V2O5).C) and D) illustrate Raman Spectra: C) V2O5 Raman spectra. D) Raman spectra after ICP CF4 etching.

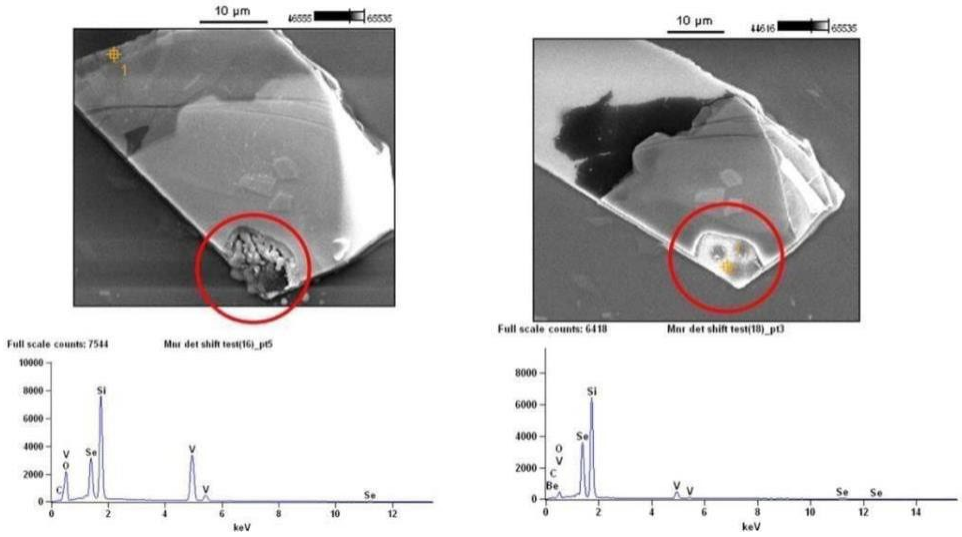


Figure 32: EDS results before and after ICP CF4 plasma treatment. EDS data were taken on the red circle area.

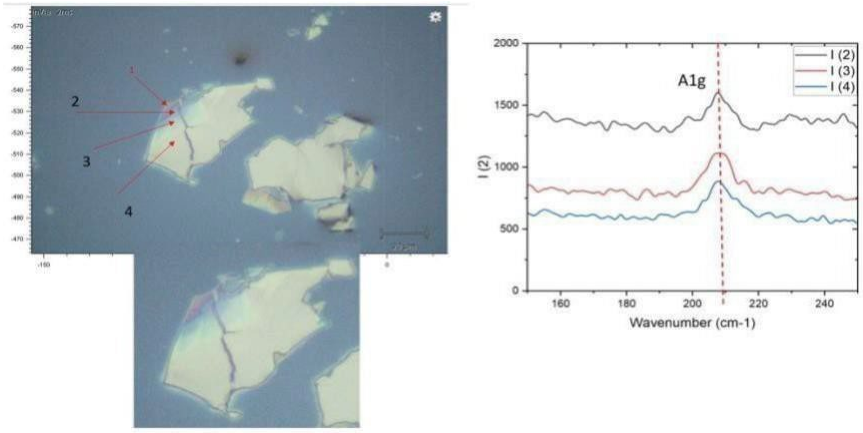


Figure 33: ICP etching results. Raman spectra only showing A1g. No oxide peak detected and no shift for the A1g.

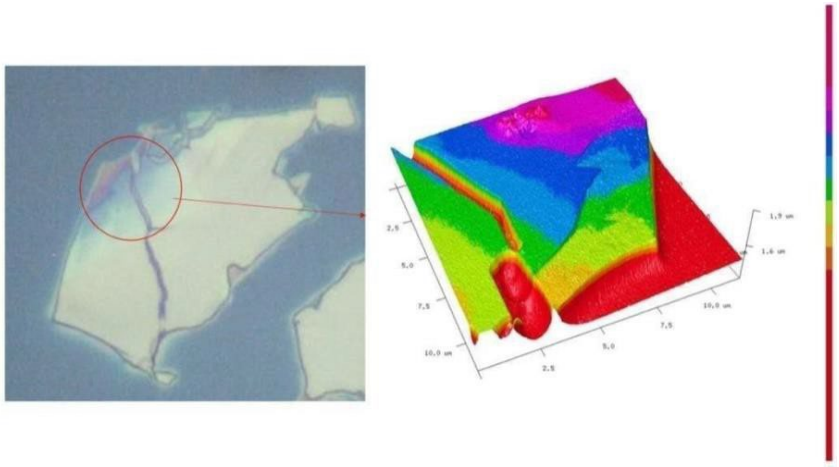


Figure 34: 3D AFM results after ICP CH4.

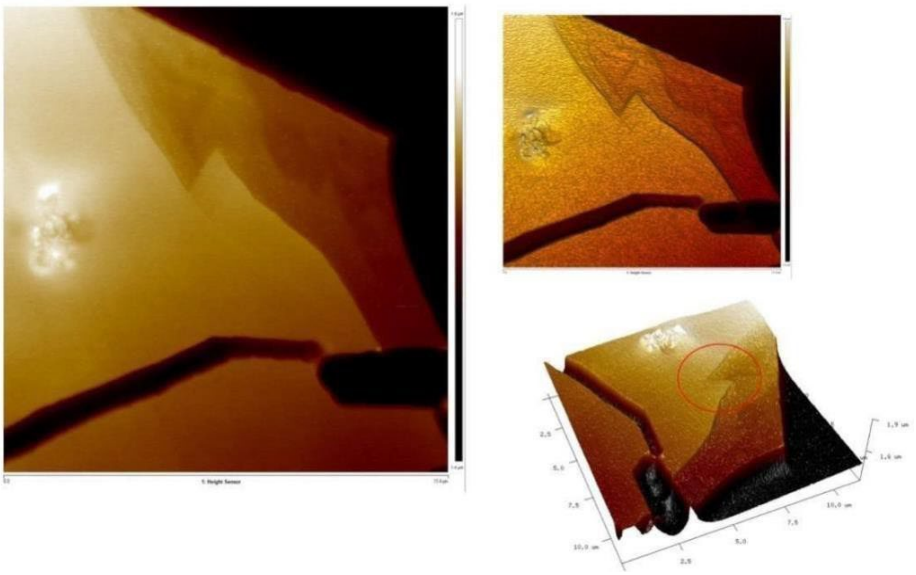


Figure 35: AFM images. C) 3D AFRM image (circle image).

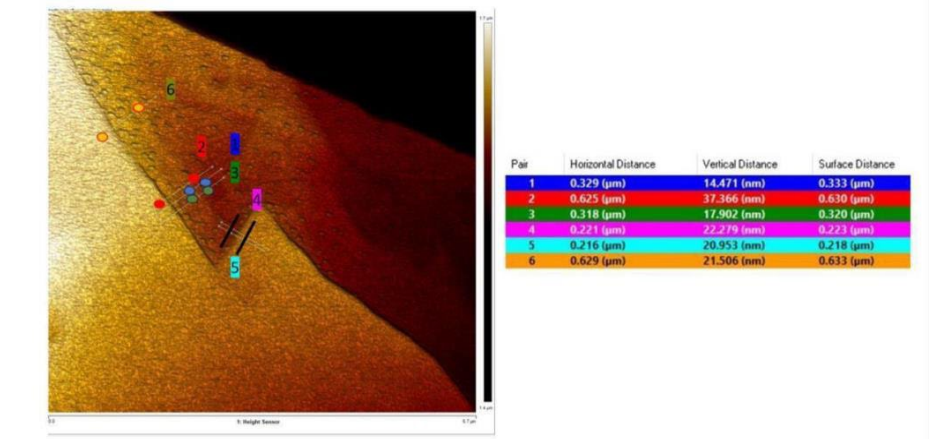


Figure 36: ARM image. B) values are adjusted to the nearest three digit, which is not real value (software adjusted values).

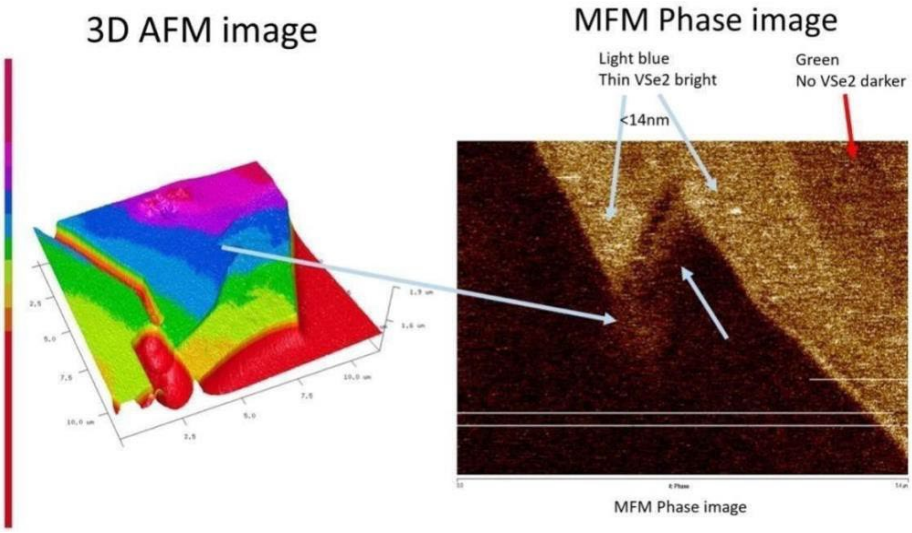


Figure 37: 3D AFM. B) MFM phase image that shows magnetic moment.

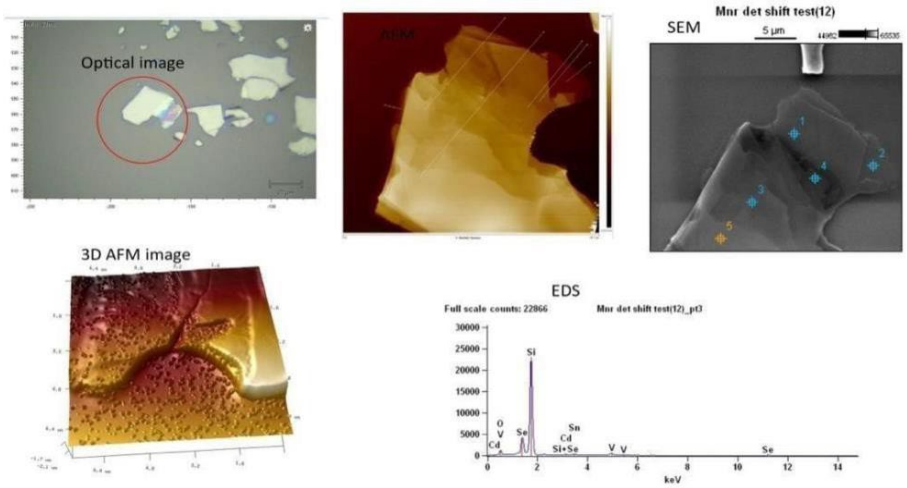


Figure 38: CF4 ICP plasma etched flake.

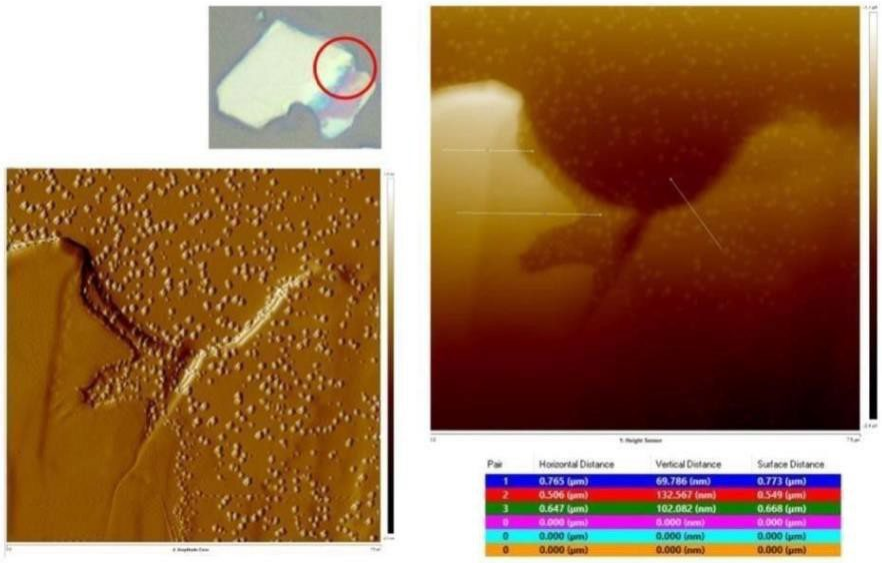


Figure 39: AFM image after ICP CF4 etching.

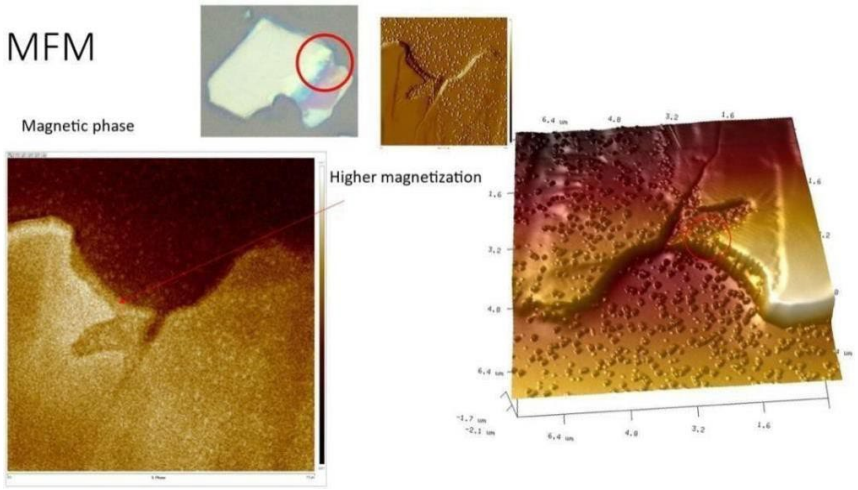


Figure 40: A) optical image. B) 3D AFM image. C) MFM image.

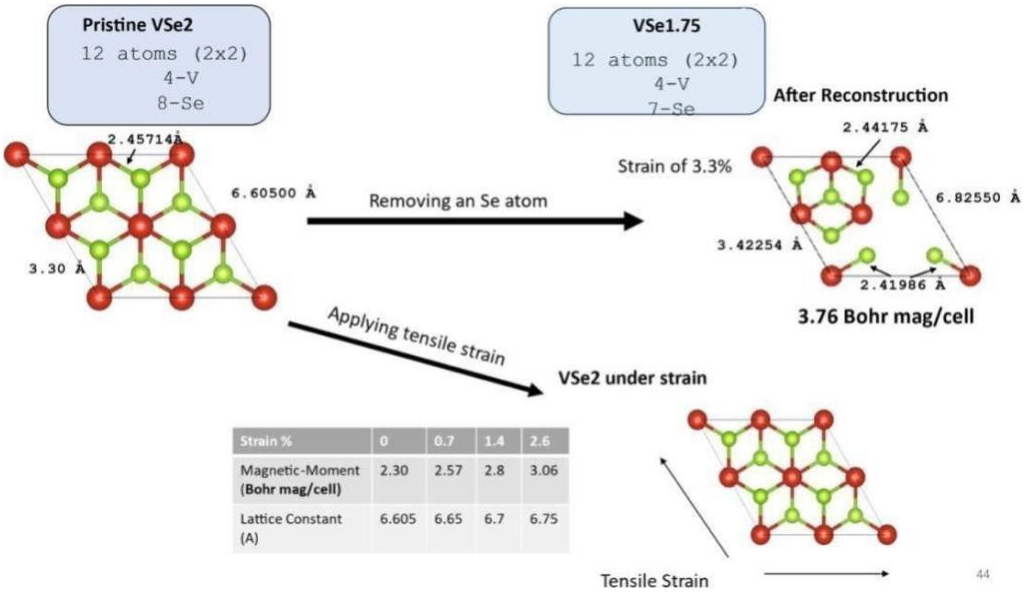


Figure 41: DFT simulation. Removing Se single atom and observing the increase of magnetic moment as well as an increase in local strain.

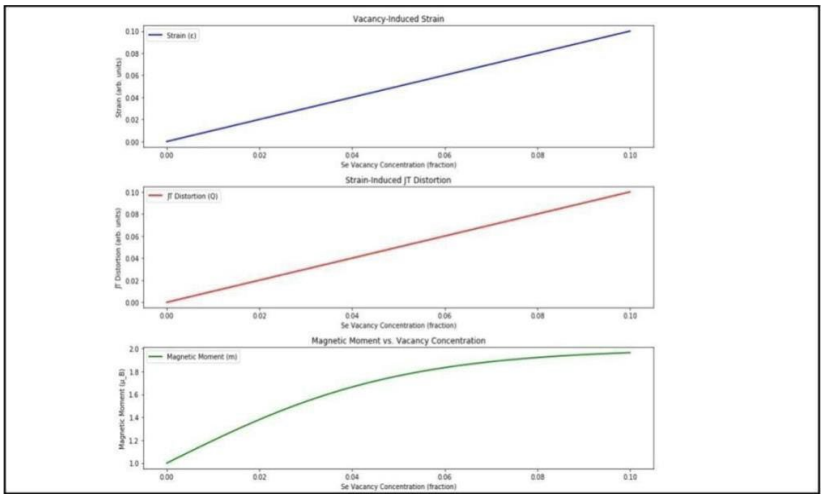


Figure 42: A) using DFT simulation correlate Se vacancy with strain. B) DFT simulation correlating Se vacancy Jhan- Teller distortion. C) DFT simulation and correlation of Se vacancy with the magnetic moment.

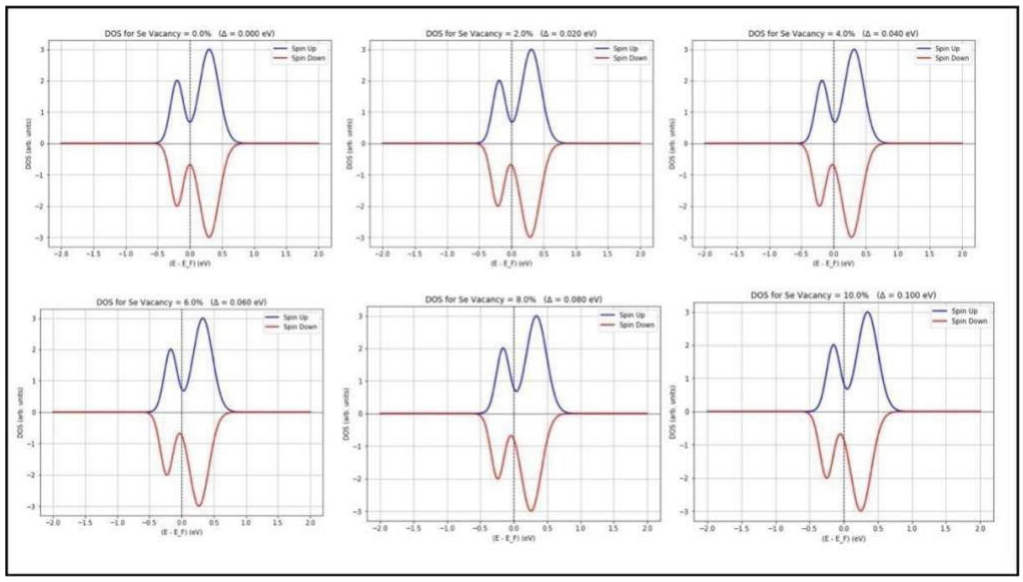


Figure 43: Dos of VSe_2 each figure represents a % Se vacancy. Starting from 0% Se vacancy.

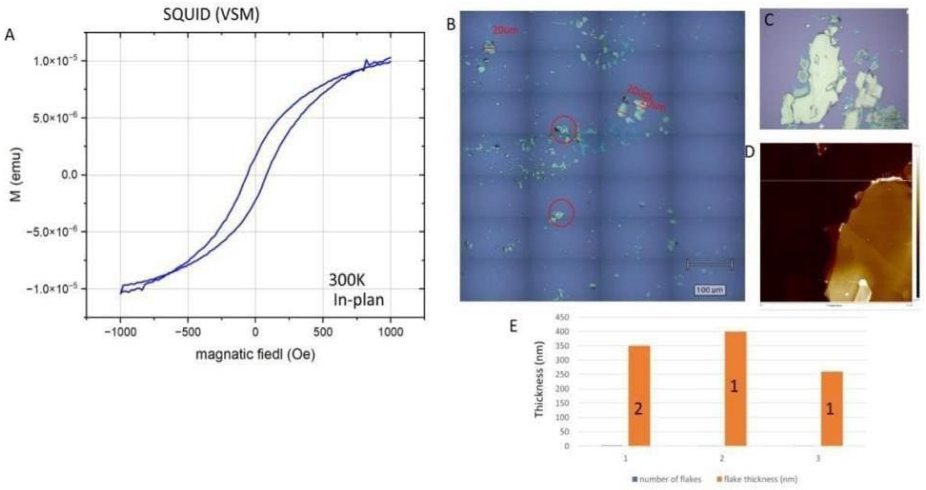


Figure 44: A) SQUID results VSe_2 CVD grown and exfoliated on SiO2 (300nm) for in- plan external magnetic. B) optical image of the VSe_2 flake. C) and D) optical and AFM results of a flake. E) statistic of an example of flakes with various thickness.

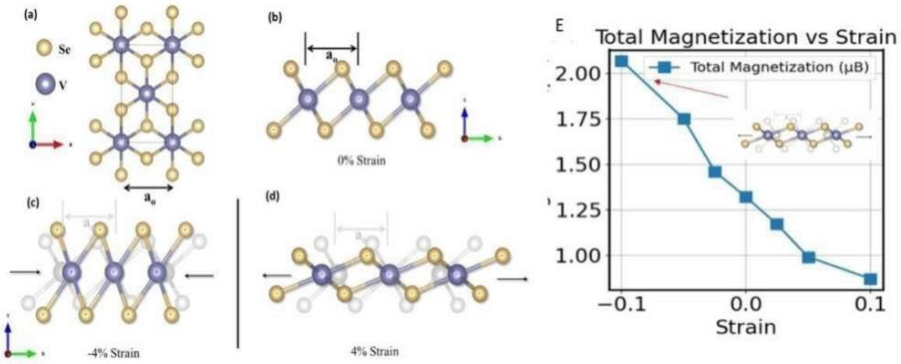


Figure 45: DFT simulation for the correlating strain with magnetic moment. E) the outer plan strain vs. magnetic moment.

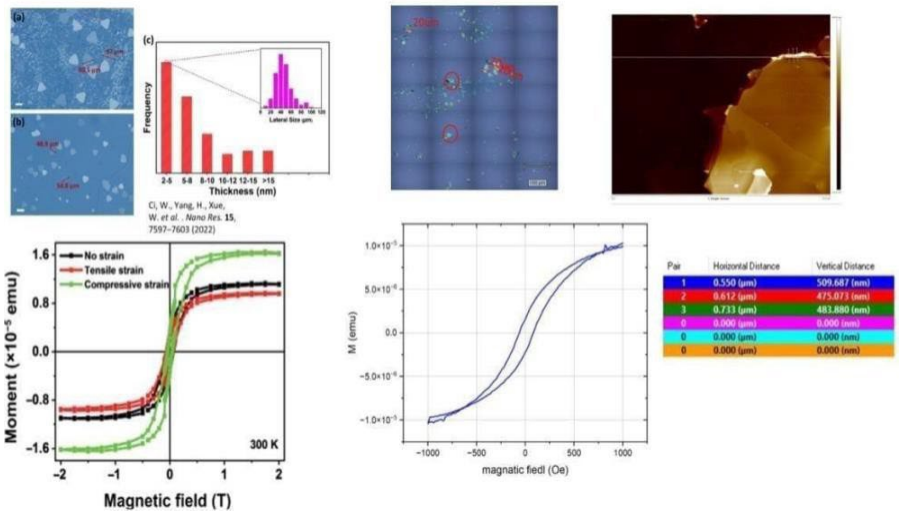


Figure 46: A) and B) are published results from Ci, et al. 2022, showing SQUID results and thickness of flakes. Comparing This works SQUID result, of in plan at room temperature.

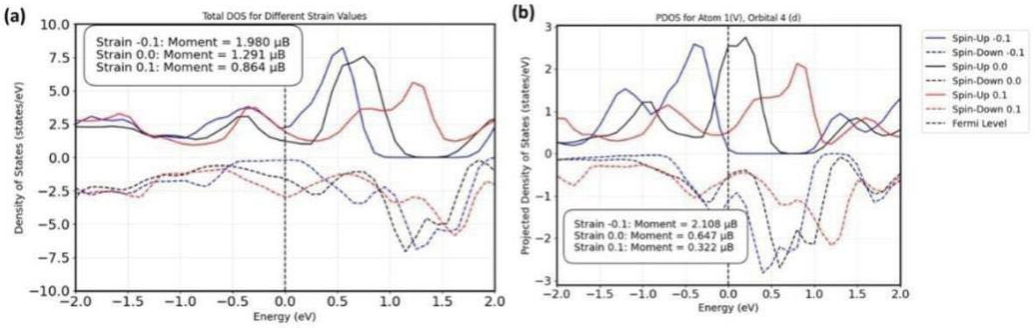


Figure 47: Density of states (DOS) of VSe_2 under different strain conditions. **(a)** the total DOS for three different strain values (-0.1, 0.0, and 0.1). The spin-up and spin-down contributions are depicted with solid and dashed lines, respectively. **(b)** presents the projected density of states (PDOS) for the d-orbital (orbital 3 of Vanadium (V). 3.

3. Results analysis and discussion

3.1 Overview

This chapter describes the experimental procedures for laser treatment and plasma etching of vanadium diselenide (VSe2) flakes. The goal is to achieve localized oxidation, evaporation, or thinning of the material by combining a confocal Raman based laser setup with selective plasma etching. Various characterization methods are introduced to evaluate structural, magnetic, and compositional properties of the treated samples. Specific process parameters, such as laser power ranges, plasma gas flow rates, and instrument calibration details, are deferred to the comprehensive methodology section to maintain clarity.

3.2 Laser Treatment System

The laser processing stage is centered on a confocal Raman spectroscopy instrument equipped with a 785 nm laser source and a 50´ objective lens, producing a spot size of approximately 1 μm on the sample surface. Exfoliated VSe_2 flakes were mounted on a 300 nm SiO_2/Si wafer, allowing localized oxidation or evaporation by varying the laser power, dwell time, and scanning step size.

One significant advantage of this setup is its *in situ* measurement capability: the Raman spectrometer collects back-scattered light immediately from the same region undergoing laser treatment, enabling real-time monitoring of phase changes, surface oxidation, or thickness alterations. A schematic (Figure 48) illustrates how the laser beam is focused onto the VSe_2

surface through the objective lens, while a beam splitter and optical filters direct the scattered signal into the spectrometer.

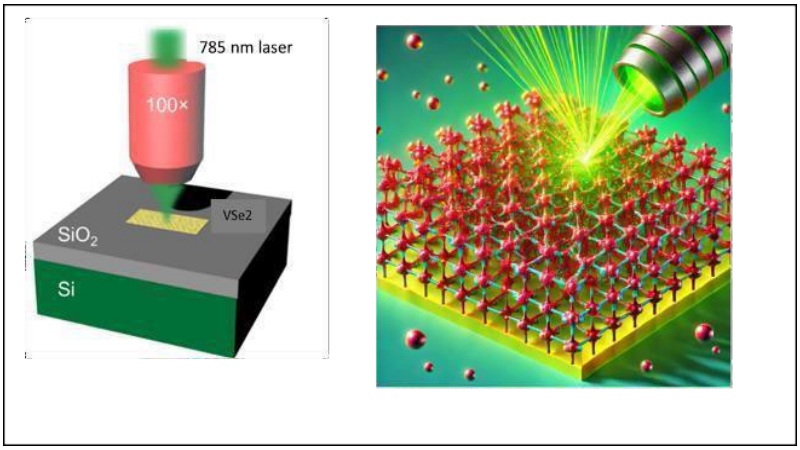


Figure 48: Schematic of the confocal Raman laser treatment system.

3.3 Plasma Etching Equipment

After laser modifications, samples underwent one or more plasma etching processes to remove either the newly oxidized material or sections of pristine VSe_2. Three different plasma systems were employed, each selected for its unique gas chemistry and ion density profile:

RF Plasma Etcher: Uses Ar, N_2, and O_2 to enable mild surface modification or oxidation.

ICP Plasma Etcher (Fluorine-based): Utilizes SF_6 or C for aggressive, anisotropic etching. **ICP Plasma Etcher (Chlorine-based):** Uses Cl_2 and related gases for alternative selectivity and etch profiles. Each case involved controlling gas flow rate, RF or ICP power, chamber pressure, and etch duration to achieve desired selectivity. The iterative combination of laser processing and plasma etching enabled controlled thickness variations, patterning, or complete removal of upper layers.

3.4 Characterization Methods

A suite of characterization tools was used to assess the laser treatment and plasma processing effects, focusing on morphology, thickness, magnetic behavior, and elemental composition.

Scanning Electron Microscopy (SEM): Provided surface morphology and contrast differences between etched and unetched regions.

Atomic Force Microscopy (AFM): Yielded high-resolution thickness and roughness profiles.

Magnetic Force Microscopy (MFM): Measured local magnetic variations correlated with thickness changes.

Superconducting Quantum Interference Device (SQUID) Magnetometry: Quantified magnetization as a function of temperature and external field. **Magneto-Optical Kerr Effect (MOKE):** Offered surface-sensitive hysteresis loop measurements to differentiate surface vs. bulk magnetism.

Raman Spectroscopy: Used post-processing to detect vibrational shifts related to oxidation, defect formation, or material removal.

Energy Dispersive X-ray Spectroscopy (EDS): Confirmed elemental composition and oxidation state changes.

3.5 Heat Transfer Effects

During laser-induced local annealing, significant effects were observed at the edges of the flake, even when treatment was applied several microns away.

This effect is attributed to heat transfer mechanisms.

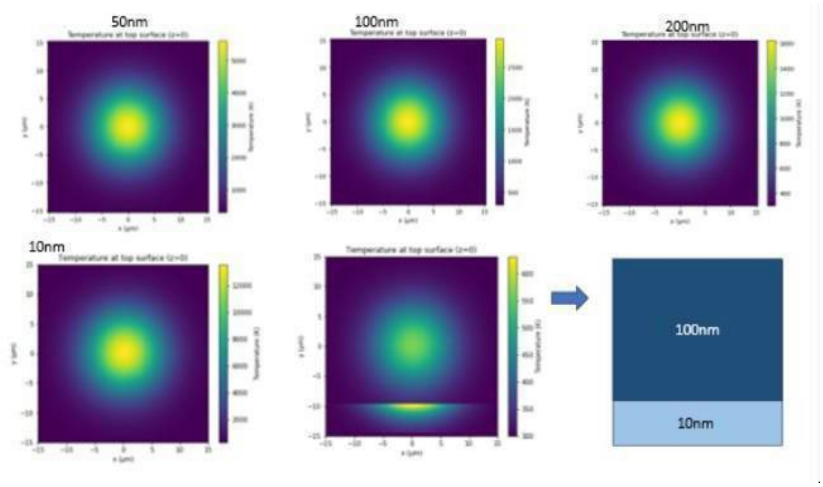


Figure 49: Simulated heat distribution for VSe_2 flake.

As heat propagates in all directions, its effect is more pronounced at the edges where the number of layers is lower. The reduced thickness in these regions leads to higher localized temperatures, promoting oxidation or evaporation.

These effects were validated through experimental Raman and AFM measurements.

3.6 Magnetic Characterization

Magnetic characterization was performed using MFM, SQUID, and MOKE techniques. The. results confirmed that thinner VSe_2 regions exhibit a stronger

magnetic moment, consistent with theoretical predictions of monolayer ferromagnetism.

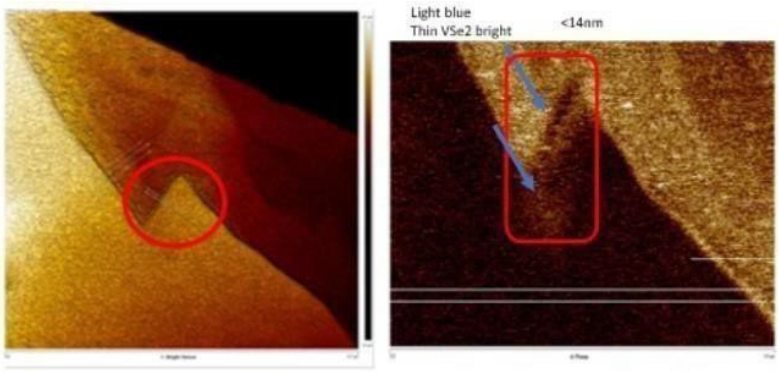


Figure 50: MFM results showing the correlation between thickness and magnetic moment.

3.7 Plasma Etching Selectivity

Selective plasma etching was performed to differentiate between VSe_2 and V2O5. Chlorine plasma etching preferentially removed VSe_2 while preserving V2O5, whereas CF4 plasma selectively etched V2O5. This enabled precise patterning and layer-by-layer removal. 3.8 Theoretical Correlation Between Se Vacancies and Magnetism. Density Functional Theory (DFT) simulations were used to explore the effect of selenium vacancies on the magnetic moment. The results indicate a direct correlation between increased Se vacancy concentration and an enhanced magnetic moment, likely due to Jahn– Teller distortions.

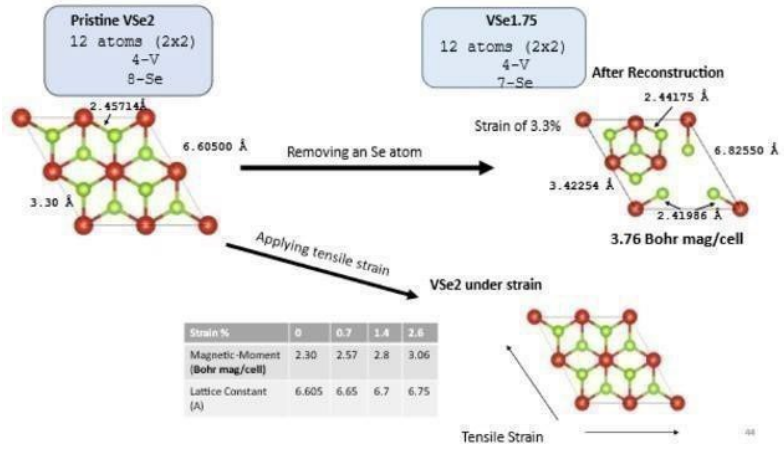


Figure 51: DFT calculations showing the effect of Se vacancies on the magnetic moment.

3.8 Summary

This chapter presented the experimental methodology for laser treatment and plasma etching of VSe_2. The workflow integrates a confocal Raman-based laser system for precise material modification with selective plasma etching techniques. Characterization through SEM, AFM, MFM, SQUID, MOKE, Raman, and EDS ensures a comprehensive understanding of structural, magnetic, and compositional transformations. The insights gained from these techniques provide a robust foundation for the controlled fabrication of 2D materials with tunable electronic and magnetic properties.

3.10 Discussion

Tunneling magnetoresistance (TMR) devices are essential components of modern spintronics, as they translate the relative orientation of ferromagnetic layers into substantial variations in electrical resistance [85].

In conventional TMR junctions— exemplified by CoFeB/MgO structures—engineered interfaces and high-quality tunnel barriers yield significant TMR ratios, often in the hundreds of percent [86]. However, there has been growing interest in transitioning these concepts to twodimensional (2D) van der Waals (vdW) materials for potentially disruptive applications: ultrathin memories, flexible spin circuits, and gate-tunable magnetism [87]. At the same time, a number of fabrication hurdles arise. These challenges include controlling the thickness and uniformity of insulating barriers on atomically thin crystals, managing contamination from lithographic resists, and stabilizing magnetic order—often with in-plane magnetization—in extremely thin layers. Indeed, many 2D magnets (such as VSe_2) are prone to surface reactions and can lose their magnetic or electronic properties when exposed to oxygen, moisture, or certain process chemicals.

Consequently, conventional top-down methods involving electron-beam lithography, photoresists, and chemically aggressive patterning have proven less than ideal. Moreover, achieving perpendicular magnetic anisotropy (PMA) is frequently a necessity for robust spintronic performance, but many 2D magnets intrinsically prefer in-plane magnetization. Strategies to induce or enhance PMA include interfacial strain, selective doping, or stacking with other magnetic materials— each of which poses further fabrication complexities. These concerns collectively motivate the need for a reproducible method to form highquality oxide barriers and define device geometries with minimal contamination, while also offering a handle to

tune magnetic anisotropy at the nanoscale.

To address these limitations, a “hybrid” fabrication approach has been proposed, demonstrated on vanadium diselenide (VSe_2). The term “hybrid” reflects its two-step nature: (i) laser-induced oxidation, and (ii) inductively coupled plasma (ICP) etching. In this scheme, a confocal laser with power up to 100 mW is focused onto the VSe_2 surface in a controlled ambient environment (often ambient air or a lowpressure O_2 atmosphere), promoting localized oxidation to form V_2O_5. By tuning the laser dwell time, spot size, and scanning speed, the thickness and lateral area of V_2O_5 can be precisely defined, down to a few nanometers of oxide. Such a process eliminates the need for polymeric masks or photoresist layers that typically contaminate 2D surfaces, thus mitigating defect creation that would compromise TMR performance. The subsequent ICP etch step leverages different etch rates of VSe_2 vs. V_2O_5 to achieve *selective removal*: one can remove the oxide and preserve pristine VSe_2 $_2$ in defined regions or selectively etch the unconverted VSe_2 and retain the oxide layer. In the context of TMR devices, a uniform, ultrathin oxide on top of a conductive or ferromagnetic 2D crystal can serve as the tunnel barrier— provided it is sufficiently defect-free. Traditional thin-film processes like ALD or sputtering are often challenging on 2D materials because they can damage the fragile surface; by contrast, this laser-based oxidation occurs at the surface itself with minimal scattering or redeposition, and the ICP step refines the resulting geometry without contact. The synergy between “laser writing” and “plasma etching” stands out as a powerful method to define

complex patterns— barriers, leads, multi-junction arrays—entirely mask-free [89], [90].

One significant benefit of this hybrid approach is *improved interface quality*, which is paramount for attaining high TMR ratios [85]. Defects or partial oxidation at the barrier interface commonly degrade the electron spin polarization [99]. By controlling the oxidation from the top down, the barrier is integrated into the 2D crystal's surface structure, potentially ensuring a sharper and more uniform interface. Additionally, because the technique does not rely on multi-step lithography, it avoids many sources of contamination such as photoresist residue or developer- induced surface roughening. This is crucial for 2D magnets like VSe_2, which are sensitive to process conditions and can exhibit metastable phases if overexposed to chemicals [100].

The hybrid method may also enhance *magnetic anisotropy* in such materials. Many 2D magnets exhibit predominantly in-plane magnetization when mechanically exfoliated or grown by molecular beam epitaxy, limiting their utility in perpendicular TMR architectures [87]. However, partial oxidation or doping at the surface can introduce strain fields or shift the band structure, thereby changing the balance of magnetic exchange interactions [91].

Beyond VSe_2 itself, this technique is broadly adaptable. Many transition metal dichalcogenides (TMDs)—MoS_2, WS_2, and WSe_2—are known to oxidize in laser driven processes, sometimes forming stable oxides that can act as passivation or doping layers [89] [101] [102].

Similarly, other 2D magnets like Fe_3GeTe_2 or $MnBi_2Te_4$ (MBT) might be selectively oxidized or partially doped to adjust their Curie temperatures or magnetic anisotropies, although care is needed to damaging the entire flake [94]. The subsequent ICP step, employing fluorinated or oxygen-based plasmas, is already standard in microelectronics for patterning thin films. By tuning gas flow rates, chamber pressure, and plasma power, one can tailor etch selectivity for each 2D material vs. its oxide [50]. Such control allows for the construction of vertical or lateral "multi-tunnel" junctions by repeating the oxidize-and-etch cycle multiple times. For instance, one might create alternating oxide–magnetic regions in the same flake or stack multiple 2D magnets with intervening oxide barriers by layering each flake sequentially via a dry- transfer method. The key advantage is that all these complex topographies—imperative for advanced spintronic devices—are achieved *without* photoresists or conventional masks, significantly cutting down on contamination and process complexity [95], [96].

In terms of TMR device optimization, there are still practical considerations. Laser beam uniformity and repeatability must be carefully managed to achieve consistent oxide thickness over large areas; local hotspots or variations in spot intensity could yield an uneven barrier and degrade the TMR ratio. Real-time monitoring techniques (e.g., reflectometry or Raman spectroscopy) may be beneficial for ensuring uniform oxidation [97]. The environment matters as well: controlling oxygen partial pressure, humidity, or temperature can improve the stoichiometry of the oxide that forms. On the plasma side, each 2D crystal

may necessitate a customized plasma recipe to achieve high selectivity between oxide and parent material. Excessive ion bombardment risks damaging or doping unintended regions, whereas insufficient plasma reactivity might leave residue or lead to incomplete etching [96]. Despite these challenges, the method is readily scalable: large-area lasers, galvanometric scanning heads, and ICP tools are all standard in semiconductor manufacturing. Consequently, an industrial pipeline could incorporate an in- line process where CVD-grown 2D films are loaded, laser-patterned, and etched without repeated mask alignment. This synergy can drastically reduce fabrication cycles for TMR devices or more exotic spintronic circuits that exploit domain walls, spin-wave propagation, or even resonant tunneling in multi-barrier junctions. On a broader scale, the *prospects for engineering magnetic properties* through localized oxidation open new frontiers. The ability to generate or remove a surface oxide with micron or submicron resolution provides a direct handle on doping, strain, and phase transitions that define a 2D magnet's behavior. For instance, one could conceive of "patchwork magnetism," where certain regions of a flake are oxidized enough to shift from in-plane to out-of-plane magnetization. Such an approach might enable domain-wall logic or zone-specific memory bits, all structured in a single contiguous crystal. Furthermore, materials like V2O5, which can be formed atop VSe_2, have well- known applications in Li-ion battery electrodes, suggesting that integrated energy storage elements could be fabricated alongside spintronic devices [93]. As TMR structures demand exacting control of interfaces and barrier thickness, the hybrid (laser + ICP) process meets a key requirement

for next-generation 2D spintronics: a mask-free, tunable, and relatively low temperature route to pattern magnets and insulators side by side. Overall, while further refinements in laser process stability, doping control, and plasma selectivity are needed, this hybrid method is poised to accelerate the deployment of 2D TMR devices. By simplifying the workflow and offering

powerful local engineering of magnetic and electronic properties, it expands the design space for spin-based technologies, bridging the gap between lab-scale demonstrations and industrial-scale manufacturing.

4. Conclusion

The research presented in this dissertation establishes a novel hybrid fabrication approach for tailoring the structural, electronic, and magnetic properties of vanadium diselenide (VSe_2) through controlled laser processing and selective plasma etching. By leveraging the unique response of VSe_2 to these treatment techniques, we have demonstrated precise control over oxidation, thinning, and etching at the nanoscale. These methods pave the way for scalable fabrication of van der Waals (vdW) heterostructures with tunable properties, offering significant implications for spintronics, quantum materials, and advanced energy storage applications.

4.1 Key Findings and Contributions

One of the major achievements of this study is the demonstration of **laser assisted oxidation of VSe_2**, forming vanadium pentoxide (V_2O_5) layers with precise spatial control. The ability to convert VSe_2 into V_2O_5 through

confocal laser treatment enables the de-sign of patterned oxide interfaces without the need for traditional lithographic masks. This localized oxidation process, validated through Raman spectroscopy and energy dispersive spectroscopy (EDS), eliminates surface contamination issues associated with polymer-based patterning, ensuring high purity and structural integrity of the modified regions. Furthermore, **selective plasma etching strategies** were developed to control material removal in a highly targeted manner. Chlorine (Cl_2) plasma was shown to preferentially etch VSe_2 while leaving V2O5 intact, allowing the use of laser formed V_2O_5 as an etch mask. Conversely, fluorine- based (CF_4) plasma etching enabled selective removal of V_2O_5 while preserving underlying VSe_2, demonstrating precise layer engineering capabilities. This two-step plasma approach highlights the potential of hybrid processing to achieve site-specific material modifications, critical for integration into device architectures. Additionally, this research provides new insights into the **magnetic properties of VSe_2**, particularly in relation to thickness and defect engineering. Through atomic force microscopy (AFM) and magnetic force microscopy (MFM) measurements, it was observed that thinner VSe_2 flakes exhibit enhanced magnetic moments, consistent with theoretical predictions of monolayer ferromagnetism. Density functional theory (DFT) simulations further elucidated the role of selenium (Se) vacancies in stabilizing ferromagnetic order, revealing a correlation between defect induced strain and increased magnetic moments via Jahn–Teller (JT)

distortion. These findings suggest a promising route for tailoring the magnetic behavior of VSe_2 through controlled defect engineering, expanding its potential for spintronic applications.

4.2 Broader Implications and Future Directions

The methodologies developed in this work contribute to the broader field of **2D material fabrication and device integration**.

The demonstrated hybrid approach— combining laser processing with selective plasma etching— addresses critical challenges in achieving nanoscale control over vdW materials, offering an alternative to conventional bottom-up growth techniques. The insights gained from this study can be extended to other transition metal dichalcogenides (TMDs), enabling the scalable production of heterostructures with customized electronic and magnetic functionalities.

From a technological perspective, the ability to pattern oxide interfaces with submicron precision opens new opportunities in **next-generation spintronic and quantum devices**. By modulating magnetic anisotropy through controlled oxidation and strain engineering, this approach can facilitate the development of 2D magnetic tunnel junctions (MTJs), spin filters, and other low- power magnetic memory technologies. Additionally, the use of V_2O_5 as a functional oxide layer presents avenues for integrating energy storage components within vdW-based electronic systems, such as hybrid lithium-ion battery architectures. Moving forward, several key areas warrant further exploration:

Optimization of Laser Processing Parameters – Further refinements in laser power, dwell time, and ambient conditions could enhance precision and reproducibility. Real-time monitoring techniques, such as in situ Raman spectroscopy, could be employed to dynamically track oxidation states during processing.

Advanced Plasma Etching Strategies – Future work could explore

additional halogen chemistries (e.g., BCl_3, SF_6) to achieve greater selectivity and patterning resolution.

Electronic and Spin Transport Measurements – Hall effect, magnetoresistance, and tunneling magnetoresistance (TMR) measurements would provide direct insights into the feasibility of these materials for spintronic applications.

- **Exploration of Other 2D Materials** – The developed methodology could be extended to other TMDs, such as $MoSe_2$, WS_2, or Fe_3GeTe_2, to compare oxidation kinetics, defect- induced magnetism, and plasma etching selectivity.
- **Integration into Scalable Device Architectures** – The compatibility of these methods with existing semiconductor fabrication techniques should be further evaluated, with an emphasis on automation and reproducibility.

In summary, this dissertation presents a comprehensive study on the controlled fabrication, modification, and characterization of VSe_2 using hybrid laser and plasma processing. The results demonstrate a powerful and scalable approach for engineering 2D materials with tailored electronic and magnetic properties. By bridging fundamental material science with practical device fabrication techniques, this work lays the foundation for the next generation of vdW-based electronic and spintronic technologies. The insights gained herein not only enhance our understanding of laser-induced oxidation and plasma etching selectivity but also open new avenues for designing functional 2D heterostructures with unprecedented precision.

5. Methodology

5.1 Sample Preparation

Crystal Fabrication via Chemical Vapor Deposition (CVD)

A common approach to synthesizing VSe_2 via chemical vapor deposition (CVD) involves co- evaporating or thermally decomposing suitable vanadium and selenium precursors in a controlled atmosphere. Typically, a two-zone furnace is employed, where vanadium precursors (e.g., VCl_4 or metallic vanadium) and selenium powder are placed in separate zones. Under an inert gas flow—often argon or a mixture of Ar/H_2—the furnace is heated to temperatures ranging from 500°C to 900°C, enabling the formation of gaseous vanadium and selenium species. These species then diffuse to a heated substrate (e.g., SiO_2/Si or sapphire) in the downstream zone, where they react and condense to form layered VSe_2. Precise control over precursor ratios, growth temperature, carrier gas flow, and growth time is critical for achieving high-quality monolayer or few-layer VSe_2. After growth, the system is usually cooled slowly in a selenium rich or inert ambient to minimize defects and maintain stoichiometry. This method allows for scalable and relatively uniform synthesis of 2D VSe_2, essential for subsequent device fabrication and characterization.

Mechanical Exfoliation of 2D van der Waals Materials

Two-dimensional (2D) van der Waals (vdW) materials, such as graphene and transition-metal dichalcogenides, were prepared via mechanical exfoliation of high quality bulk crystals. The process began by cleaving the crystals with adhesive tape to isolate thin layers, followed by iterative peeling until flakes sufficiently thinned to be identified under an optical

microscope. The substrates used were silicon wafers with a 300 nm thermally grown oxide layer (Si/SiO_2), which were cleaned in acetone and isopropanol before being dried under a nitrogen stream. The tape carrying the exfoliated material was then carefully pressed onto the cleaned substrate, allowing the thin flakes to

transfer. Optical microscopy was subsequently employed to verify the presence of mono- or few layer regions, ensuring the selection of high-quality flakes for subsequent experiments.

5.2 Characterization Techniques

Raman Spectroscopy

A Renishaw In Via confocal Raman spectrometer was employed to both laser treat and subsequently characterize the VSe_2 (or V_2O_5) flakes. First, a 785 nm laser line was used for localized laser processing in mapping mode, systematically scanning across the flake at power settings of 25 mW, 50 mW, or 100 mW to induce controlled modifications. A 50× objective lens was selected for these scans, ensuring a sufficiently high spatial resolution for patterning. Following the treatment step, Raman spectra were collected in extended scan mode at a reduced laser power of 1 mW for 60 seconds, minimizing damage while capturing reliable vibrational signatures of the sample. This two-step procedure—laser treatment followed by lower-power Raman measurement— allowed for precise tuning and subsequent spectroscopic confirmation of any structural or chemical changes in the material.

Scanning Electron Microscopy (SEM) and Energy-Dispersive X-ray Spectroscopy (EDS)

A ThermoFisher Nova Nano 230 variable pressure scanning electron microscope (SEM), equipped with an energy-dispersive X-ray spectroscopy (EDS) detector, was employed to investigate both the morphology and elemental composition of the samples. Variable pressure conditions helped mitigate charging artifacts, allowing for high-resolution imaging of the 2D

flakes. For the EDS measurements, an acceleration voltage of 15 keV was used to effectively detect selenium signals. Prior to analysis, the samples were mounted on conductive carbon tape to enhance electron conduction and reduce charging.

SEM micrographs were acquired at various magnifications to assess surface features and flake uniformity, while EDS point and area scans provided elemental maps confirming the presence and distribution of selenium and other relevant elements.

Atomic Force Microscopy (AFM) and Magnetic Force Microscopy (MFM) Scanning probe microscopy (SPM) was utilized to examine both the surface topography and local magnetic domains of the 2D flakes, employing two Bruker instruments for distinct measurement modes. First, magnetic force microscopy (MFM) was performed on a Bruker Dimension Icon SPM, using magnetically coated probes to detect and map out nanoscale magnetic features. This approach involved a two-pass scanning method, where the first pass captured the sample's topography, and a subsequent elevated "lift" scan recorded phase shifts attributable to magnetic interactions. Meanwhile, atomic force microscopy (AFM) was conducted on a Bruker Dimension FastScan SPM in tapping (or PeakForce)

mode, providing rapid and high resolution topographical images of the flake surfaces. Together, these complementary techniques offered a comprehensive view of both the morphological and magnetic properties of the samples at the nanoscale.

5.3 Plasma Etching

Plasma treatments involved three primary systems. First, low-power radio frequency (RF) cleaning was conducted using a Gatan Plasma System SOLARUS, operating at up to 50 W for as long as 10 minutes; this approach served primarily as a surface cleaning step without significantly etching the material. More aggressive etching was achieved via inductively coupled plasma (ICP) processes.

For VSe_2, a chlorine-based etch was performed on a Plasma Therm SLR 770 ICP, using an ICP power of 800 W and an RF bias of 100 W, with BCl3 (20 sccm), Ar (10 sccm), and Cl_2 (60 sccm) as process gases. Under these conditions, VSe2 was effectively removed within a 10-second process window, where the high ICP power generated a dense plasma and the elevated RF bias supplied sufficient ion bombardment to break surface bonds and remove sub- chloride or passivation layers; BCl_3 and Cl_2 together formed a highly reactive chlorinated environment, while Ar contributed to physical sputtering.

In contrast, a fluorine-based etch was used for V_2O_5 on an STS AOE system, operating at a lower ICP power of 500 W, an RF bias of 50 W, and a chamber pressure of 15mTorr. Gas flows of O_2 (40 sccm) and CF_4 (30 sccm) over a 30second treatment selectively removed V_2O_5 by forming volatile oxyfluorides, while leaving VSe_2 largely untouched. Here, the

reduced power settings favored chemical etching of the oxide over sputter induced removal of the selenide, and the moderate chamber pressure facilitated reactive species transport without extensive passivation of VSe_2.

6. References

[1] K. S. Novoselov and A. K. Geim, "Electric field effect in atomically thin carbon films," *Science*, vol. 306, no 5696, pp. 666–669, 2004, doi: 10.1126/science.1102896.

[2] S. Z. Butler, S. M Hollen, L. Cao, et al., "Progress, challenges, and opportunities in two- dimensional materials beyond graphene," *ACS Nano*, vol. 7, no. 4, pp. 2898– 2926, 2013, doi:10.1021/nn400280c.

[3] Y. Hernandez, V. Nicolosi, M. Lotya, et al., "High-yield production of graphene by liquid- phase exfoliation of graphite," *Nature Nanotechnology*, vol. 3, no.9, pp. 563– 568, 2008, doi: 10.1038/nnano.2008.215.

[4] X. Li and R. S Ruoff, "Evolution of graphene growth on Ni and Cu by carbon isotope labeling," *Nano Letters*, vol. 9, no. 12, pp. 4268–4272, 2009, doi: 10.1021/nl902515k.

[5] Y. Shi, H. Li and L. J. Li, "Recent advances in controlled synthesis of 2D transition metal dichalcogenides via vapor deposition techniques," *Chemical Society Reviews*, vol. 44, no. 9, pp. 2744–2756, 2015, doi: 10.1039/C4CS00256C.

[6] K. F Mak, C. Lee, J. Hone, J. Shan and T. F. Heinz, "Atomically Thin MoS2: A New Direct- Gap Semiconductor," *Phys. Rev. Lett*., vol. 105, 2010, doi:10.1103/PhysRevLett.105.136805.

[7] H. R. Gutiérrez et al., "Extraordinary room-temperature photoluminescence in triangular WS_2 monolayers," *Nano Letters*, vol. 13, no. 8, pp. 3447–3454, Aug. 2013, doi: 10.1021/nl3026357.

[8] C. R. Dean et al., "Boron nitride substrates for high-quality graphene electronics," *Nature Nanotechnology*," vol. 5, no. 10, pp. 722–726, 2010, doi: 10.1038/nnano.2010.172.

[9] W. Wang, A Carl and R.Gorbachev, "Clean assembly of van der Waals heterostructures using silicon nitride membranes," *Nature Electronics*, vol 6, no. 12,
pp. 981–990, 2023.

[10] S. H. Choi et al., "Large-scale synthesis of graphene and other 2D materials towards industrialization," Nature Communications, vol. 13, no. 1, article 1484, Mar. 2022, doi: 10.1038/s41467-022-29182-y.

[11] M. Lotya, P. J. King and U. Khan et al., "High-concentration, surfactant-stabilized graphene dispersions," *ACS Nano*, vol. 4, no.6, pp. 3155–3162, 2010, doi: 10.1021/nn1005304.

[12] A. Gurarslan et al., "Surface-energy-assisted perfect transfer of centimeter-scale monolayer and few-layer MoS_2 films onto arbitrary substrates," *ACS Nano*, vol. 8, no. 11, pp. 11522– 11528, 2014, doi: 10.1021/nn5057673.107

[13] J. N. Coleman, M. Lotya, A. O'Neill et al., "Two-dimensional nanosheets produced by liquid exfoliation of layered materials," *Science*, vol. 331, no. 6017, pp. 568–571, 2011, doi: 10.1126/science.1194975.

[14] S.-J. Chang et al., "Graphene growth from reduced graphene oxide by chemical vapour deposition: seeded growth accompanied by restoration," *Scientific Reports*, vol. 6, Art. no. 22653, 2016, doi: 10.1038/srep22653.

[15] Z. Xu et al., "1T MoS_2 growth from exfoliated MoS_2 nucleation as high rate anode for sodium storage," Nanotechnology, vol. 33, no. 2, p. 025001, 2022, doi: 10.1088/1361-6528/ac2d09.

[16] J.J. Pyeon et al., "Wafer-scale growth of MoS_2 thin films by atomic layer deposition," Nanoscale, vol. 8, no. 20, pp. 10792–10798, 2016, doi: 10.1039/C6NR01346E.

[17] V. Nicolosi, M. Chhowalla, M. G. Kanatzidis, et al., "Liquid exfoliation of layered materials," *Science*, vol. 340, no. 6139, Article number 1226419, 2013, doi: 10.1126/science.1226419.

[18] X. Huang, X. Rui, H. H Hng and Q.Yan, "Vanadium pentoxide-based cathode materials for lithium-ion batteries: morphology control, carbon hybridization, and cation doping," *Particle & Particle Systems Characterization*, vol. 32, no. 3, pp. 276-294, 2015.

[19] K.B. Φstreng, Y. Gandrud, Y. Hu, O. Nilsen and H. Fjellvag, "High power nano- structured V2O5 thin film cathodes by atomic layer deposition," *J. Mater Chem. A*., vol. 2, no. 36, pp. 15044-15051, 2014, doi: 10/1039/C4TA00694

[20] J. A Wilson, F. J. Di Salvo, and S. Mahajan, "Charge-density waves and superlattices in metallic layered transition metal dichalcogenides," *Advances in Physics*, vol. 24, no.2, pp.117–201, 1975.

[21] P. Chen, X. Xu, Y. Chen, D. Chen and X. Zhang, "Structural distortions and phase transitions in 2D VSe2 and their applications," *Nano Letters*, vol.19, no. 8, pp. 5184– 5191, 2019.

[22] M. Chhowalla, H.S. Shin, G. Eda, L.J Li, K. P Loh and H. Zhang, "The chemistry of two- dimensional layered transition metal dichalcogenide nanosheets," *Nature Chemistry*, vol. 5, pp. 263–275, 2013.

[23] S. Manzeli, D. Ovchinnikov, D. Pasquier, O. V. Yazyev and A. Kis, "2D transition metal dichalcogenides," *Nature Reviews Materials*, vol. 2, Art. no. 17033, 2017, doi: 10.1038/natrevmats.2017.33.

[24] S. Kaushik, T. Mehta, P. Chand, S. Sharma, G. Kumar, "Recent advancements in cathode materials for high- performance Li-ion batteries: Progress and prospects," *Journal of Energy Storag*e. 2024, 97:112818.

[25] X. Ma, Y. Feng and L. Miao, "Investigation of the metallic TMD VSe2: Synthesis, electronic structure, and potential device implementations," *Journal of Physical Chemistry C*, vol. 124, no. 13, pp. 7213–7221, 2020.

[26] M. Bonilla, S. Kolekar, Y. Ma, H. C. Diaz, V. Kalappattil, R. Das, T. Eggers,
H. R. Gutierrez, M. H. Phan and M. Batzill, "Strong room-temperature ferromagnetism in VSe2 monolayers on van der Waals substrates," *Nature Nanotechnology*, vol. 13, pp. 289–293, 2018.

[27] J. Feng, S. Li, Z. Qian, X Qi and Y. Hou, "Emerging 2D VSe2 materials: Synthesis, properties, and device applications," *Advanced Functional Materials*, vol. 28, no. 45, Art. no. 1804281, 2018.

[28] J.Livage, "Vanadium Pentoxide Gels," *Chem. Mater.* 1991, *3*, 578– 593, doi: 10.1021/cm00016a006

[29] M. S. Whittingham, "Lithium batteries and cathode materials," *Chemical Reviews*, vol. 104, no. 10, pp. 4271–4302, 2004.

[30] R. Santos, *et al.* (2013). *Thermoelectric properties of V_2O_5 thin films deposited by thermal evaporation*. *Applied Surface Science*, 282, 590–594. https://doi.org/10.1016/j.apsusc.2013.06.016

[31] G. Guzman, R. Morineau, and J. Livage, "Synthesis of vanadium dioxide thin Films from vanadium alkoxides," *Materials Research Bulletin*, vol 29, no. 5, pp. 509-15, 1994.

[32] X. Chen et al., "Ozone-Based Atomic Layer Deposition of Crystalline V_2O_5 Films for High Performance Electrochemical Energy Storage," Chemistry of Materials, vol. 24, no. 7, pp. 1255–1261, 2012, doi: 10.1021/cm202901z.

[33] Y. Rong, Y. Cao, N. Guo, Y. Li, W. Jia and D. Jia, "A simple method to synthesize V2O5 nanostructures with controllable morphology for high performance Li-ion batteries,"
Electrochimica Acta vol. 222, pp.1691-9, 2016.

[34] M. Gibertini, M. Koperski, A. F. Morpurgo and K. S. Novoselov, "Magnetic 2D Materials and heterostructures," *Nature Nanotechnology*, vol.14, pp. 408–419, 2019.

[35] N. Samarth, "Condensed-matter physics: Magnetism in flatland," *Nature*, vol. 546,
pp. 216– 218, 2017.

[36] W. Zhang, P. K. J. Wong, R. Zhu and A. T. S. Wee, "Van der Waals magnets: Wonder building blocks for two-dimensional spintronics?," *InfoMat*, vol. 1, no. 4,
pp. 479–495, 2019.

[37] B. Huang, G Clark, E. Navarro-Moratalla, et al, "Layer-dependent

ferromagnetism in a van der Waals crystal down to the monolayer limit," *Nature*, vol. 546, Art. no. 7657, pp. 270–273, 2017.

[38] W. O. Chen, Z. Y. Sun, Z. J. Wang, et al. "Direct observation of the layer-dependent electronic structure in the van der Waals ferromagnetic CrVI3 by ARPES. *Science*, vol. 366, Art. no. 6464, pp. 983–987, 2019.

[39] B. Huang, G. Clark D. R. Klein, et al, "Electrical control of 2D magnetism in bilayer CrI3,"*Nature Nanotechnology*, vol. 13, no. 7, pp. 544–548, 2018.

[40] F. Matsukura, Y. Tokura and H. Ohno, "Control of magnetism by electric fields,"
Nature Nanotechnology, vol.10, no. 3, pp. 209–220, 2015.

[41] C. Gong, L. Li, Z. Li. et al., "Discovery of intrinsic ferromagnetism in two- dimensional van
der Waals crystals," *Nature*, vol. 546, Art. no. 7657, pp. 265–269, 2017.

[42] Y. J Deng, Y. J. Yu, Y. C. Song, et al., "Gate-tunable room-temperature ferromagnetism in two-dimensional Fe3GeTe2," *Nature*, vol. 563, Art. no. 7729, pp. 94–99, 2018.

[43] Z. Y Wang, C. Tang, R. Sachs, et al., "Proximity-induced ferromagnetism in graphene revealed by the anomalous Hall effect," *Physical Review Letters*, vol. 114, no.1, Art. no. 016603, 2015.

[50] J. G. Feng, D. Biswas, and A.Rajan, et al., "Electronic structure and enhanced charge- density wave order of monolayer VSe2," *Nano Letters*, vol. 18, no. 7, pp. 4493–4499. (2018).

[51] P. Chen, W. W. Pai, Y. H. Chan et al., "Unique gap structure and symmetry of the charge density wave in single-layer VSe2," *Physical Review Letters*, vol. 121, no. 19, Art. no.196402, 2018.

[52] K. Xu, P. Z, Chen, X. L. Li, et al., "Ultrathin nanosheets of vanadium diselenide: A metallic two-dimensional material with ferromagnetic charge-density-wave behavior," *Angewandte Chemie International Edition*, vol. 52, no. 40, pp. 10477–10481, 2013.
.

[53] Chua, R., et al., "Reconstructed defect line effects in VSe2: From experiment to theory,"
Advanced Materials, vol. 32, no. 24, Art. no. e2000693, 2020.

[54] Y. D Ma, Y. Dai, M.Guo et al., "Evidence of the existence of magnetism in pristine VX2 monolayers (X = S, Se) and their strain-induced tunable magnetic properties," *ACS Nano*, vol. 6, no. 2, pp.1695–1701, 2012.

[55] J. Cenker, S. Sivakumar, K. Xie, A. Miller, P. Thijssen, Z. Liu, et al., "Reversible strain-induced magnetic phase transition in a van der Waals magnet," *Nat Nanotechnol*, vol 17, no.13, pp. 256-61, 2022.

[56] W. Ci, et al., "Thickness-dependent and strain-tunable magnetism in two-dimensional van der Waals VSe2.," *Nano Research*, vol. 15, no.10, pp. 1–7, 2022.

[57] K. Xu, P. Chen, X. Li, C. Wu, Y. Guo, J. Zhao, X. Wu and Y. Xie, "Ultrathin nanosheets of vanadium diselendide: A metallic two-dimensional material with ferromagnetic charge-density-wave behavior," *Angewandte Chemi International Edition*, vol. 52, no. 40, pp. 10477-10481, 2013.

[58] E.C. Ahn, "2D materials for spintronic devices," *npj 2D Mater Appl 4*, vol. 17, 2020https://doi.org/10.1038/s41699-020-0152-0

[59] Q. Cao, F.F. Yun, L. Sang, F. Xiang, G. Liu and X. Wang, "Defect introduced paramagnetism and weak localization in two-dimensional metal VSe2," *Nanotechnology*, vol. 28, no. 47, Art. No. 475703, 2017.

[60] W. Yu, J. Li, T.S. Herng, Z. Wang, X. Zhao, X. Chi et al., "Chemically exfoliated VS2 Monolayers with room-temperature ferromagnetism," *Advanced Materials*, vol. 31, no. 39, Art no. 1903779, 2019, doi: 10.1002/adma.201930779.

[61] Chua, R., et al., "Reconstructed defect line effects in VSe2: From experiment to theory,"*Advanced Materials*, vol. 32, no. 24, Art. no. e2000693, 2020.

[63] H. Liu, L. Bao, Z. Zhou, B. Che, R. Zhang, C.Bian, et al., "Quasi-2D transport and weak antilocalization effect in few-layered VSe2," *Nano Letters*, vol. 19, no. 7, pp. 4551– 4559, 2019.

[64] Parker JC. Raman scattering from VO2 single crystals: A study of the effects of surface oxidation. Phys Rev B Condens Matter. 1990 Aug 15;42(5):3164-3166. doi: 10.1103/physrevb.42.3164. PMID: 9995815.

[65] N. Kuroda and H. Y. Fan, "Raman scattering and phase transitions of V_2O_3," *Physical Review B*, vol.16, no.11, pp. 5003–5008, 1977, doi:10.1103/PhysRevB.16.5003.

[66] S.W. Park, Y.J. Jo, S. Bae, B.H. Hong, S.K. Lee, "Synthesis of Large-Scale Transition Metal Dichalcogenides for Their Commercialization," *Applied Science and Convergence Technology*, vol. 29, pp. 133-142, 2020, https://doi.org/10.5757/ASCT.2020.29.6.133

[68] T. G. Ulusoy Ghobadi, B. Patil, F. Karadas, A. K. Okyay and E. Yilmaz, "Catalytic properties of vanadium diselenide: A comprehensive study on its electrocatalytic performance in alkaline, neutral, and acidic media," *ACS Omega,* vol. 2, no.11, pp. 8319– 8329, 2017, https://doi.org/10.1021/acsomega.7b01226

[69] Hyo-Chang Lee, “Review of inductively coupled plasmas: Nano-applications and bistable hysteresis physics,” *Appl. Phys. Rev.* 1, vol. 5, no. 1, 011108, March 2018. https:// doi.org/10.1063/1.5012001

[70] P. M Marley, T. A. Abtew, K. E. Farley, G. A. Horrocks, R. V. Dennis, P. Zhang and

S. Banerjee, “Emptying and filling a tunnel bronze,” *Chemical Science*, vol. 6, no. 3,
pp. 1712–1718, 2015, https://doi.org/10.1039/C4SC03748K

[71] D. S Rawal, A. Kapoor, H. S. Sharma, B. K. Sehgal and H. K. Malik, “A highly selective low pressure inductively coupled plasma etching process for GaAs using photoresist mask,” *The Open Plasma Physics Journal*, vol. 4, pp. 34–39, 2011
https://doi.org/10.2174/1876534301104010034

[74] C.G.N Lee, K.J. Kanarik, R.A. Gottscho, “The grand challenges of plasma etching: a manufacturing perspective,” *Journal of Physics D: Applied Physics*, vol. 47, no. 27):273001, 2014.

[75] Steven A. Vitale, Heeyeop Chae, Herbert H. Sawin, “Silicon etching yields in
F2, Cl2, Br2, and HBr high density plasmas,” *J. Vac. Sci. Technol. A* 1, vol.19, no. 5,
pp. 2197–2206 September 2001. https://doi.org/10.1116/1.1378077

[76] S. D. Park et al., “Effect of additive gases on the selective etching of tungsten films using inductively coupled halogen-based plasmas,” Thin Solid Films, vol. 447–448, pp. 586–591, 2004. DOI: 10.1016/S0040-6090(03)01257-4.

[79] W. M. Haynes (ed.), *CRC Handbook of Chemistry and Physics*, 95th Edition, CRC Press, 2014.

[80] R. Chang, *Physical Chemistry for the Chemical and Biological Sciences*, 3rd Edition University Science Books, 2000.

[81] O. Knacke et al., *Thermochemical Properties of Inorganic Substances*, 2nd Edition Springer, 1991.

[82] P. Giannozzi, S. Baroni, N. Bonini, M. Calandra, R. Car, C. Cavazzoni, D. Ceresoli, G. L. Chiarotti, M. Cococcioni, I. Dabo, et al., "QUANTUM ESPRESSO: a modular and open- source software project for quantum simulations of materials,"
J. Phys.: Condens. Matter, vol. 21, Art. no. 395502, 2009.

[83] J. P. Perdew, K. Burke, and M. Ernzerhof, "Generalized Gradient Approximation Made Simple," *Phys. Rev. Lett*., vol. 77, Art. no. 3865, 1996.

[84] P. Giannozzi et al., "Advanced capabilities for materials

modeling with Quantum ESPRESSO," *J. Phys.: Condens. Matter*, vol. 29, Art. no. 465901, 2017.

[85] S. Yuasa and D. D. Djayaprawira, "Giant tunnel magnetoresistance in magnetic tunnel junctions with a crystalline MgO(001) barrier," *J. Phys. D: Appl. Phys*., vol. 40, R337–R354, 2007.

[86] S. Ikeda, et al., "A perpendicular-anisotropy CoFeB–MgO magnetic tunnel junction," *Nature Materials* vol. 9, pp. 721–724, 2010.

[87] Q.H. Wang, A. Bedoya-Pinto, M. Blei, A.H. Dismukes, A. Hamo, S. Jenkins, et al., "The Magnetic Genome of Two-Dimensional van der Waals Materials," *ACS Nano*, vol.16, no.5, pp. 6960-70792022.

[89] H. Wang, M. Xu, H. Ji, T. He, W. Li, L. Zheng, et al., "Laser-assisted synthesis of two-dimensional transition metal dichalcogenides: a mini review," *Frontiers in Chemistry*, vol. 11, 2023.

[90] T.S. Vo, B. Jeon, V,P.T. Nguyen, T. Hoang, K.M. Lwin, S. Han, et al., "A comprehensive review of laser processing-assisted 2D functional materials and their specific applications," *Materials Today Physics*, vol. 47, Art. No. 101536, 2024.

[91] N. Jutong, U. Eckern, T. Mairoser and U. Schwingenschlögl,"Effect of Gd doping and O deficiency on the Curie temperature of EuO," *Scientific Reports*, vol. 5, Art. No. 8038, 2015, https://doi.org/10.1038/srep08038

[93] J. Singh, K. Hong, Y.Cho, M. S. Akhtar, J. Kang and A. K Rai, "Metal-Organic Framework Fabricated V_2O_5 Cathode Material for High-Performance Lithium-Ion Batteries. Coatings," vol 12, no. 6, Art. No. 844, 2022 https://doi.org/10.3390/coatings12060844

[94] C. Gong and X.Zhang, "Two-dimensional magnetic crystals and emergent Heterostructure devices," *Science*, vol. 363, Art. no. eaav4450, 2019.

[95] J. Liang, K. Xu, B. Toncini, B. Bersch, B. Jariwala, Y-C Lin, et al., "Impact of Post- Lithography Polymer Residue on the Electrical Characteristics of MoS2 and WSe2 Field Effect Transistors," *Advanced Materials Interfaces*, vol. 6, no,3, 18013212019.

[98] L. Hu, X. Shan, Y. Wu, et al., "Laser Thinning and Patterning of MoS_2 with
Layer-by- Layer Precision," *Sci Rep* vol. 7, Art. No. 15538, pp. 15350-4, 2017, https:// doi.org/10.1038/s41598-017-

[98] G. Vinai, C. Bigi, A. Rajan, M.D. Watson, T.L. Lee, F. Mazzola, et al., "Proximity- ferromagnetism and chemical reactivity in few-layer ${\mathrm{VSe}}_{2}$ heterostructures," *Physical Review B*, vol. 101, no.3, art. No. 035404, 2020.

[99] N. D. Telling, G. van der Laan, S. Ladak and R. J. Hicken, "Spin polarization and barrier-oxidation effects at the Co/Alumina interface in magnetic tunnel junctions," *Applied Physics Letters*, vol. 85, no. 17, pp. 3803–3805, 2004,https://doi.org/10.1063/1.1812383

[100] S. Friedensen, P. Yasini, R. Keneipp, A. Castan and M. Drndić, "Solvent-induced degradation of electrochemically exfoliated vanadium selenide visualized by electron microscopy," *ACS Omega,* vol. 7, no.46, pp. 42146–42154, 2022, https:// doi.org/10.1021/acsomega.2c04749

[101] A. Alrasheed, J.M. Gorham, B.C. Tran Khac, F. Alsaffar, F.W. DelRio, K-H Chung, et al., "Surface Properties of Laser-Treated Molybdenum Disulfide Nanosheets for Optoelectronic Applications," *ACS Applied Materials & Interfaces*, vol.10, no.21, pp.18104-12, 2018.

[102] M. Albagami, A. Alrasheed, M. Alharbi, A. Alhazmi, K.L. Wong, H. Qasem, et al., "Anomalous Conductivity Switch Observed in Treated Hafnium Diselenide Transistors," *Advanced Electronic Materials*, 2020.